Defect Evolutions and Mechanisms of Structural Materials under Extreme Environments by Energy Landscape-based Atomistic Modeling

by

Zhitong Bai

A dissertation submitted in partial fulfillment
of the requirements for the degree of
Doctor of Philosophy
(Mechanical Engineering)
in the University of Michigan
2022

Doctoral Committee:

Professor Yue Fan, Chair
Professor Fei Gao
Professor Wei Lu
Professor Amit Misra

Zhitong Bai

ztbai@umich.edu

ORCID iD: 0000-0001-8461-7558

Acknowledgements

First of all, I wish to express my deepest appreciation and gratitude to my advisor, Professor Yue Fan, for his support and guidance throughout my Ph.D. study. Thanks to his kindness, patience, and persistence, I could overcome all challenges through the rough road to finish my Ph.D. program. I really appreciate his understanding and flexibility during the difficult pandemic time in my life. His training and positive working attitude will be a lifetime wealth of mine and he has been my role model for my future career.

I would also like to thank Professor Amit Misra, Professor Fei Gao, and Professor Wei Lu for serving on my dissertation committee. Their insightful comments and advices on my proposal and final dissertation defense helped me have a deeper understanding on my fundamental research studies.

I am thankful to my colleagues in Professor Fan's lab: Dr. Bin Wu, Dr. Shan Zhang, Mr. Chaoyi Liu, and Mr. Yuchu Wang for insightful discussions and suggestions on my projects of dislocation and grain boundary. I am particularly grateful to Mr. Glenn Balbus and Professor Daniel Gianola for their experimental data, helpful discussions and insightful suggestions on our collaborated grain boundary project. In addition, I am also thankful to Dr. Li Jiang and Professor Amit Misra for the trust on the collaborated high entropy alloy project.

I would also like to address thanks to the University of Michigan, especially the Rackham Graduate School and Department of Mechanical Engineering. They always give me prompt and

helpful replies whenever I have questions. Meanwhile, I also want to acknowledge National Science Foundation for providing financial support during my Ph.D. studies.

Finally, I want to address my special thanks to my friends and family members. Without your support and encouragement, I cannot overcome all of the challenges during my Ph.D. journey. No matter what happens, they are always my strongest backing. I love you all.

Table of Contents

List of Figures

List of Tables

List of Appendices

Abstract

      The energetics and kinetics of interactions between microstructural point, line, and planar defects govern the most significant mechanical properties of structural materials, which is crucial in assessing, predicting and controlling the material behavior in technological applications such as nuclear reactors and additive manufacturing (AM). Modeling microstructural evolutions under extreme conditions with high atomistic fidelity and at experimental time scales has been known as a longstanding challenge in material science. Under some cases, traditional atomistic modeling techniques like molecular dynamics (MD) enable the elucidation of molecular mechanisms of microstructural evolutions. Nevertheless, conventional MD could hardly go beyond nanoseconds and therefore simple extrapolation of MD results from short timescales could undermine the accuracy or even give a misleading prediction to materials performance at realistic environments. To overcome such challenge, advanced atomistic modeling techniques that can directly tackle the long timescale problems are greatly desired.

      In this thesis, emphasizing the limitations of MD method, we present a novel computational framework based on the concept of potential energy landscape (PEL), which enables the investigation of microstructural evolutions at long time scales while fully retaining the atomistic details. To demonstrate its capabilities, we show the application of this framework to some key problems in material science. The following problems are addressed:

      (i) We investigate a local interaction between dislocation and a vacancy-type obstacle in BCC Fe at room temperature over a wide range of strain rates, from $10^8 s^{-1}$ down to $10^3 s^{-1}$. Very

surprisingly, a non-monotonic correlation is found between the critical resolved shear stress (CRSS) of the system and applied strain rates. This suggests a negative strain rate sensitivity (nSRS) at low strain rate regime, which could be responsible for materials' degradations such as the non-uniform deformation and mechanical instabilities. We demonstrate that the nSRS is due to the complex interplays between thermal activation and applied strain rate.

(ii) We map the kinetic evolution of metastable <100> symmetric tilt grain boundaries (GBs) in copper under non-equilibrium processing, which is significant in determining the strength and ductility of nanocrystalline materials. Our combined study, providing both atomistic simulations and novel experiments employing femtosecond laser-material interactions, demonstrates striking features of the energetics and kinetic pathways to achieve a multiplicity of grain boundary states. Specifically, we populate a high-fidelity map of the energetics of the grain boundaries and show that it can be divided into an ageing regime and a rejuvenating regime over a broad energy—temperature parameter space. We further ascribe the origin of this ageing/rejuvenating behavior to the inherent energy imbalance along with elementary hopping processes in the system's underlying PEL. It is worth noting that copper material is simulated to demonstrate the reported experimental measurements on Cu-rich nanocrystalline alloys and the discovered energetic evolution may be broadly applicable to other metal materials.

(iii) We also investigate the non-equilibrium relaxations of metastable tilted GBs in copper under ultrafast thermal cycles, which is critical in assessing the structural materials' properties during AM. We demonstrate that the structural evolution of metastable GBs is mainly driven by disorder and rough energy landscape rather than free volume. Most importantly, a universal scaling is observed between the GBs' inherent structure energies and their structural transition temperatures during the rapid cooling stage. To further assess the applicability of the

obtained scaling correlation, we also investigate a group of GBs in Ni. A similar correlation

persists, which gives reason to expect the present study may apply to other materials as well.

Based on this noteworthy finding, we could manipulate GBs' microstates and properties in

advanced processing such as AM and *fs*-laser irradiation.

In summary, PEL-based modeling framework is employed to investigate the

microstructural evolution at long time scales, without invoking empirical assumptions or fitting

parameters. This framework might shed light on the predictive design of advanced structural

materials to be used in complex environments.

Chapter 1 Introduction

1.1. Motivation and Background

To meet the demand of high-performance materials for renewable and sustainable energy, it is becoming increasingly significant to study structural materials performance under extreme environments. For instance, nuclear energy is low-carbon and can be deployed to supply reliable, clean, and affordable electricity to achieve the urgent carbon neutrality mission by 2050. Thus, advanced nuclear reactors are being designed for electricity generation while operating in extreme conditions of high temperature and high doses [1, 2]. The neutron-irradiated alloys designed for nuclear reactors typically include enormous defects (self-interstitial atoms and vacancy clusters) and such microstructural evolutions are critical to understand and predict the mechanical properties of structural materials, such as swelling, creep, and irradiation-assisted crack [3-5]. Another example of renewable and sustainable energy development is additive manufacturing (AM) to improve manufacturing efficiency and reduce material waste [6, 7]. During AM process, metals and alloys' powders are melted by laser or electron beams and the powdered materials experience ultrafast heating-cooling thermal cycles, which introduces super-saturated defects such as heterogeneous distribution of grain boundaries (GBs) [8-11]. Since the high volumetric number density of GBs play a decisive role in determining the material properties [12-14], it is imperative to understand and control GB properties in structural materials under ultrafast thermal cycles produced by AM. Both sustainable energy development examples demonstrate that understanding and assessing the microstructural evolution and the

1

underlying mechanisms induced by irradiation or ultrafast thermal cycles is essential and of great importance to design structural materials more tolerant to extreme environments.

Traditional atomistic modeling methods such as molecular dynamics (MD) have been extensively employed to understand the defect evolution of high-performance materials from fundamental atomistic levels [15-18]. However, the integration time step in MD simulations cannot be larger than a fraction of a typical phonon vibration (~1-10 fs) to ensure the stable and accurate results of the integration of the equations of motion [19]. In other words, depending on the speed of computers, atom numbers, and force field potentials, MD simulations can just reach to nanoseconds, which is still far away from the time scales of experiments. Due to the huge gap in time scales between MD and experiments, under some cases, MD simulations at short time scales cannot uncover the realistic mechanisms in experiments [20, 21]. Therefore, it is imperative to develop new modeling algorithms at the fundamental level to overcome the timescale limitation and reveal the realistic mechanisms of microstructural evolution. This thesis focuses on employing the potential energy landscape (PEL)-based modeling techniques to investigate the microstructural evolutions and elucidate the underlying mechanisms and further establish quantitative structure-property relationships under extreme conditions in high-performance materials at long time scales [22-25].

1.2. Scope of Thesis

This thesis is organized as described below:

In Chapter 2, we discuss the methodology of PEL-based atomistic modeling framework at long time scales. Section 2.1 briefly describes the traditional atomistic MD method and timescale limitations in modeling microstructural evolution. Then, the notion of potential energy

surface (PES) is introduced in Section 2.2. Meanwhile, we discuss two different long time scale

atomistic techniques based on the concept of probing the transition pathways in the PES,

including the autonomous basin climbing (ABC) method and the activation-relaxation technique

(ART). In the final part of Section 2.2, we discuss the advantages and drawbacks of the two

methods of exploring the PES and availabilities for different problems of interest. We employ

ABC method to explore the PES of the system of dislocation-defect interaction in Chapter 3,

while ART is used to probe the PES of disordered grain boundaries. Finally, we discuss a

recently-developed novel computational framework based on the concept of PEL to enable the

investigation of dislocation-defect interaction at realistic strain rates by using ABC method

combined with transition state theory (TST) called ABC-T in Section 2.3. More details of

employing the ABC-T method to study microstructural evolution will be discussed in Chapter 3.

In Chapter 3, we employ ABC-T method to simulate dislocation-obstacle interaction at

realistic strain rates and uncover the different mechanisms of intermediate microstructure

evolution in BCC Fe. This is important because interactions of defects with dislocations formed

under irradiation in nuclear reactors determines the mechanical properties of structural materials.

In particular, we investigate a local interaction between dislocation and a vacancy-type obstacle

in BCC Fe at room temperature by ABC-T method, over a wide range of strain rates, from $10^8 s^{-1}$

down to $10^3 s^{-1}$. Interestingly, a non-monotonic correlation is found between the critical resolved

shear stress (CRSS) of the system and applied strain rates. As strain rate increases, the CRSS

first decreases and then increases with a minimum at the condition of $10^5 s^{-1}$. This suggests a

negative strain rate sensitivity (nSRS) at low strain rate regime, which might cause deterioration

in the nuclear reactor's structural materials. We demonstrate that the nSRS is due to the different

intermediate microstructures emerged under the complex interplays between thermal activation and applied strain rates.

In Charter 4, we focus on the kinetic evolution in a multiplicity of metastable grain boundaries (GBs) under ultrafast thermal cycles, since this microstructural evolution governs the mechanical properties in nanocrystalline during additive manufacturing process. Combined methods, including PEL-based atomistic simulations and femtosecond laser experiment collaborated with Gianola and his coworkers are employed to investigate this kinetic evolution. The energetic evolution of GBs over a broad energy-temperature space is mapped out by an advanced statistical analysis, wherein two distinct regimes—an ageing regime and a rejuvenating regime—are retrieved with high fidelity. Such ageing-rejuvenating mechanism map is universal by comparing the simulation results with various conditions (*e.g.* ultrafast heating-cooling, isothermal annealing). The ageing/rejuvenating phenomena originate from the energy imbalance during progressive transitions in the system's PEL probed by ART method, which can further be quantitatively characterized by a self-consistent kinetic equation. Without invoking free fitting parameters, our PEL-based modelling framework naturally captures key phenomena of the experimentally measured non-linear hardness variation with respect to the laser fluence under femtosecond laser pulses.

In Chapter 5, we seek to build up a robust processing-microstructure-properties correlation for metastable GBs, which could manipulate the metastable microstates of GBs without changing the macroscopic textures during additive manufacturing or nanocrystalline synthesis process. Specifically, we investigate non-equilibrium relaxations in a multiplicity of tilted GBs subjected to ultrafast thermal driving forces to mimic femtosecond laser pulses by atomistic modeling. A universal hysteresis behavior is observed in symmetrically/asymmetrically

tilted GBs. By exploring the intermediate atomic configurations and their assessable activation barriers in the underlying PEL, we demonstrate the energetics and atomic diffusions in metastable tilted GBs are disorder-driven rather than free volume-driven. A critical transition temperature is identified, separating the non-equilibrium GBs' evolution into a fast-varying stage, and a tuning-ineffective stage, respectively. Most importantly, a universal correlation between such critical transition temperature and GBs' inherent structure energy is discovered, which paves a promising way to assess and predict the kinetic and mechanical properties of interface-dominant systems.

In Chapter 6, a brief summary is given and we will discuss the importance of multiscale modeling based on the concept of PEL and potential implications on microstructural evolutions at long time scales. Finally, we discuss some future work on some complex microstructural defects and structural materials via atomistic modeling.

Chapter 2 Methodology: Atomistic Modeling

This chapter presents a variety of atomistic modeling methods employed in the following chapters of the thesis. Firstly, molecular dynamics (MD) method is briefly described and the limitation from a time scale standpoint is discussed. Then we propose potential energy landscape (PEL)-based modeling framework to capture atomic deformation behaviors and mechanisms at long time scales. Autonomous basin climbing (ABC) method and activation-relaxation technique (ART) are selected to overcome the timescale limitation and collect rare transition events by probing the potential energy surface (PES). Finally, the ABC-T method combining ABC method and transition state theory (TST) is discussed to simulate the microstructural evolution at very low strain rate conditions.

2.1. Molecular Dynamics (MD) Method

2.1.1. Overview on MD

Over the past few decades, MD simulations have been widely used in a variety of fields [26, 27] from an atomistic perspective. In principle, MD simulations could track the dynamic evolution of particles and then uncover the microscopic behavior of the system by numerically resolving the Newton's equations of motion given as:

$$f_i = m\frac{dv_i}{dt} = m\frac{d^2r_i}{dt^2} = -\frac{\partial E(r_1, r_2, ..., r_N)}{\partial r_i} \tag{2.1}$$

in which f_i, v_i, r_i, $E(r_1, r_2, ..., r_N)$ are the forces, velocities, initial positions, and potential energies, respectively. To resolve the equations of motion, the velocity Verlet algorithm [28] is

6

implemented by introducing each time step, Δt, to update positions and velocities of particles. These equations are given below,

$$r_i(t + \Delta t) = r_i(t) + v_i(t + \frac{1}{2}\Delta t)\Delta t \tag{2.2}$$

and

$$v_i(t + \frac{1}{2}\Delta t) = v_i(t - \frac{1}{2}\Delta t) + a_i(t)\Delta t \tag{2.3}$$

It should be noted that the time step, Δt, cannot be larger than a fraction of a typical phonon vibration (~1-10 fs) to ensure the stable and accurate results of the integration of the equations of motion. It is also worth noting the fitting potential force field is significant because this determines the physical attraction and repulsion between particles and further influences particles' trajectories [29, 30]. In statistical mechanics, there are three main ensembles [31, 32] (microcanonical ensemble, canonical ensemble, and grand canonical ensemble) where MD simulations are conducted. More specifically, the number of particles, volume and total energy are all kept constant in microcanonical ensemble, which is called NVE. While in canonical ensemble the temperature is constant, which is called NVT and the system is under heat bath. Finally, the grand canonical ensemble represents that the chemical potential, volume, and temperature remains constant, which allows the number of particles to change.

2.1.2. Time Scale Limitation in MD

Though MD method gives insight into the dynamic evolution of the material from an atomic viewpoint, there are still unresolved problems in terms of the length and time scales which are experimentally inaccessible. Nowadays, with huge improvement of computer power, refined potential force fields, and data storage capacity, the length scale issue is less challenging.

For example, MD simulations could be accessible to hundreds of millions of particles and running for nanoseconds [33-35]. However, the time scale problem is noticeably challenging. The reasons are twofold: according to TST, the escape time (Δt) from one of the basins is determined by the temperature and activation energy barrier as shown below,

$$\Delta t = [v * \exp(-\frac{E_A}{k_b T})]^{-1} \tag{2.4}$$

where v is the jump frequency, T is temperature and E_A is the activation barrier. 1) The low temperature slows the movement of particles and the physical phenomena of interest will require longer time, which is inaccessible in MD simulations. 2) Due to the high dimensionality of the phase space and higher activation barriers for some rare events, the system will be stuck in deep energy basins for an amount of time. Figure 2-1 shows it is hardly to transit from basin A to basin B due to the high activation barrier and MD simulation time is mostly spent near the bottom of energy basins A and B. As MD method captures the thermal vibration of particles, the time step is on the order of a typical phonon vibration (~1-10 fs). Therefore, the MD simulation can hardly go beyond nanoseconds, which are inaccessible to many realistic experiments of interest. For instance, strain rates in MD simulations are extremely high ($10^6 \text{ s}^{-1} \sim 10^{10} \text{ s}^{-1}$) [36-39], which are experimentally inaccessible (~10^{-3} s^{-1}) [40]. This huge time scale gap between MD simulations and experiments might trigger some time-dependent phenomena and underlying mechanisms at long times [20, 21]. Therefore, it is imperative to develop approaches to tackle the time scale challenge. Herein we develop and implement PEL-based modeling algorithms to investigate the microstructural evolution at long time scales, which are presented later in this chapter.
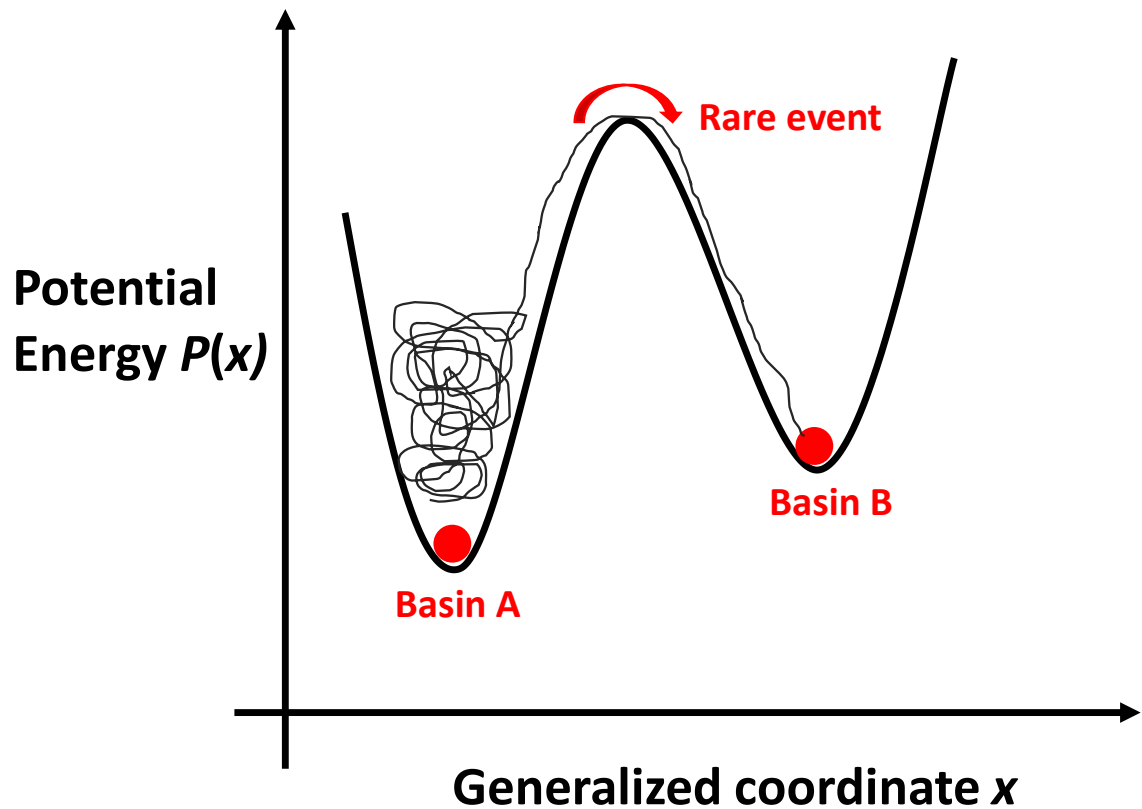
Figure 2-1. Transition from basin A to B is rare in MD simulations and most events are found near the bottom of energy basins in a MD simulation. The thin black line represents a random trajectory through the energy landscape.

2.2. Potential Energy Landscape (PEL)-based Modeling Methods at Long Time Scales

In the previous section, we mentioned the time scale limitation of MD method and thus researchers have proposed a variety of methods based on the concept of PEL to overcome this time scale limitation. In the following sections, we discuss various methods to explore the PES.

2.2.1. Potential Energy Landscape

From a fundamental perspective, the properties of a many-body system are primarily governed by the collective interactions between particles, which could be characterized by the PES. Basically, there are many local minima, also known as inherent structures (IS), representing some metastable states with certain atomic configurations. In principle, material microstructural evolutions and concomitant properties change should correspond to the progressive exploration of the IS in the PES. Thus, the microstructural evolution at long time scales could be achieved by probing the topology of the underlying PES and then further coupling that information to TST calculations. Various techniques have been proposed to explore the PES efficiently and accurately, wherein ABC and ART are widely applied for different applications. In the following two sections, we discuss the two techniques to explore the PES.

2.2.2. Activation Relaxation Technique (ART) to Explore PES

ART is a method of searching first-order saddle points as a given basin in the PES [41]. There are two main steps: the activation to a nearby saddle point and the relaxation a new minimum. During the stage of searching a nearby saddle point, the lowest eigenvalue and corresponding eigenvector of the Hessian matrix are calculated by Lanczos algorithm [42]. When the current eigenvalue or curvature of PEL's Hessian matrix is negative, with absolute value larger than a given threshold, the system is regarded as approaching to the nearby saddle state. The initial uphill push direction is changed to the corresponding eigenvector. The ART algorithm shown in Figure 2-2 for each new successful event is described as following:

i Relax the system to a local minima with an appropriate potential force filed;

ii Deform the system slightly in a random direction and create a nonzero force in a certain direction;

iii Perturb iteratively and push the system to a saddle point;

iv Judge whether it is a saddle point: (a) if it is a saddle point, go to next step; (b) if it is not a saddle point, go back to step ii;

v Push to a new local minima and relax.

```mermaid
```

Relax to a new minimum

↓

Deform randomly and create nonzero force

↓

Push to a saddle point

↓

Is it a saddle point

NO → (back to Deform randomly and create nonzero force)

YES ↓

Push and relax to a new minimum
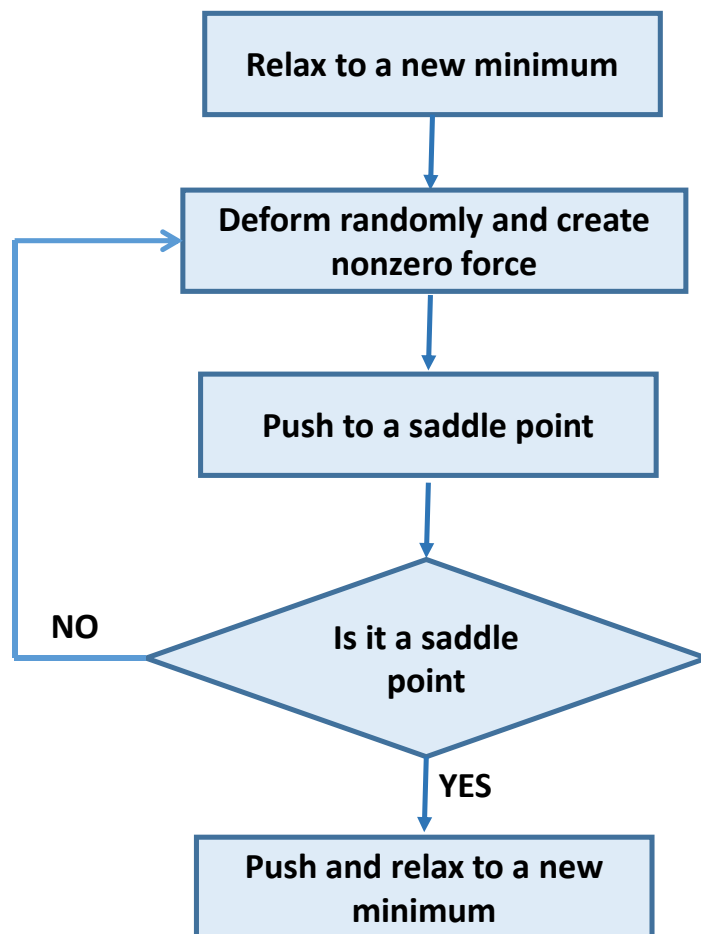
Figure 2-2. ART algorithmic flowchart at each new generated event.

Once a new event is generated, the system is brought back the original local minima again and deformed in another random direction to find new surrounding saddle points and minimum states. These collected saddle points and pathways serve as the input parameters for the further kinetic Monte Carlo (KMC) calculations. Combining ART and KMC, kinetic activation-relaxation technique (k-ART) has been proposed and successfully applied in amorphous and glassy materials, from glasses to polymers and proteins [41, 43].

2.2.3. Autonomous Basin Climbing (ABC) Method to Explore PES

The ABC method was developed by Kushima et al. [44], inspired by Laio and Parrinello's idea [45] of escaping from free energy basins by adding penalty functions in a 3N-dimensional space for a given N-particle system. Explicitly, the ABC algorithm could be implemented as the following steps:

i The system is relaxed to a local minima $E_{min}(1)$ as seen in Figure 2-3(a);

ii A penalty function is added to the system to explore the PES. The penalty function $\phi^k(r)$ follows a Gaussian shape described as

$$\phi^k(r) = w\exp[-\frac{(r-r_{min}^k)}{2\sigma^2}] \tag{2.5}$$

where k denotes the local penalty function number. The height and width are controlled by the parameters of w and σ. r_{min}^k is the minimized configuration after k-th applied penalty function. Then Figure 2-3(b) shows the modified total energy $\psi(r)$ described as

$$\psi(r) = E(r) + \sum_{k=1}^{p}\phi^k(r) \tag{2.6}$$

where $E(r)$ is the potential energy of the system and p is the total number of penalty functions;

iii The system is locally minimized to a new minima r_{min}^{k+1};

iv Steps ii and iii are repeated until a dramatic drop of the total energy occurs, which is identified as a saddle point as shown in Figure 2-3(c). The criterion of find a saddle point is the total energy is equal to the potential energy of the new local minima;

v Steps ii-iv are repeated to obtain more minima configurations in the PES.

It should be noted that ABC doesn't require the information of reaction coordinates from preceding MD calculations and therefore ABC algorithm is especially useful in exploring

unknown PES and finding low probability configurations without knowing the reaction pathways in advance.
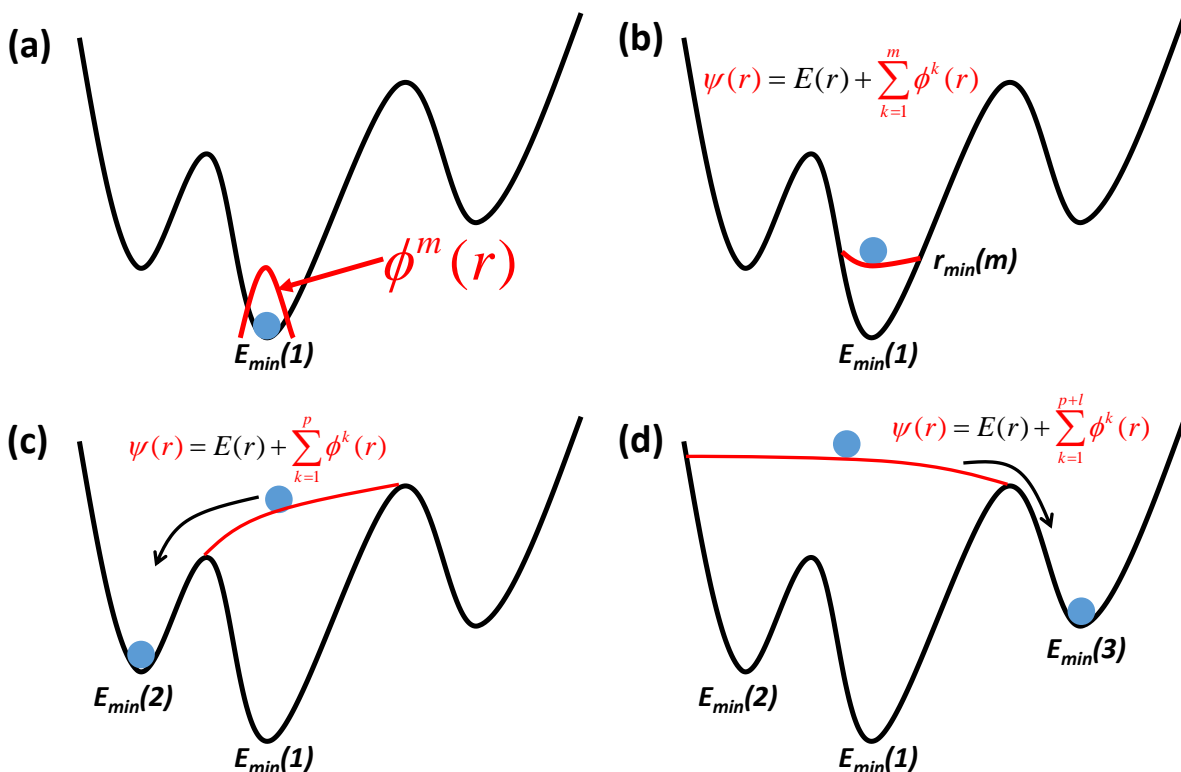
Figure 2-3. Schematic illustration of basin filling by adding penalty functions in ABC method. (a) and (b) Penalty function $\phi^m(r)$ added to push the system; (c) Find the saddle point and relax to a new minima $E_{min}(2)$; (d) Continue adding more penalty functions to find more surrounding local minima $E_{min}(3)$.

The penalty width and height controls the efficiency and accuracy of calculations in exploring the PES. For instance, smaller penalty function parameters may cause more accurate energy barriers but increase computational load. Therefore, in order to balance the accuracy and efficiency of computational load, researchers employ nudged elastic band (NEB) [46]

method to refine the energy barriers after finding initial and final states explored by ABC method.

In the ABC algorithm, the system evolves towards the pathway with the lowest energy barriers. However, ABC algorithm neglecting some neighboring higher barrier pathways will cause time overestimation if there are multiple competing transition pathways in the same basin. The extended ABC (ABC-E) has been developed by Fan and his coworkers [47] to tackle this problem. The basic principle is to add a repulsive Gaussian penalty function on the lowest saddle point to block the identified pathways. Once a new saddle point is found, the system is set back to the original local minima. By doing the iterations, multiple transition pathways could be identified in the same energy basin. The stopping iteration criteria is determined by the relative probability of the new transition with respect to previous transition pathways. Overall, ABC-E may provide more accurate estimations of the kinetic evolution.

2.2.4. Discussion on Different Techniques to Explore PES

Except the two above mentioned ART and ABC methods, dimer and temperature-accelerated dynamics (TAD) methods are also employed to explore PES. In the dimer algorithm, a replica of the system is firstly created by displacing a small and fixed distance and then the dimer system is rotated in order to find the lowest curvature of the current PEL where the dimer is located. Similarly to the ART method, the dimer method could explore multiple transition pathways but heavy computation load. The dimer method has been basically used in chemical reactions. TAD method is based on biased dynamics to activate the system by increasing the temperature. There is no need to fit the jumping frequency in TAD method, which could provide more accurate results. However, the lowest barrier limits the boost factor, and the system will be easily trapped in a well. The TAD method was applied

15

several problems, including the Frenkel pair recombination nearby GBs [48] and vapor-deposited crystal growth [49].

ART and ABC methods also own their advantages and drawbacks. The ART method could explore multiple surrounding equilibrium configurations and therefore is particularly useful in the disordered systems, including a series of transition pathways. However, this method could dramatically increase computational load for long-term non-equilibrium evolution since ART algorithm just searches one saddle point in each iteration but each local minima is connected with many new surrounding states for complex non-equilibrium systems. Recently the k-ART has been proposed based on off-lattice KMC with on-the-fly cataloging capabilities to tackle the increased computational load problem [43]. ABC method does not need the collective reaction information and thus could explore unknown PES without knowing the dominant transition pathways in advance. Meanwhile, ABC method could balance the accuracy and efficiency by tuning parameters of penalty functions. Nevertheless, there is one main issue in ABC method. ABC method needs to store the information of penalty functions to avoid finding repeated minima but this could dramatically increase computational load and memory space. A method called self-learning metabasin escape (SLME) was developed by Cao [50] to tackle this problem.

In the chapters 3-5, we employ both ABC and ART methods to probe the PES depending on the studied problem of interest. In chapter 3, we investigate the dislocation-defect interaction at realistic strain rates and ABC method is employed because dislocation gliding pathways are very clear. In chapter 4 and 5, we study the kinetic evolution and dynamic relaxation of metastable GBs, where ART algorithm is applied to explore multiple equilibrium configurations in disordered GB structures.

2.3. ABC Method Combined with Transition State Theory (TST) at Long Time Scales

ABC method could explore the static energy landscape, while it is hard to explore time-dependent landscape and corresponding behaviors. In experiments, materials normally are applied dynamic strain rate and such dynamic scenarios cause the PEL changing with time. Therefore, it is inaccurate to study the dynamic PEL by using a single initial local minima in ABC method. To address this challenge, an alternative method to apply a constant experimental strain rate to the system by consecutive ABC iterations combined with TST was developed by Fan *et al*. [51]. This method combining ABC and TST is called ABC-T (seen in Figure 2-4) and is described as following:

i Pick up a desired strain rate $\dot{\varepsilon}$;

ii Apply ABC algorithm to explore the current PES as a given strain ε_i;

iii Find the initial and final equilibrium states by ABC algorithm and apply NEB method to refine the energy barrier;

iv Calculate the hopping time Δt_i according to TST using Equation 2.4 and obtain the strain increment $\Delta\varepsilon_{i+1}$ for a certain strain rate $\dot{\varepsilon}$. The $\Delta\varepsilon_{i+1}$ could be expressed as $\Delta\varepsilon_{i+1} = \dot{\varepsilon}\Delta t_i$;

v Apply the strain increment to the system and bring back to step ii to explore the new PES.
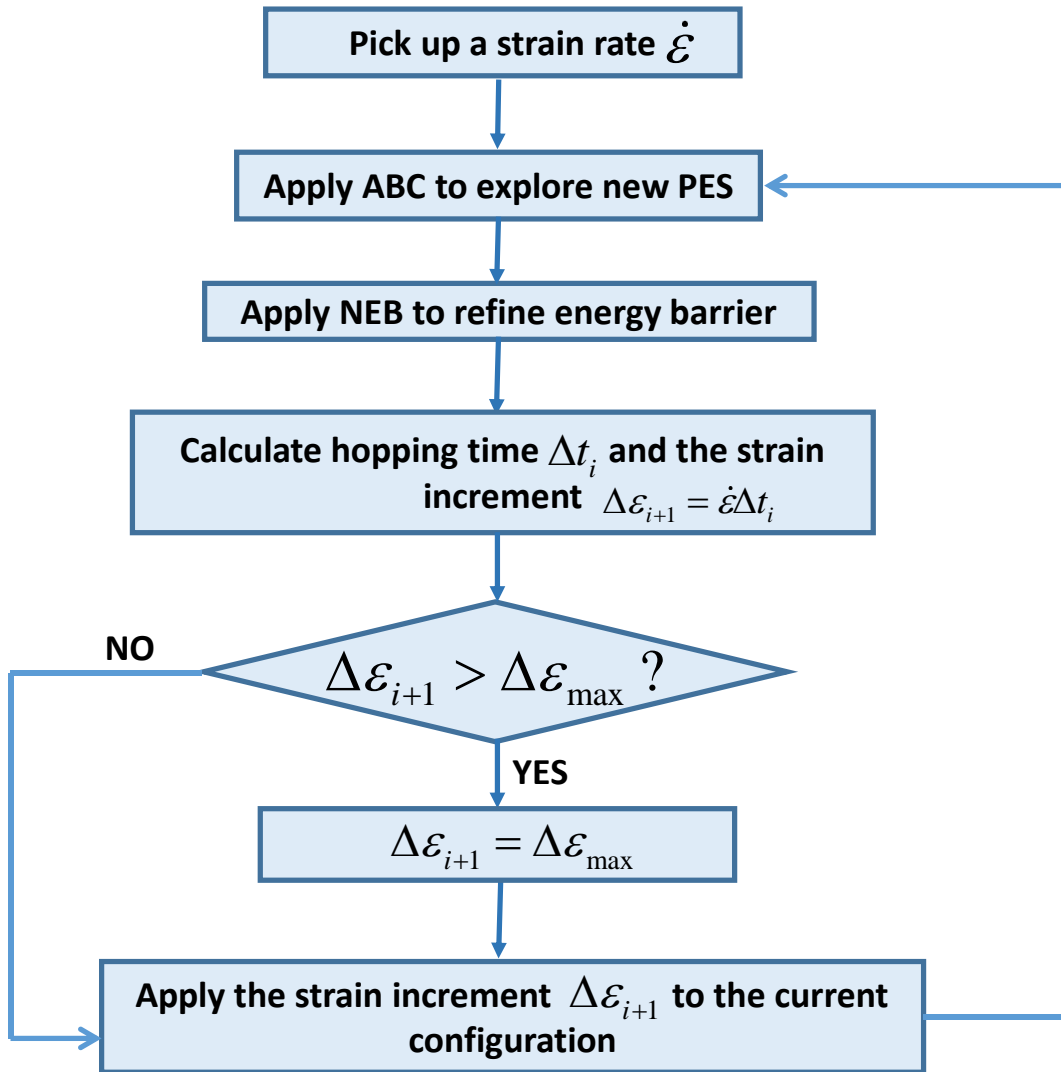
Figure 2-4. Algorithmic flowchart of ABC-T.

Thus, ABC-T could be accessible to the realistic time scale by applying an experimental strain rate. It should be noted that the strain increment $\Delta\varepsilon_{i+1}$ should be small because the strain loading is continuous in experiments and MD simulations. In other words, if the increment strain is too large, the system would be driven far away from the current state, which causes the abrupt PEL change and accumulated error. To tackle this problem, a maximum strain increment $\Delta\varepsilon_{max}$ is set up. If $\Delta\varepsilon_{i+1}$ is larger than $\Delta\varepsilon_{max}$, $\Delta\varepsilon_{max}$ is accepted instead of $\Delta\varepsilon_{i+1}$, otherwise, $\Delta\varepsilon_{i+1}$ is

applied. In the next chapter, we discuss an example of investigating dislocation-obstacle interaction at realistic strain rates by employing ABC-T method.

Chapter 3 Dislocation-Defect Interaction at Long Time Scales by ABC-T Method

The interaction between an edge dislocation and vacancy clusters in bcc Fe is investigated over a wide range of strain rates from $10^8 s^{-1}$ down to $10^3 s^{-1}$, which is enabled by employing an energy landscape-based atomistic modeling algorithm. It is observed that, at low strain rates regime less than $10^5 s^{-1}$, such interaction leads to a surprising negative strain rate sensitivity (nSRS) behavior, which was believed can only be induced by global diffusion and concentration of defects around dislocation core. We demonstrate that, even for a local dislocation-obstacle interaction, different intermediate microstructures can emerge due to the complex interplays between thermal activation and applied strain rate, and could eventually lead to the observed inverse relation between critical stress and strain rate.

3.1. Introduction

Advanced nuclear reactors are being designed for longer lifetimes while operating in extreme conditions of temperature and irradiation [1]. The microstructure of neutron-irradiated structural materials, which mainly consist of ferritic alloys, typically includes a super-saturated small defects such as self-interstitial atom and vacancy clusters [52]. The nature of interaction between such defect clusters and dislocations is critical to understand and predict the mechanical degradations of the materials, such as swelling, creep, hardening and embrittlement [3-5].

nSRS is a remarkable phenomenon showing an inverse relation between flow stresses and applied strain rates [53-55], which might lead to detrimental effects such as non-uniform deformation and mechanical instabilities [56]. It is challenging to explain nSRS by the direct

interaction between a dislocation and an obstacle. Because according to the conventional picture proposed by Kocks, Argon and Ashby [57], the activation barrier for a dislocation-obstacle unit interaction monotonically decreases as stress increases, following a (p,q)-shape power-law expression. Two direct implications stem from this picture: (i) the qualitative interaction mechanism is presumably unaffected by surrounding environments; and (ii) only a normal strain-rate sensitivity, namely a positive correlation between strain rate and flow stress, can be obtained by employing the kinetics theory. Therefore, to explain the nSRS phenomenon, a global diffusion scheme has been proposed: there is an adequate supply of defects that diffuse towards the dislocation, and lower strain rate allows more time for defects concentrate at dislocation core, which yield stronger resistance and higher flow stress [56]. Several continuum models have been developed to quantify the nSRS behavior. For example, by assuming the obstacle and dislocation concentrations are time and strain dependent, Estrin *et al.'s* model can predict an inverse behavior if the homogenous nucleation of obstacles in bulk being taken place [58, 59]. Recently, Curtin *et al.* made a significant improvement to Estrin *et al.*'s model by introducing the mechanism of direct single-atomic jump across the dislocation slip plane [60]. However, understanding the nSRS behavior fundamentally is still challenging and herein we employ ABC-T method to uncover the underlying mechanisms.

3.2. Methodology and System Set Up

For Vacancy clusters or voids are common defects in structural materials and can induce strong resistance to the glide motion of edge dislocation [61]. Therefore, we consider the interaction between the $1/2<111>$ edge dislocation and a small void containing 9 vacancies in bcc Fe. The simulation system has the dimensions 9.81 nm (x) *3.51 nm (y)*12.57 nm (z), and

contains 33171 Fe atoms. The periodic boundary conditions are applied on the dislocation line

and glide directions, respectively. The interatomic potential employed in this study is an

embedded atom method (EAM) type developed by Ackland *et al [62]*. Atomistic modeling on

dislocation-obstacle interactions at low strain rate (less than 10^6s^{-1}) has been known as a

longstanding challenge to traditional MD simulations [61]. Recently, our developed ABC-T

algorithm [51] makes it possible to probe considerably lower strain rate conditions than in

traditional MD simulations.

A schematic illustration of the modeling framework is shown in Figure 3-1. For a given

strain condition (including the initial state with no strain), employ ABC to obtain the local

dominant reaction pathway in the system's underlying PEL and get its activation barrier E_b. The

corresponding thermal activation time at temperature T can be calculated as $\Delta t = [v_0 e^{-E_b/k_B T}]^{-1}$,

according to the TST, where v_0 is the attempt frequency (of order 10^{13} s^{-1}) [63]. For a specified

strain rate $\dot{\varepsilon}$, the corresponding strain increment, $\Delta \varepsilon = \dot{\varepsilon} \Delta t = \dot{\varepsilon} [v_0 e^{-E_b/k_B T}]^{-1}$, is then applied to the

system, as shown in Figure 3-1. Keep doing the procedures iteratively until the dislocation is

unpinned from the obstacle, one can then investigate the microstructural evolutions and the

corresponding properties of the system (e.g. critical resolved shear stress (CRSS)) at prescribed

conditions of temperature and applied strain rate.

To be more specific, a few atom layers near the top and the bottom (green regions) are set

as rigid blocks in the simulation cell. The shear strain is implemented into the system by

displacing the upper block as a whole [64]. At each strain state, the total force along the

dislocation glide direction on the upper block F_b is calculated. The shear stress is then calculated

as F_b/S_t, where S_t is the top surface area of the upper block. The CRSS is regarded as the peak

stress of the stress-strain curve. More details of the model, in what we now call ABC-T, can be found in Refs. [51, 65].
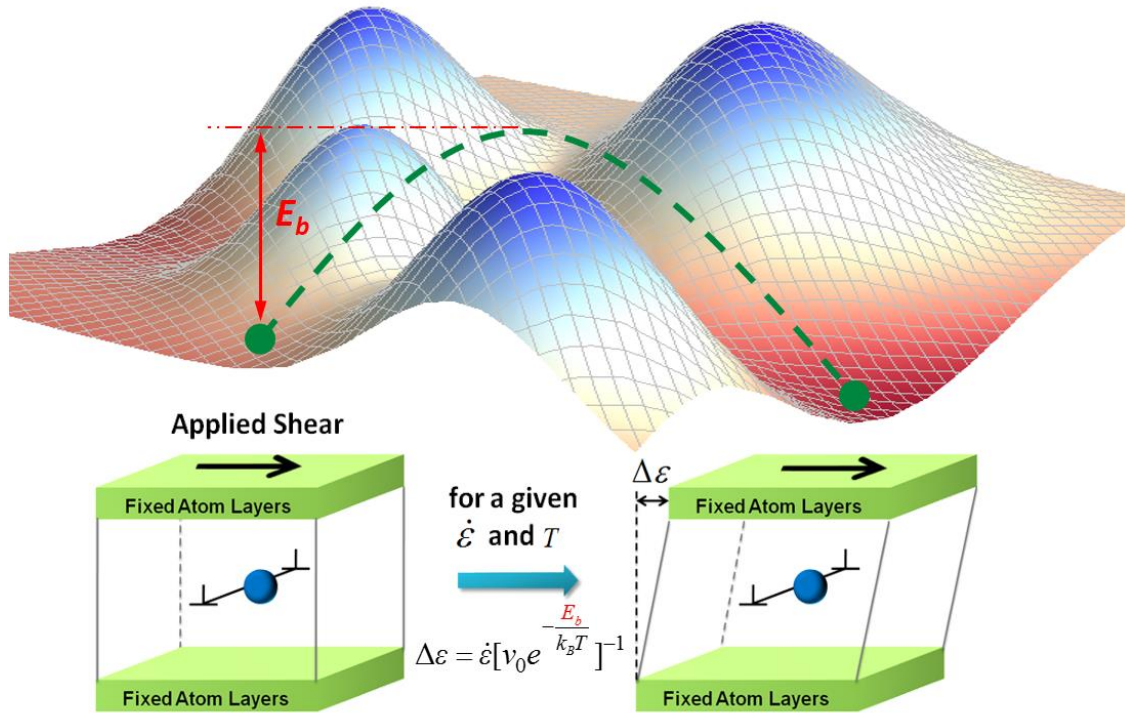
Figure 3-1. Illustration for the dynamic model in capturing the dislocation-obstacle interaction as a function of strain rate, $\dot{\varepsilon}$, and temperature, T, after combing the autonomous basin climbing method and transition state theory.

3.3. Results and Discussion

3.3.1. Dislocation-Obstacle Interaction under Static Conditions

We first studied the interaction between the dislocation and the vacancy cluster under static conditions. Figure 3-2 shows the stress-strain curve, associated potential energy (per atom on average), and corresponding critical configurations for this interaction.
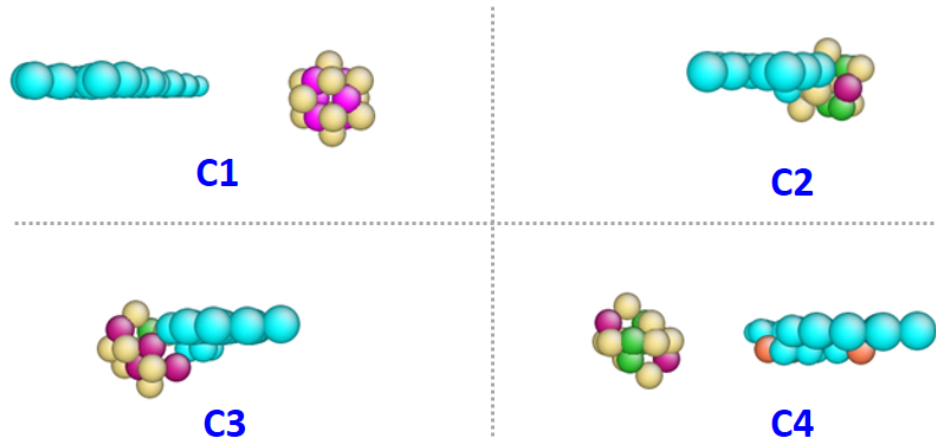
Figure 3-2. (a) The stress-strain curve, and associated potential energy (per atom on average) of the system, during the static interaction. (b) The corresponding critical atomistic configurations during the static interaction as shown in (a). The atoms are visualized by AtomEye [66], and colored according to different coordinate numbers.

In the beginning, the vacancy cluster is on the right side of the dislocation, with the center of mass placed on the glide plane. Upon shear loading, the dislocation is attached to the vacancy

24

cluster (Figure 3-2(b), C2) associated with a stress relaxation down to -251 MPa, indicating a very strong attractive pinning interaction in the early stage [61]. To better mimic the strain-controlled tensile test experimental condition, it is convenient to study the interaction as a function of strain. The corresponding strain at C2 is therefore set to be zero as a reference state. By further increasing the strain, there is a monotonic increase of the stress from C2 to C3. When the stress increases up to 570 MPa, the dislocation and vacancy cluster are detached from each other, leading to the sharp stress relaxation. The corresponding potential energy of the system during the interaction is also shown by the red curve in Figure 3-2(a). Two vacancies in the void are absorbed by the dislocation during the static interaction, and a small jog is formed after the interaction (Figure 3-2(b), C4).

3.3.2. Dislocation-Obstacle Interaction at Room Temperature over a Wide Range of Strain Rates

We then probed the same interaction at room temperature and five different strain rates from $10^8 \, \text{s}^{-1}$ down to $10^3 \, \text{s}^{-1}$, by employing the ABC-T framework shown in Figure 3-1. The results are benchmarked against independent MD simulations on the same system at the high strain rates ($10^6 \, \text{s}^{-1}$ and $10^8 \, \text{s}^{-1}$), where MD is known to be valid. Figure 3-3(a-b) show the corresponding stress-strain curves provided by ABC-T and MD simulation, respectively. It can be seen that all the CRSS under non-zero temperature are lower than the critical stress found from the static calculation. It is also noticed that in the MD simulations (seen in Figure 3-3(b)), the stress at the beginning is around -170 MPa, which is 80 MPa deviated from the static results (black curve in Figure 3-3(a)). We believe such a discrepancy is mainly attributed to the thermal compression stress produced in the non-zero temperature MD simulations, because of the fixed volume control (see **Appendix A**). The atomistic configurations after the interaction are shown

in Figure 3-3(c). Compared to 2 vacancies absorbed in static interaction, 5 vacancies are absorbed by the dislocation under 300 K, while different strain rates lead to different atomic configurations after the interaction. In the ABC-T simulations, a most compact structure of vacancy cluster is formed under 10^3s^{-1}, as seen in Figure 3-3(c). The remaining vacancy clusters for the strain rates between 10^4s^{-1} and 10^8s^{-1} are in the same structure, while the jogged dislocation at 10^8s^{-1} has a relatively ripped structure because of the extremely high strain rate. As seen in Figure 3-3(c), independent MD simulations show identical vacancy cluster configurations as in ABC-T results under the same conditions. The slight differences in dislocation structures are due to the atom oscillations in non-zero temperature MD simulations.
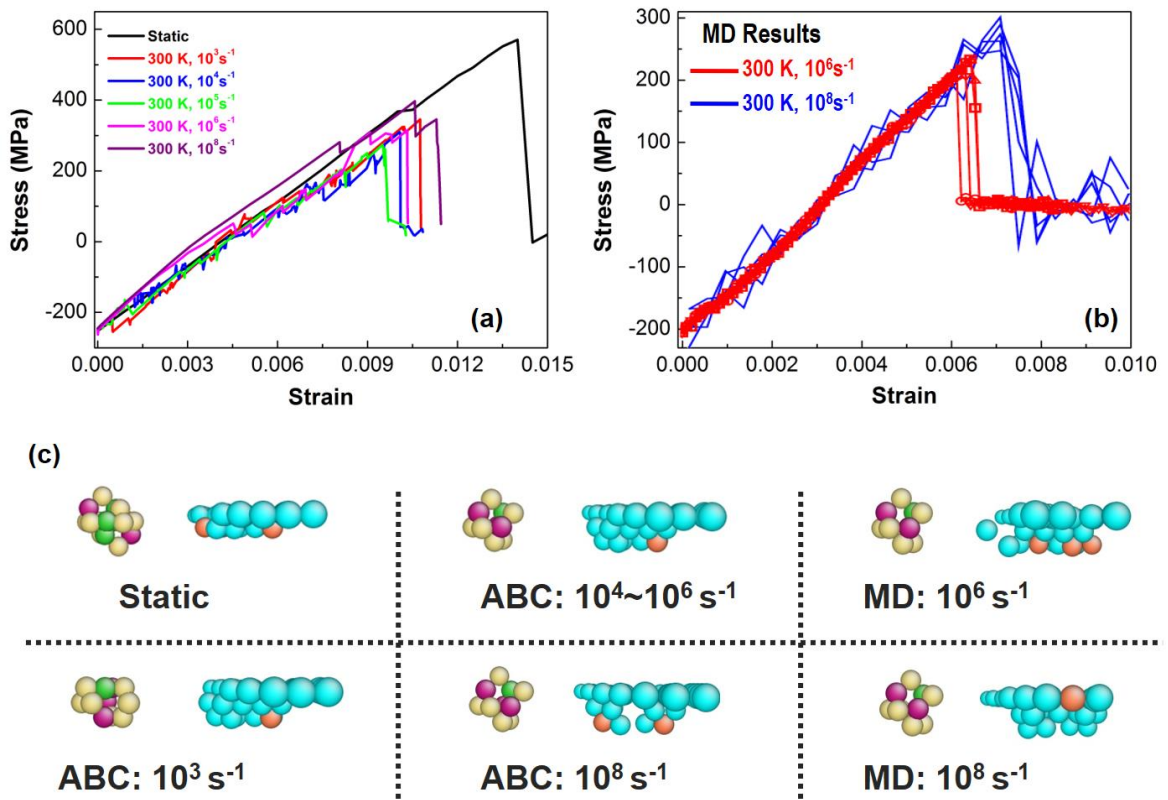
Figure 3-3. (a)-(b) The stress-strain curves for the dislocation void interaction under different strain rate conditions, provided by ABC-T and MD simulations, respectively. (c) The associated critical atomic configurations after the interaction.

3.3.3. Critical Resolved Shear Stress (CRSS) under Different Strain Rates

The CRSS under different strain rates are read off from Figure 3-3(a-b) and plotted in Figure 3-4. It can be seen from ABC-T results that, for strain rates higher than $10^5 s^{-1}$, the CRSS increases as a function of strain rate, which shows a normal relation and is consistent with earlier studies [67, 68]. It is noticed that under the same conditions, there are quantitative mismatches of CRSS between ABC-T and MD. The reasons could be twofold: (i) It might again originate from the thermal compression stress in MD simulations mentioned above; (ii) the attempt jump frequency v_0 in ABC-T is set as 10^{13} s^{-1}. Although such value has been widely used and accepted, it might become larger upon strong entropy effects [69], which could lead to a lower CRSS because each strain increment step in the ABC-T simulation will be faster and the dislocation and the obstacle would detach from each other earlier.

More importantly, if we remove the thermal stress effects and focus on the net increases of CRSS from $10^6 s^{-1}$ to $10^8 s^{-1}$, then clearly both ABC-T and MD studies show the same results. The agreements on the CRSS variations, along with the identical configurations shown in Figure 3-3(c), demonstrate the robustness of ABC-T algorithm in probing the dislocation-obstacle interactions. Very interestingly, and surprisingly, the CRSS shows a negative sensitivity to strain rate below $10^5 s^{-1}$ in ABC-T simulations.
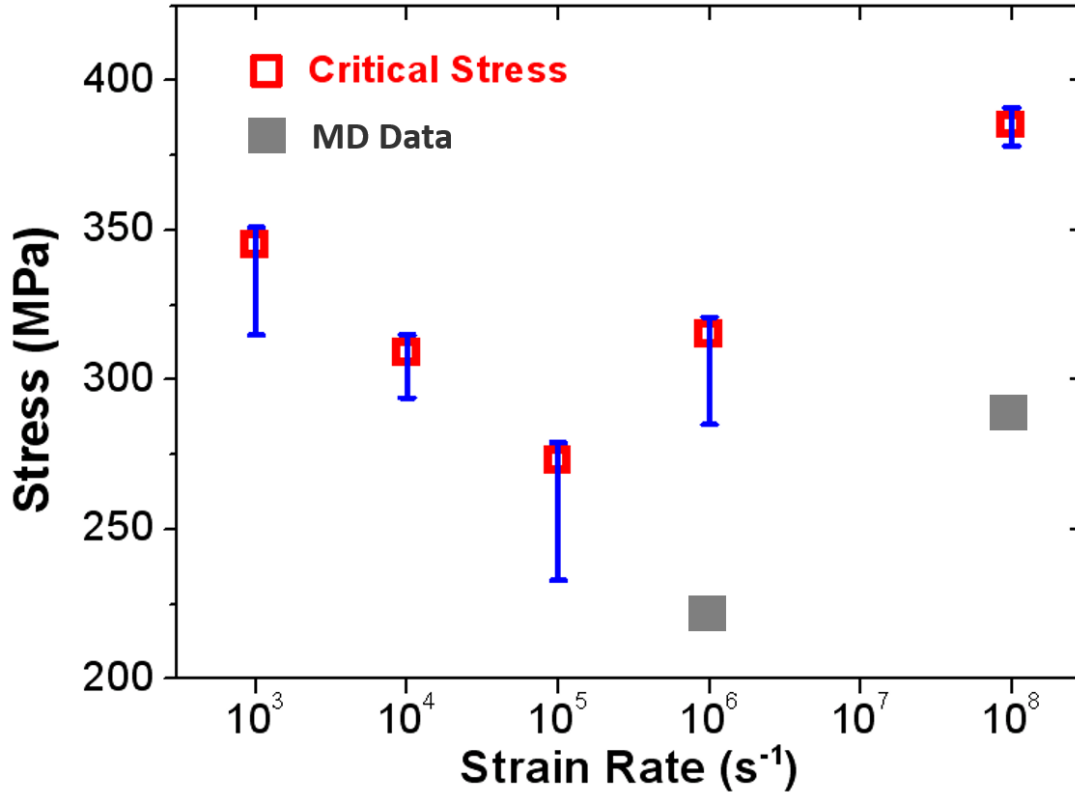
Figure 3-4. The CRSS under different strain rates conditions. Red open squares are the results of ABC-T framework simulations, while the black squares represent the MD simulations results.

3.3.4. Mechanisms on Negative Strain Rate Sensitivity (nSRS) Behavior

To reveal the underlying mechanisms of the nSRS behavior, we focus on the potential energy changes of the system during the evolutions, following the similar ideas proposed by Dutta *et al.* [70] and Monnet [71]. In particular, we analyze the system's potential energy and defect structure evolutions under different strain rate conditions. For each set of strain rate, a parabola like shape of the potential energy is observed, similar to the red curve in Figure 3-2(a). Figure 3-5(a) shows the energy differences at various strain rate conditions, with respect to the static interaction energy (red curve in Figure 3-2(a)). As seen in the figure, at relatively low strain rate $10^4 s^{-1}$, there are high frequent fluctuations on the energy difference curve, which

indicates significant amount of thermal activations and relaxations. For the higher stain rates such as 10^6s^{-1}, however, the energy difference curve is smoother, which demonstrates that the system is mainly driven by strain deformation induced by the high strain rate. It is worth noting that a similar serrate-smooth transition has also been observed in nano-indentation experiments, by increasing the applied strain rates [72].
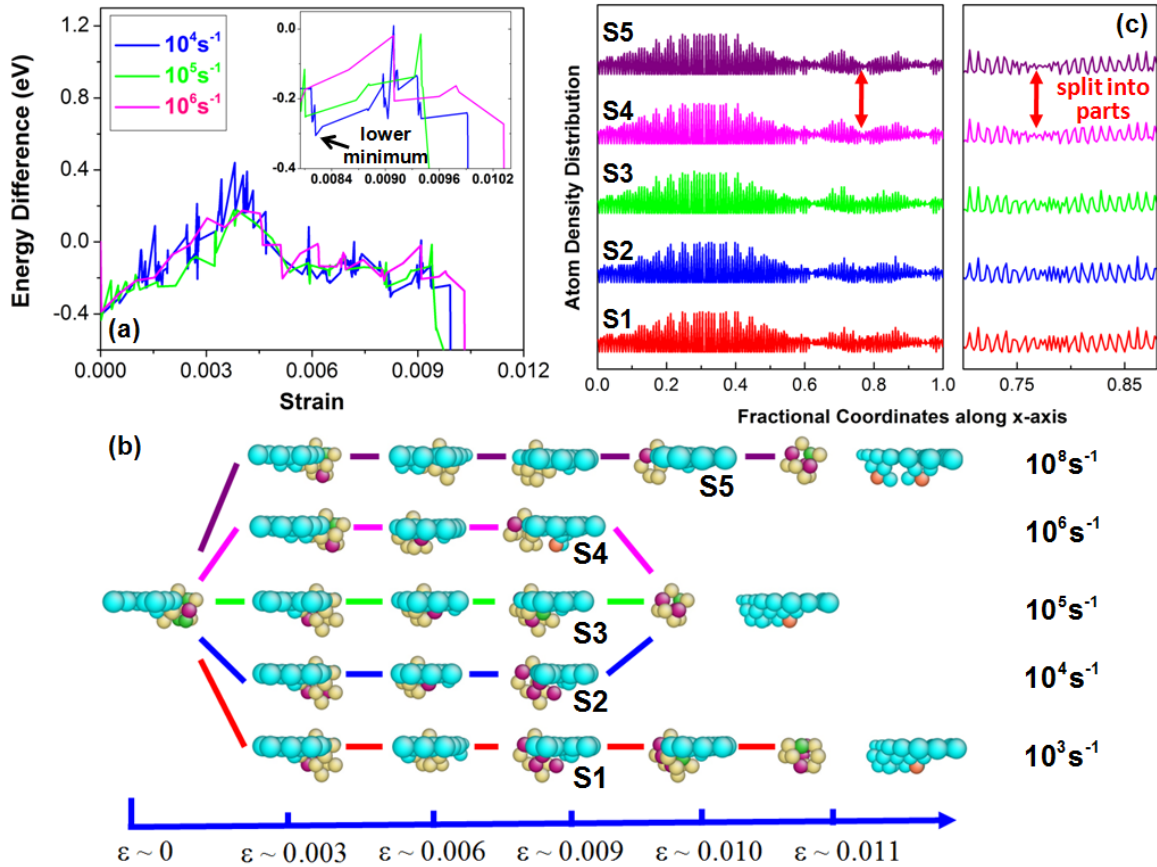
Figure 3-5. (a) The potential energy differences of the system under different strain rates conditions, with respect to the static energy curve. (b) The atomistic configurations during the interactions, at various strain rates. (c) The atom density distributions along x-axis, *i.e.* the <111> direction, for structures S1-S5. The vacancy cluster's fractional coordinate along x-axis is about 0.8. It clearly shows that for high strain rates 10^6s^{-1} and 10^8s^{-1}, the vacancy clusters are ripped into parts, while such behavior is not observed for lower strain rates.

The defect structure evolutions under different strain rates are shown in Figure 3-5(b). At early strain stage (ε~0.003), the vacancy cluster is nucleated downward due to the thermal activation, for those strain rates between $10^3 s^{-1}$ and $10^5 s^{-1}$. However, under high strain rates of $10^6 s^{-1}$ and $10^8 s^{-1}$, no such nucleation is observed because there is not enough time for this event to be thermally activated.

Assisted by thermal activations, the dislocation core glides to the right side of vacancy cluster at medium strain stage (seen in Figure 3-5(b), the configurations at ε~0.006 for the strain rate between $10^3 s^{-1}$ and $10^6 s^{-1}$). This process is associated with the energy peak between ε=0.003 and ε=0.006 shown in Figure 3-5(a). On the other hand, for the highest strain rate $10^8 s^{-1}$, the dislocation does not glide to the right side of the vacancy cluster until the strain reaches the level around 0.009. This is because, at very high strain rate condition, the thermal activations are significantly suppressed and correspondingly, the similar interaction mechanism can only take place at deferred strain [51, 73].

Upon further deformation, the structures of vacancy cluster show different evolutions at various conditions, as seen from S1-S5 in Figure 3-5(b). Under the strain rates between $10^3 s^{-1}$ and $10^5 s^{-1}$, the vacancy clusters show downward nucleation due to thermal activations (S1-S3 in Figure 3-5(b)). However, at $10^6 s^{-1}$ and $10^8 s^{-1}$, the vacancy cluster is ripped into parts (see S4 and S5 in Figure 3-5(b)) rather than being nucleated, because there is not enough time for this event to be thermally activated at very high strain rates. The atomic density projection along x-axis (gliding direction of dislocation) shown in Figure 3-5(c) also demonstrates a clear split behavior at high strain rates. It is worth noting that there are still strong connections between the ripped parts because their spatial spans are comparable with the cutoff radius of the EAM potential. Therefore, effectively the ripped structure at high strain rate imposes a larger surface area

attaching to the dislocation core. On the other hand, the vacancy clusters nucleate to different structures (S1-S3) at the strain rates between $10^3 s^{-1}$ and $10^5 s^{-1}$. S1 and S2 are in a relatively looser structure than S3, and the lower energy minimum in the inset plot of Figure 3-5(a) indicates that they are energetically more stable than S3. For both the loose structure (S1-S2) and the ripped structure (S4-S5), they have larger surface areas attached to the dislocations than S3 does. Correspondingly, the larger areas induce stronger impedances, and thus lead to higher critical stresses. This explains the reason that the CRSS reaches its minimum at $10^5 s^{-1}$.

By comparing the further evolutions between $10^3 s^{-1}$ and $10^4 s^{-1}$, it can be found that the loose structure of vacancy cluster under $10^3 s^{-1}$ (S1) further nucleates to another stable configuration, because of more available time for thermal activation under lower strain rate. Subsequently, the stable structure leads to a higher CRSS than that in $10^4 s^{-1}$. Therefore in the entire simulated strain rate regime from $10^3 s^{-1}$ to $10^8 s^{-1}$, the CRSS shows a "*V*" shape as seen in Figure 3-4.

3.3.5. Discussion on ABC-T and nSRS

It is worth noting that the minimum strain rate considered here is $10^3 \ s^{-1}$. In principle, the ABC-T method would allow us to tackle even slower processes. However, as illustrated in Figure 3-1, at a given temperature too small strain rate can only implement a negligible strain increment during each iteration, which will tremendously increase the total computational costs. As a comparison, typical experiments concerning the dislocation-obstacle interactions are usually done in the strain rate regime between 10^0 and $10^{-3} \ s^{-1}$ [21, 74, 75], which seems still slower than the present study by several orders of magnitude. But we would like to note that such low rates usually refer to the global strain rates applied to the entire specimens in the mm order.

And experiments [76, 77] show that the deformation in the specimen is highly heterogeneous and largely localized within the so-called dislocation channels, of which the width is in the order of tens of nm. In other words, inside those channels where dislocation-obstacle interactions take place, the local strain rates can be up to 105 (∼1 mm/10 nm) times larger than the average global strain rates. Since the present study focuses on the local dislocation-obstacle interaction, we therefore believe the hereby obtained results are not unrealistic.

The inverse behavior between CRSS and strain rate is known as nSRS phenomena, and can induce some detrimental effects on the materials. For example, the inverse behavior results in the decreased ductility and strength of the materials, and correspondingly generates the instabilities of materials during deformation. Understanding and explaining such behavior are therefore critical for the material design strategies. The nSRS phenomena subject to many variables, such as temperature, strain rate, defects concentration, grain size, *etc*. In our work, we particularly study the strain rate effects on the local interaction process between dislocation and obstacle. Through direct atomistic simulation we demonstrate that, in addition to previously proposed global diffusion models , the unit process of dislocation-obstacle interaction can induce the nSRS behavior as well, due to the interplay between the thermal activation and strain rate. In fact, such interplay does not only contribute to nSRS, but also results in other important phenomena, such as flow stress up-turn behavior, and dislocation channel formation.

We would like to stress that although the present study focuses on the nonmonotonic variation of CRSS in a bcc Fe system, the underlying principle—namely, the complex interplay between thermal activation and mechanical loading—is rather general and applicable to many different materials. For example, it has been found in a large variety of materials (including Al, Cu, Ni, Zr, and intermetallic $\gamma - TiAl$) [51, 65, 78] that the microstructural evolutions of

32

dislocations can be qualitatively different at different time scales. And the transitions between various mechanisms have been viewed as an underlying competition of strain rate and thermal activation, corroborating the spirit of the present study. It is also worth noting that, Schuh *et al.* [79] recently show that grain boundaries, a very different type of defect from dislocation, undergo remarkably different mobilities at the timescales beyond MD's accessibility. Their studies, together with the present observation and other recent results on dislocations, suggest that in general the defects evolutions are very complex. Therefore, the traditional simple extrapolation of MD results from short to long timescales could undermine the accuracy or even give a misleading prediction to materials performance at realistic environments. As a final note, in addition to the strain rate effects probed in the present study, many other factors (e.g. system size, type of obstacle, *etc.*) can also affect the microstructural evolutions.

3.4. Summary

In summary, we have examined an edge dislocation-vacancy cluster interaction in bcc Fe by a recently developed framework, ABC-T, which allows us to extend the atomistic modeling to low strain rate conditions. We demonstrate that the dislocation-obstacle interaction is determined by two competitive driving forces: strain rate and thermal activation. Under low strain rates, thermal activations assist the vacancy cluster in nucleating to more stable states (S1 and S2 in Figure 3-5 (b)), which induces a stronger resistance to the dislocation and therefore lead to a higher CRSS than that in $10^5 \, \text{s}^{-1}$. However under high strain rates such as $10^6 \, \text{s}^{-1}$ and $10^8 \, \text{s}^{-1}$, there is not enough time for the vacancy cluster nucleation being thermally activated. In contrast, the vacancy cluster is ripped to parts (S4 and S5 in Figure 3-5 (b)) due to the high strain rate. The parts of vacancy cluster have a larger total area attached to the dislocation than the compact

structure in $10^5 s^{-1}$ (S3 in Figure 3-5 (b)). It therefore also leads to a stronger interaction with the dislocation and thus higher CRSS. All these together explain the underlying mechanism for the "V" shape relation between CRSS and strain rate, with the minimum at $10^5 s^{-1}$. The interaction at high strain rates are directly benchmarked against MD simulations. Two independent studies show the identical atomic configurations after the interactions. The CRSS-strain rate relations are also qualitatively consistent with each other. Such consistency suggests that the basic arguments used in our analysis of competition between thermal activation and strain rate effects are correct, at least in the limit of high strain rates.

Chapter 4 Kinetic Evolution of Metastable Grain Boundaries under Non-Equilibrium Processing from the PEL Standpoint

In the previous chapter we proposed ABC-T algorithm to achieve realistic time scales while retaining fully the atomistic details. This method was validated by low strain rate shear tests for dislocation-obstacle interaction, which is significant in studying nuclear materials' degradations such as the non-uniform deformation and mechanical instabilities. In this chapter, we address another longstanding challenge of understanding the kinetic evolution of metastable GBs under non-equilibrium processing, which is crucial in assessing and controlling structural material properties during additive manufacturing (AM).

4.1. Introduction

Polycrystalline solids are among the most pervasive engineering materials, and the interfaces between the grains, known as GBs, play a decisive role in determining the system's physical properties [80, 81]. In recent years, nanocrystalline (NC) alloys have received considerable attention, because the high concentration of GBs endows the systems with high strength [12, 82-84], improved resistance to wear [85] and fatigue [86], and in some instances high ductility [87]. Meanwhile, additive manufacturing (AM) is regarded as a disruptive technology owing to its unique capabilities of creating an object by stacking layers of materials into complex 3-D geometries. During AM process, metals and alloys' powders are melted by laser or electron beams and the powdered materials experience ultrafast heating-solidification non-equilibrium thermal cycles, which results in enormous defects such as grain boundaries in

relatively large columnar grains [8]. Thus, investigating the kinetic evolution of GBs under ultrafast thermal cycles is essential in assessing and controlling structural materials performance in AM.

Traditionally, the structure and properties of a given GB are characterized by five angular degrees of freedom between the neighboring crystals. While this macroscopic description of GBs is powerful, it does not uniquely and completely describe the atomistic structure of the GB. To be more specific, GBs' microscopic configurations are typically isolated by identifying the structures with minimum energy at $0K$. These structures are usually associated with high coherency and distinguishing structural units, *e.g.* kites [81, 88, 89] or misfit dislocation arrays [90, 91]. However, such "ideal" equilibrium GBs with "frozen" microstructures are too often over-simplified and do not capture the complex behavior of GBs under realistic environments [80].

Recent computational studies by Han and Srolovitz [14] have systematically demonstrated that GBs, even with a fixed misorientation, can exhibit an essentially infinite number of metastable states with a broad and continuous spectrum of energies. It has also been demonstrated that the NC alloys' enhanced fatigue toughness [86] and record-breaking combination of strength and ductility [87] may in fact originate from intentionally introducing disorder within the GB regions. Moreover, recent sub-ablation femtosecond (*fs*) laser experiments [92] show that NC samples could experience a significant hardness variation (up to 87%) following laser pulses with negligible grain sizes changes. These studies collectively underscore the pressing need for a fundamental and self-consistent knowledge on the evolution of non-equilibrium metastable GBs' under external stimuli.

4.2. Methodology and System Set Up

A realistic embedded atom method (EAM) inter-atomic potential [93] for Cu is employed in atomistic simulation for the construction and investigation of GBs in this study. At first, the "ground-state" configurations for a group of <100> STGBs are created through a conventional bicrystal set-up: the symmetrically tilted upper and lower grains are joined together, followed by in-plane rigid body translations, atom deletions, and finally a conjugate gradient minimization [94]. The sizes of simulation boxes vary from 23,840 to 135,200, depending on the specific misorientation angles (more details in **Appendix B**, **Table B-1**).

Random perturbations are then introduced to the hereby constructed ideal GBs to mimic the consequences of fast external stimuli. Specifically, a thin plate section near the GBs (between -7 Å and 7 Å along the normal direction) is selected, and atoms therein are randomly chosen and displaced to a random position. By minimizing the system after each random perturbation, a multiplicity of metastable structures and their corresponding energies can thus be obtained. Note that the atom numbers are kept constant during the metastable GBs creation process, because in the scope of present study the system is driven out of equilibrium under ultrafast stimuli (*e.g.* sub-ablation *fs*-laser pulses) and thus should no longer be characterized by a grand canonical ensemble.

The energetic and structural evolutions of metastable GBs under both isothermal annealing and fast thermal-cycling conditions are investigated by MD simulations using the LAMMPS software. For isothermal annealing studies, the system is annealed at a constant temperature with the NPT (P = 0) control for 500 *ps*. The time step is set to be 2 *fs*. The energy and structure of the system are calculated every 1 *ps*. For fast thermal-cycling studies, the metastable GBs' energy and configurations are tracked every 5 *K*. The energy of a metastable

GB is calculated as the excess energy of the present configuration divided by the area of grain boundary plane, where the excess energy is defined as the energy difference between the GB system's potential energy and the potential energy of a single crystal system with the same number of atoms.

The ART [95] is also employed in sampling the PEL of metastable GBs and obtaining their activation energy spectra. Specifically, the ART simulation is initiated by choosing a random atom inside the GBs, which has been characterized as the particles with a centro-symmetry parameter (implemented in LAMMPS) larger than 2.0. Then small perturbations, *i.e.* random displacements, were applied to the central atom and its nearest neighbors with a total displacement of 0.5 Å. When the lowest eigenvalue (*i.e.* curvature) of the PEL calculated by Lanczos algorithm is found to be smaller than -0.01 eV Å^{-2}, the system is then relaxed toward the saddle point with a force tolerance of 0.005 eV Å^{-1}. For each central atom, 10 ART searches with different perturbation directions are applied. Finally, statistical histograms are obtained by removing the repeated and failed searches.

4.3. Results and Discussion

4.3.1. GBs' metastability Evolution in Energy-Temperature Space

Infinite number of metastable GBs with various energy states can be created through the random perturbations described above in last section, and the left panel in Figure 4-1 shows 4 representative structures after perturbing the ideal Σ5 (310) STGB. The hereby obtained metastable structures are then subjected to isothermal annealing at various temperatures below the system's melting point (T_m~1350K), and the corresponding energetic temporal evolution curves are tracked, as seen in the right panel of Figure 4-1. To better analyze the GBs' evolution,

38

we herein adopt the quenching protocol used by Zhang and Srolovitz [96] and focus on the variation of the GBs' inherent structures (ISs) energy. Note that the ISs are obtained by minimizing the dumped configurations to $0K$ with a steepest descent algorithm, and the real dynamics at finite temperatures are not interrupted.
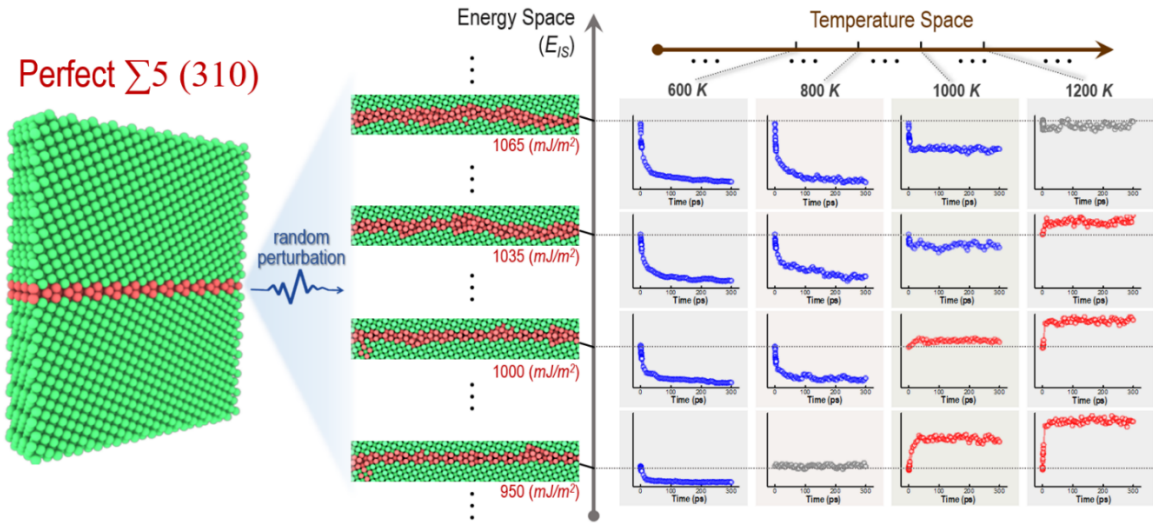
Figure 4-1. (Left) A multiplicity of metastable Σ5 (310) GBs across a broad energy range are created by introducing random perturbations to the ideal ground-state GB. (Right) The produced metastable structures are then subjected to isothermal annealing at various temperatures from $0K$ to $1300K$ (below the system's melting point, $T_m\sim1350K$), and the corresponding energetic temporal evolution curves are tracked.

It is evident in Figure 4-1 that the evolution of a metastable GB is sensitively dependent on both its IS energy (denoted as E_{IS}) and surrounding temperature. In some parameter space (blue curves), E_{IS} decreases to a lower level during annealing, which essentially represents an ageing phenomenon; while in some other parameter space (red curves), E_{IS} increases as a function of time, which corresponds to a rejuvenating behavior. Under some specific cases (grey curves), GBs reach a steady state condition with the E_{IS} being invariant with annealing time. To avoid the plot being too crowded in Figure 4-1, we only display the evolution of 4 representative

metastable GBs at 4 different temperatures. Many more metastable states have actually been considered in the present study over many more assigned temperature conditions, and we note that they all share the qualitatively similar complexity.

4.3.2. Mapping of Ageing and Rejuvenating

Figure 4-1 suggests that metastable GBs' energetic evolution is intrinsically non-linear and non-monotonic. To better understand such behavior subjected to complex conditions, it is critical to quantify their intrinsic ageing/rejuvenating rate. The energy variation rate can be calculated by analyzing the time derivative of the isothermal annealing curves $\left(\partial E_{IS}/\partial t\right)\big|_T$, at various prescribed (E_{IS}, T) conditions. Using an enhanced statistical analysis to examine the evolution of all the generated metastable GBs (see **Appendix B**, Figure B-1 for details), a high-fidelity pixel-wise map on the energy variation rate is constructed in Figure 4-2.**a** across a broad parameter space.

For the convenience of visualization, each pixel comprising the map is colored on a log scale according to its energy variation rate. At first, it is immediately apparent from Figure 4-2.**a** that the evolution of metastable GBs can be divided into two distinct regimes, namely an ageing regime (blue) where $\left(\partial E_{IS}/\partial t\right)\big|_T$ is negative and a red regime where $\left(\partial E_{IS}/\partial t\right)\big|_T$ becomes positive. The crossover boundary is marked by the dashed yellow curve, indicating the steady state condition. Another intriguing observation is that, the contour lines in the blue regime exhibit a non-monotonic dependence on temperature, indicating an optimized condition for the ageing of metastable GBs to take place.
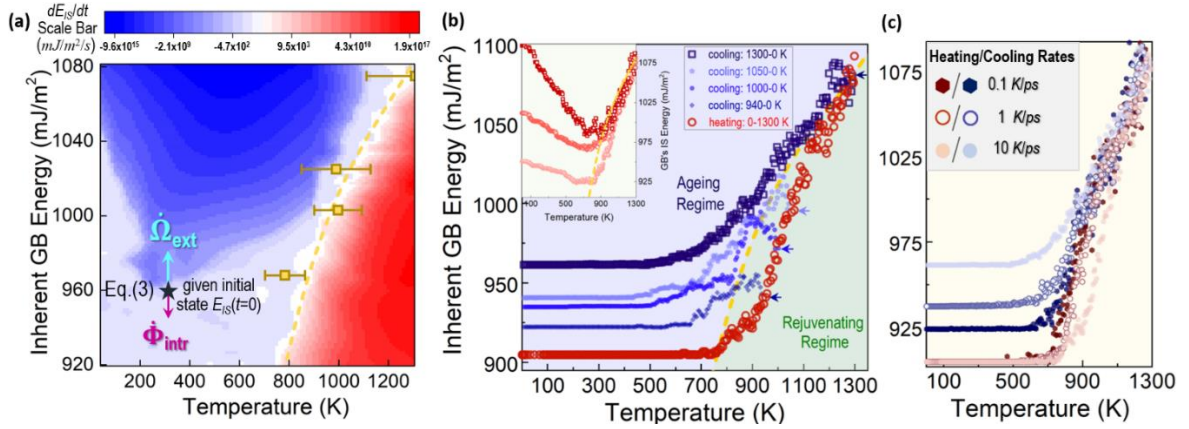
Figure 4-2. (a) Resolved pixel map of GB's energetic variation rate in the broad energy-temperature space. In the red regime $(\partial E_{IS}/\partial t)|_T > 0$, and the system exhibits a rejuvenating behavior; while in the blue regime $(\partial E_{IS}/\partial t)|_T < 0$, and the system exhibits an ageing behavior. The ageing/rejuvenating crossover boundary is marked by the dashed yellow curve. The open yellow squares with error bars are the numerically calculated solutions to $\bar{E}_A(T) - \bar{E}_R = 0$, provided with the E_A and E_R spectra at different energy levels in the system's underlying PEL. (b) MD validations on GB's metastability evolution under fast heating-cooling cycles at the rate of 10 *K/ps*. The anomalous peaks in the truncated thermal cycles (*i.e.* heating/cooling switching at intermediate temperatures of 940 K, 1000 K, and 1050 K marked in the plot) overlap well with the dashed yellow curve extracted from (a), suggesting the validity of the obtained ageing/rejuvenating mechanism map. Inset plot shows the energetic evolution of a few metastable states with higher initial energy levels during heating at 10 *K/ps*. The system's IS energy keeps decreasing in the early stage until it hits the dashed yellow curve, and then the system's IS energy starts to increase afterwards. (c) The heating/cooling cycles at different rates in MD simulations. The hysteretic behavior remains, while its magnitude becomes smaller at lower rates.

It is worth noting that, Figure 4-2.**a** is constructed upon the isothermal annealing analyses independently from any special/extreme driving forces. In other words, such a map reflects generally the metastable GBs' energetic evolution at various prescribed (E_{IS}, T) conditions. Therefore, to validate the demarcation of ageing and rejuvenating regimes given by Figure 4-2.**a**,

41

the two most straightforward approaches one can consider is to introduce external stimuli either

along the E_{IS}-axis or along the T-axis. The E_{IS}-axis examination will be discussed later, and here

in this section we introduce the T-axis stimuli to verify Figure 4-2.**a** through a series of

heating/cooling MD simulations.

Specifically, in Figure 4-2.**b** the initial ground-state Σ5 (310) GB is heated to 1300K (red

open circles) at a rate of 10K/ps, which is then immediately followed by a cooling treatment to

0K (dark blue open squares) at the same rate. Overall, there exhibits a clear hysteretic behavior,

which is not surprising because the GB is driven away from equilibrium by the ultrafast

processing and eventually trapped at a metastable state. More specifically, in the heating stage

the system's IS energy does not substantially increase until it goes beyond the crossover

boundary (dashed yellow curve) and enters the rejuvenating regime previously identified in

Figure 4-2.**a**. Between 1100K and 1300K the data points overlap with the dashed yellow curve,

because at high temperatures the intrinsic relaxation dynamics becomes fast enough and the

system is able to remain at steady state. Upon cooling from high temperatures, the dark blue

squares are located consistently on the left side of the crossover boundary and exhibit a

monotonic decreasing (*i.e.* ageing) behavior, corroborating the mechanism map in Figure 4-2.**a**.

The heating/cooling rate effects are examined in Figure 4-2.**c** at lower rates of 1K/ps, and

0.1K/ps, respectively. The hysteretic behavior clearly remains, although the apparent magnitude

of hysteresis becomes smaller at a lower heating/cooling rate because it would provide more time

for the system to relax towards the equilibrium. Admittedly, the heating/cooling rates in MD

simulations are extremely fast. But it is not impossible to benchmark the MD results by realistic

experiments. For example, electrical pulse technique can reach an effective cooling rate of 10^{14}

K/s [97] that is even shorter than typical MD timescales, although such a comparison is beyond

the scope of the present study. We also note that, while the magnitude varies, such hysteresis is universal in a diversity of other <100> STGBs (see **Appendix B**, **Figure. B2).**

To further verify the ageing/rejuvenating mechanism map, we truncate the full thermal cycle and instead begin the cooling treatment at intermediate temperature, *e.g.* 940*K*, 1000*K*, and 1050*K* marked in Figure 4-2.**b**. An anomalous behavior occurs under such scenarios. Specifically, the energy first increases despite the decreasing temperature, reaching a peak value below the temperature where the simulation is truncated. It therefore suggests that, on the right side of those anomalous peaks there is $\left(\partial E_{IS}/\partial t\right)\big|_{T} > 0$, while on the left side there is $\left(\partial E_{IS}/\partial t\right)\big|_{T} < 0$. It is evident that those peak positions are well located on the crossover boundary extracted from Figure 4-2.**a**. The inset plot in Figure 4-2.**b** presents another set of MD validation by heating (at 10*K/ps*) a few selected metastable GBs with higher initial energy states. It is clear that the energy decreases first and then increases, and transitioning points of such non-monotonic variations align well again with the extracted yellow curve from Figure 4-2.**a**. The extent of such agreement suggests that the hereby discovered ageing/rejuvenating mechanism map is rather universal, irrespective of the actual stimuli used to elicit those non-equilibrium GB structures. As discussed below, this would also lay the foundation to describe and explain the mechanical behavior of NC alloys under *fs*-laser irradiation.

4.3.3. PEL Origin of the Non-Equilibrium Evolution

In pursuit of explaining the underlying physics of the obtained mechanism map, here we adopt a PEL perspective because the time evolution of a condensed matter system and any concomitant property changes are known to correspond to the transitions between local minima and progressive exploration of different ISs in the system's underlying PEL [98-105]. Note that a

similar ageing/rejuvenating behavior has been recently reported in metallic glasses [106], and it is demonstrated there that the crossover boundary can be well characterized by the competitions between an effective uphill climbing energy ($\bar{E}_A$) and a downhill dropping energy ($\bar{E}_R$) during sequential transitions in the system's potential energy landscape. In particular, when $\bar{E}_A < \bar{E}_R$ the system would evolve towards a lower energy state and thus undergo an ageing process; otherwise, an opposite rejuvenating effect would occur. Given the many reported similarities between glasses and GBs [107-111], here we seek to employ such an energy imbalance criterion to interpret the resolved map in Figure 4-2.**a**. Specifically, the effective $\bar{E}_A$ and $\bar{E}_R$ are calculated as:

$$\bar{E}_A(T)|_{IS} = -k_B T \cdot ln[\int P(E_A)|_{IS} \cdot e^{-\frac{E_A}{k_B T}} dE_A] \tag{4.1}$$

$$\bar{E}_R|_{IS} = \int E_R \cdot P(E_R)|_{IS} dE_R \tag{4.2}$$

Note that because in GB systems each IS can be connected with many different saddle states, all those potential pathways in the PEL [112] need to be taken into consideration. Therefore, instead of being explicit numbers, the effective $\bar{E}_A$ and $\bar{E}_R$ have to be estimated over the broad distributions, $P(E_A)|_{IS}$, and $P(E_R)|_{IS}$, respectively, which are dependent on the system's present IS. The key difference above is that $\bar{E}_A$ is T-dependent, while $\bar{E}_R$ is T-insensitive. This is because the up-hill climbing is a thermally activated process, while the down-hill dropping can spontaneously happen and does not need thermal assistance.

One can analytically prove that $\bar{E}_A(T)|_{IS}$ in Eq. (4.1) is monotonically increasing as a function of T. Therefore, it is expected that the term $(\bar{E}_A - \bar{E}_R)$ would flip from negative to positive as T increases, naturally explaining the transition from ageing to rejuvenation in Figure

44

4-2.**a**. More quantitatively, the ageing/rejuvenating crossover should occur when $\bar{E}_A(T) - \bar{E}_R = 0$.

Therefore, according to Eqns. (4.1-2), a precise quantification of the crossover point relies on the determination of accurate spectra of $P(E_A)\big|_{IS}$ and $P(E_R)\big|_{IS}$. Here we employ the ART method to obtain such spectra, which is known as an effective atomistic sampling algorithm capable of probing the PEL structures with high fidelity [95, 113-115].

Figure 4-3.**a** shows the obtained spectra of E_A and E_R at 4 different IS energy levels: $1075\,mJ/m^2$, $1025\,mJ/m^2$, $1003\,mJ/m^2$, and $968\,mJ/m^2$. The distribution $P(E_A)\big|_{IS}$ shows an apparent dependence on the GBs' IS energy level: as E_{IS} decreases, the fractional distribution of low energy activation values becomes smaller, resulting in a larger average E_A. On the other hand, $P(E_R)\big|_{IS}$ is evidently IS-independent and follows a universal exponential decaying distribution, reminiscent of similar features in glassy materials. The computed spectra of $P(E_A)\big|_{IS}$ and $P(E_R)\big|_{IS}$ are then fed into Eqns. (4.1-2) for numerical calculations, and by varying the temperature one can thus identify when the crossover condition (*i.e.* $\bar{E}_A(T) - \bar{E}_R = 0$) is satisfied. The open yellow squares in Figure 4-2.**a** represent such PEL-enabled calculations, which are consistent with the independent annealing studies within numerical error. Such agreement is encouraging, as it lends credence to the notion that the nature of the GBs' ageing/rejuvenation originates from the kinetic processes in the underlying PEL.
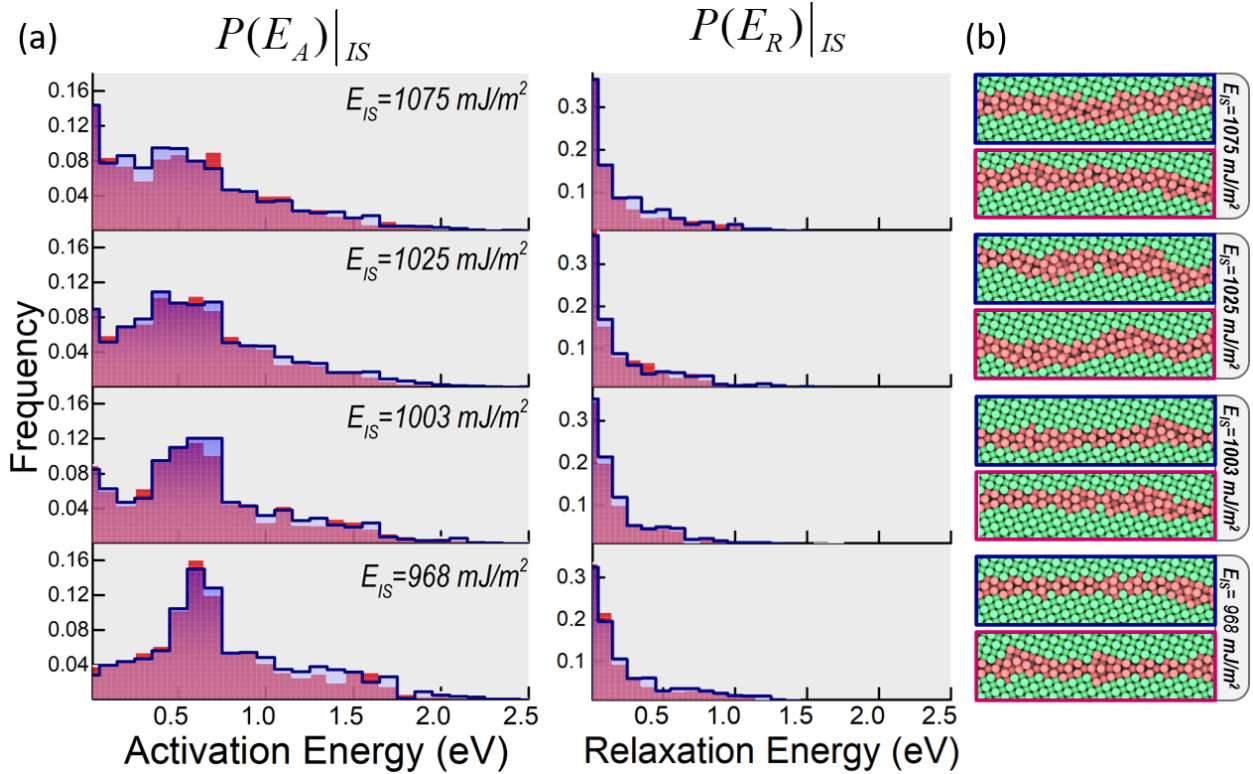
Figure 4-3. (a) The ART-probed E_A and E_R spectra of metastable GBs at different energy levels by sampling the system's underlying PEL. In each panel it displays the spectra of two metastable GBs at the same energy level but with different atomic configurations shown in (b).

It is also worth noting that the broad E_A spectra approximately consist of two modes: a distribution centered around $0.6 eV$, and another complementary mode distributed within the lower energy tail. These seem to correspond to the reported activation barriers for GBs' self-diffusion [116, 117], and the collective reshuffling processes [116], respectively. In other words, the entire spectrum of the GBs' migration/diffusion mechanisms are implicitly encoded in the PEL. Another noteworthy feature is that the activation energy spectra seem to be sensitive only to the energetics of GBs' IS rather than its detailed atomic configuration. To be more specific, in each panel of Figure 4-3.**a** we show the spectra of two metastable GBs at the same energy level but with different atomic structures (Figure 4-3.**b**), and the spectra are

evidently similar to each other. As discussed later, this might lead to a vast simplification in building an explicit expression of $P(E_A)$ for metastable GBs.

The non-monotonic ageing phenomenon discussed above in Figure 4-2.**a** can also be readily explained by such a PEL picture. Specifically, the system's overall metastability evolution should be mutually determined by a driving factor, and a kinetic factor, respectively. The driving force factor, namely $(\bar{E}_A - \bar{E}_R)$, determines the direction/sign of the evolution. As discussed above, in the blue regime the sign of $(\bar{E}_A - \bar{E}_R)$ is negative while its absolute value keeps decreasing as T increases. On the other hand, the kinetic factor in general exhibits a monotonic increasing dependence on T. Such opposite sensitivities to temperature yield the observed non-monotonic contour lines in ageing regime. These collective results point to a wholly consistent viewpoint of metastable GBs' energetics and their evolutions.

4.3.4. Implication on the Mechanical Behavior of GBs

The mechanical behavior of nanocrystalline materials is inherently linked to the energetic state of GBs in the limit where deformation mechanisms become increasingly GB-mediated. Work from Vo [118] *et al.* demonstrated that, for a fixed grain size, the yield strength of nanocrystalline Cu is inversely proportional to the GB energy. Other simulations have demonstrated that during the deformation of metastable GBs, mechanisms such as GBs sliding are preferred over traditional dislocation plasticity, which in turn dramatically affects the mechanical properties [119]. Even in cases where dislocations participate in plastic deformation via GB emission and absorption mechanisms, their nucleation and propagation barriers as well as their ability to annihilate at GBs are influenced by the interface energies. Indeed, experimental evidence supports the observation that the hardness of a GB-concentrated system varies inversely

as a function of its energy level [92]. Therefore, the PEL framework discussed above allows for a prediction of the GBs' mechanical performance at different conditions. We focus on recent experiments showing GB rejuvenation using ultrafast (*fs*) laser pulses, which result in dramatic changes in the material hardness [92].

The interactions between *fs*-lasers and materials are rather complex, but several insights relevant to the present work can be gleaned. On the one hand, extremely fast temperature variations can be involved. Although the heating and cooling rates during sub-ablation threshold *fs*-laser experiments (focused in the present study) have not been investigated, simulations of high-energy *fs*-laser irradiation that induce material ablation demonstrate heating and cooling rates upwards of 10^{11} *K/s* during the ablation process [120, 121]. While the relaxation phenomena present in sub-ablation *fs*-laser irradiation is similar to that during ablation, as no material is removed during experiments we do not anticipate such high temperatures or heating rates, although modeling efforts to investigate such phenomena would make for intriguing future work. Despite limited understanding of the temperature effects in this regime, sub-ablation *fs*-laser irradiation results in *GPa*-level tensile and compressive stress waves localized to GBs that may induce localized atomic rearrangements [92, 122], effectively increasing the energy of GBs regardless of the thermal profile. Thus, while it is intractable to experimentally measure the effective heating/cooling rates during sub-ablation *fs*-laser irradiation, the net result of such irradiation should be an overall increase in the energetic state of the GBs at a fixed temperature, as evidenced by the dramatic decrease in hardness. Considering these points, the system's energetic evolution in the presence of external stimuli, as illustrated in Figure 4-2.**a**, should then be determined by the interplay between two factors,

namely the intrinsic energy variation $\dot{\Phi}_{intr}(E_{IS}, T) \propto (\bar{E}_A - \bar{E}_R)$, and the external energy input

rate $\dot{\Omega}_{ext}$ (*i.e.* net results of sub-ablation *fs*-laser irradiation discussed above), respectively.

While an analytical expression of $\dot{\Phi}_{intr}(E_{IS}, T)$ is not yet available, its numerical value

over broad E_{IS}—T space can be obtained by interpolating the high-resolution pixel map in

Figure 4-2.**a**. Therefore, using experimentally-relevant values of $\dot{\Omega}_{ext}$ (*e.g.* the power of the *fs*-

laser pulse) and the GB's initial energy state $E_{IS}(t=0)$, one can then numerically resolve the

GBs' metastability evolution. The qualitative picture is clearly captured in Figure 4-2.**a**: if the

external stimuli $\dot{\Omega}_{ext}$ is larger than the intrinsic ageing (*i.e.* energy dissipation) $\dot{\Phi}_{intr}$, then the

system will move upwards on the map. However, such an energy increase will not be

maintained at a constant rate because, as E_{IS} increases, the intrinsic term $\dot{\Phi}_{intr}$ becomes larger,

resulting in a slower net gain rate of E_{IS}. When absolute values of the intrinsic and external

terms become equal, the system reaches a steady state and the energy is stabilized at a saturated

level. From a more quantitative perspective, the system's metastability evolution and the

resultant mechanical behavior would be determined by the initial energy state, the stimuli

strength, and temperature.

Figure 4-4 shows the GB's energetic evolution at room temperature and under an

external stimulus of $1.0 \times 10^{14} \, mJ/m^2/s$. The choice of $\dot{\Omega}_{ext}$ is rationalized after considering the *fs*-

laser's pulse energy, pulse width, and volume fraction of affected GBs in real experiments [92].

To facilitate the comparison with the hardness measurement here we plot the inverse variation

of the system's energy (-ΔE) with respect to its initial state, because as discussed above, the

hardness of a NC system is inversely proportional to the GBs' energy. In particular, we

examined a series of cases with various initial energy states ranging from $960 \, mJ/m^2$ and 1065

mJ/m². Two notable features emerge: (i) all curves show non-linear behavior with a gradually

vanishing slope prior to saturation. This behavior has been discussed above – the net variation

rate of E_{IS} becomes slower and slower under the driving of external stimuli. (ii) A sample with

lower initial energy state can accommodate more uphill energy variation as opposed to a sample

with a high initial energy state. If we convert these to hardness values, then one should expect

that: (i) the sample's hardness should gradually reduce and eventually saturate with increasing

laser fluence; and, (ii) the hardness drop in a sample with lower initial energy state is larger

than that in a higher initial energy state sample. Note that while saturation is not always

observed experimentally, as it sometimes is precluded by material removal (ablation) at higher

laser energies, the predicted trends in Figure 4-4 are consistent with the reported experimental

measurements [92] on Cu-rich NC alloys (seen in the inset plot) and many other alloys

reflecting a diverse range of GB chemistries and synthesis routes (see **Appendix B**, **Figure.

B3**).
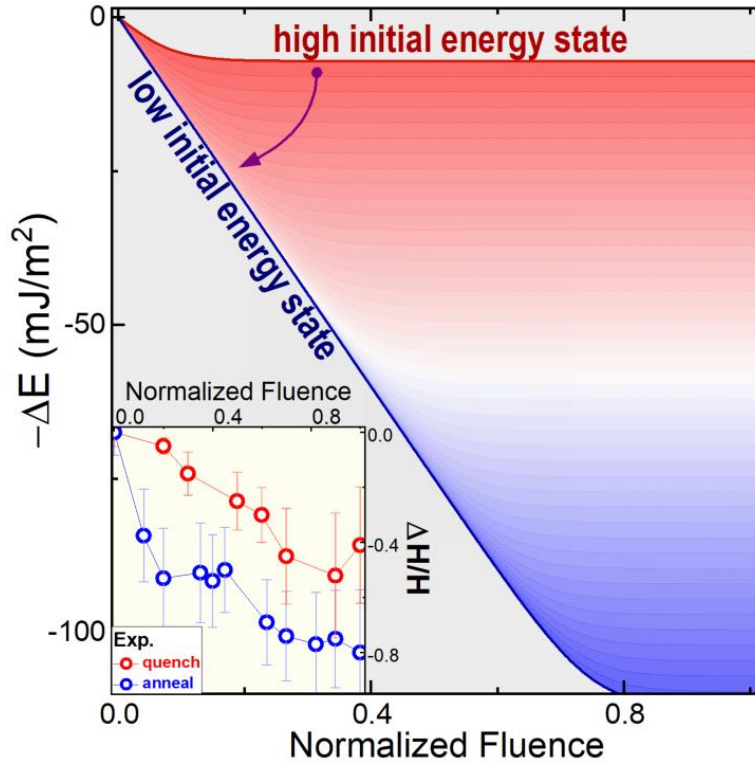
Figure 4-4. Numerically calculated GBs' energetic evolution under the external stimuli of 1.0×10^{14} *mJ/m²/s*. Here we plot the inverse variation of energy (*-ΔE*) for the convenience of comparison with the sample's hardness, which is known inversely proportional to GBs' energy. In general, the curves show a non-linear stiff-to-flat variation pattern. In addition, a sample with lower initial energy state can accommodate more variation as opposed to a sample with higher initial energy state. Such predicted features are in good agreement with recent measurements on the hardness variation of the Cu-rich NC alloys under fs laser processing (details in **Appendix. B**).

It is also worth remarking that conventional wisdom states that NC materials soften after annealing owing to grain growth. However, an emerging body of experimental evidence highlights an initial regime of hardening with increasing annealing temperature, prior to softening at the onset of microstructural evolution [83, 123-126]. While different origins (*e.g.* solute segregation and dislocation annihilation at GBs) have been proposed to explain such non-monotonic behavior, some studies [83, 127] demonstrate that the anomalous hardening

phenomenon still exists even in pure NCs and with a reduced dislocation density, suggesting that alternative mechanisms mediate this phenomenon. Figure 4-2.**a** in the present study places such an alternative perspective on a quantitative foundation. Specifically, the contour lines in the ageing regime present a clear non-monotonic feature as a function of temperature, meaning that at various annealing temperatures the system would be driven to different energy levels in a concave up shape. Consequently, the hardness should vary non-monotonically in a concave down manner, which is qualitatively consistent with the reported experiments.

We would like to clarify that here we do not directly focus on the specific strengthening and deformation mechanisms of NCs, such as nucleation of dislocations or disconnections [128-132]. Instead, we propose an energy-centric and statistical perspective to acquire a predictive implication on the metastable GBs' mechanical behaviors under various environments. The rationale behind such a perspective comes from the established fact [118, 133, 134] that the yield strengthen of NC alloys are strongly and inversely correlated with the GBs' energy. Interestingly, very recent studies [135] on the GBs containing both structural and chemical complexities also demonstrate that, from a statistical point of view it is the energetics, rather than detailed structural/chemical features, that governs the GBs' behaviors under driving conditions. Therefore, there is reason to believe the hereby developed energetic evolution model may be broadly applicable to the understanding of metastable GBs under non-equilibrium processing.

4.3.5. E_A Spectra Correlations between Various Metastable GBs

As discussed above, the energetic evolution and mechanical behavior of metastable GBs are dependent on the system's surrounding E_A spectrum in the PEL. A central question that follows is: are there unique structural signatures associated with the various GB states

responsible for the spectrum of accessible behavior? The features of the activation energy spectra

$P(E_A)\big|_{IS}$ provide an important clue. It is not difficult to imagine that, for a given GB's IS, there

should be a corresponding $P(E_A)\big|_{IS}$. However, given the complex metastability of GBs [14],

there are essentially infinite numbers of ISs and it would be impractical to sample all those

spectra. Figure 4-3 in the present study suggests a vast simplification of this problem.

Specifically, in each panel of Figure 4-3.**a** we show the spectra of two metastable GBs at the

same energy level but with different atomic structures, and the spectra are very similar to each

other. This implies that the E_A spectrum is only sensitive to the energetics of GBs' IS rather than

its detailed atomic configuration. To further verify such hypothesis, we select multiple different

metastable GBs over a broad range of energy scales and probe each of their E_A spectra using the

ART method. Figure 4-5 examines the contrasts between those spectra defined as $\Delta_{ij} \equiv$

$(\int [P_i(E_A) - P_j(E_A)]^2 dE_A)^{1/2}$, where $P_i(E_A)$ and $P_j(E_A)$ correspond to samples #i's and #j's

spectra, respectively. It is clear that, when two samples' E_{IS} are close to each other their

activation energy spectra differences are relatively small; on the contrary, if the E_{IS} of two

samples are far from each other, the spectra differences are relatively large. Such nice correlation

indicates that it might be possible to express the E_A spectrum as an explicit function of E_{IS},

$P(E_A \,|\, E_{IS})$. Although obtaining reliable and explicit formalisms for $P(E_A|E_{IS})$ is beyond the

present work's scope, it represents a rich avenue for future inquiry because of its potential in

leading to a reduced-order modeling approach for disordered material system.
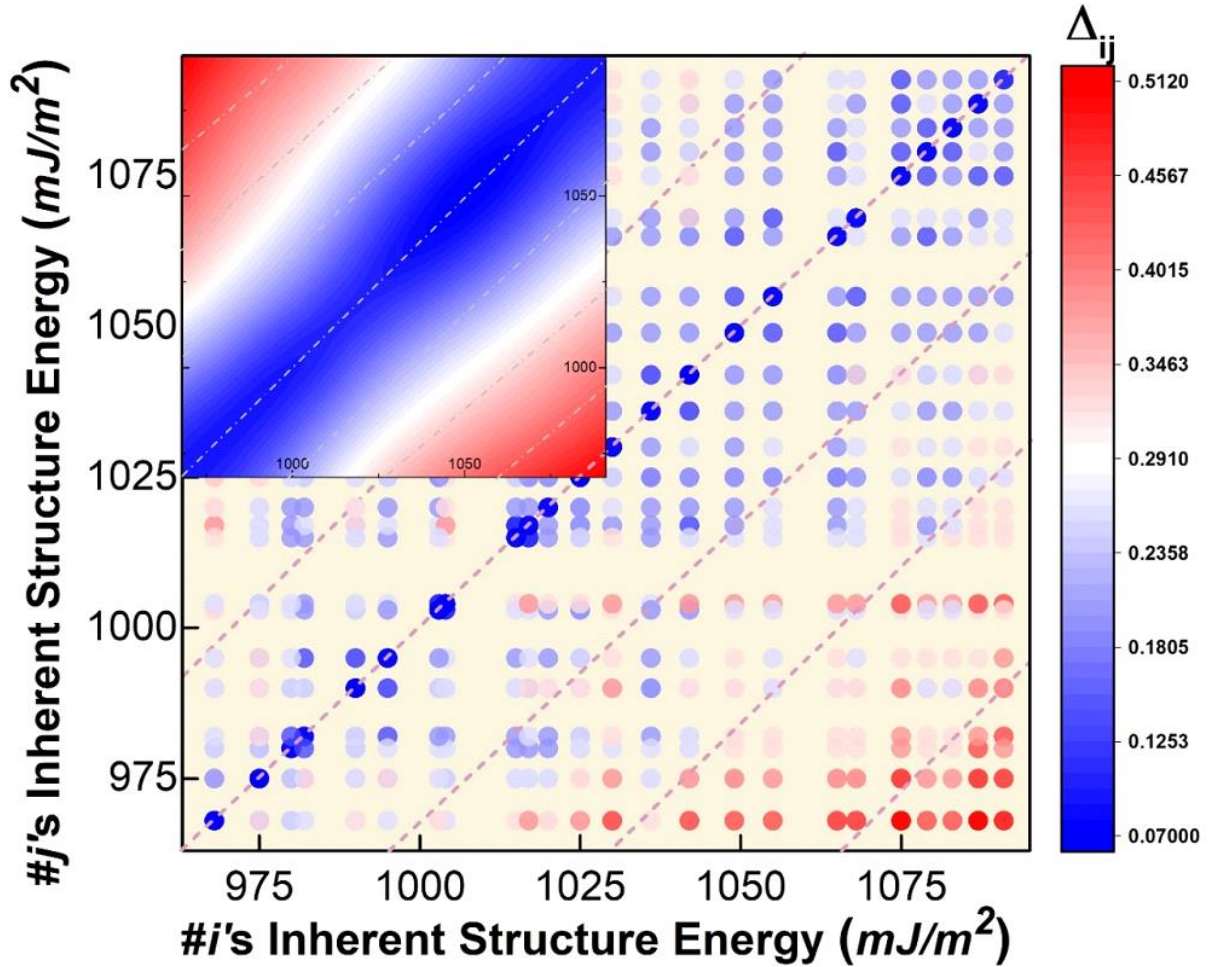
Figure 4-5. The differences between the E_A spectra among a number of metastable GBs. It is found that if two GBs' IS energies are close to each other, their E_A spectra differences are also smaller (diagonal blue data), while the opposite is true if two GBs' IS energies are far from each other (off-diagonal red data). The discrete data points are converted into the inset contour map using the thin-plate spline interpolation algorithm.

4.3.6. Discussion on Robustness of PEL Model for Metastable GBs

It would be of interest to ask whether the effective model developed above for metastable GBs can be applicable to those ground state GBs (*e.g.* perfect straight interfaces with repeating kites), and we believe the nature of E_A distribution plays an important role. More specifically,

general metastable GBs contain significant disorder and their E_A spectra are usually wide, continuous, and stretch to very low barrier (almost zero), as seen in Figure 4-3**a**. By contrast, for ground state GBs their E_A distributions should present in a much more discrete pattern with a well-defined lower bound. For example, it has been reported [112] that the E_A distribution in a perfect $\sum5$ GB in Cu displays a clear onset threshold barrier around 0.6 eV. This is not so surprising because the apparent order in perfect GBs (*e.g.* repeating kites) would impose strong restrictions and thus considerably reduce the number of available transition pathways in the PEL. According to Eq. (4.1), a threshold of 0.6 eV for $P(E_A)$ distribution means the effective activation barrier $\bar{E}_A$ can only be even higher, which is significantly larger than the effective $\bar{E}_R$ in Figure 4-3**b**. In other words, from a statistical point of view $(\bar{E}_A - \bar{E}_R)$ should always be greater than 0 in this case, suggesting the system can only move up (rejuvenation) while moving down (ageing) is practically prohibited. This actually complies with the definition of the "ground" state.

In spite of its qualitative compliance, one should not overstate the applicability of the present study onto ground state GBs. This is because Eq. (4.1) is actually derived after statistical average and thus holds a mean-field spirit. In other words, its robustness might be compromised in the absence of a wide and continuous E_A spectrum. Therefore, we believe the framework developed in the present study is more suitable to investigate general metastable GBs rather than perfect ground-state GBs.

As a final note, the hereby discovered ageing/rejuvenating evolution map for metastable GBs, and the dependence of their activation barrier spectra on E_{IS}, are strongly reminiscent of the recently observed non-equilibrium evolution in metallic glasses [106]. This is not surprising, as many previous studies have also reported the qualitative similarities between GBs and fully

amorphous glassy materials [107-110, 136]. However, we would like to remark that, the

robustness of Eqns. (4.1-4.2) demonstrated in the present study lends quantitative credence to

these similarities, which have not been fully characterized before. Even though the herein

employed EAM potential is, in principle, empirical, the spectra of $P(E_A)\big|_{IS}$ and $P(E_R)\big|_{IS}$

presented in Figure 4-3.**a** are directly obtained using an atomistic algorithm rather than through a

numerical fitting with free parameters. Given this, we see considerable promise in such a

"bottom-up" PEL-oriented model for establishing quantitative structure-property relationships in

metastable GBs and other disordered non-equilibrium materials.

4.4. Summary

Our present studies on the metastability evolution of bicrystal-GBs subjected to non-equilibrium conditions allow us to draw the following conclusions:

- The energetic evolution of metastable GBs over the broad E_{IS}—T parameter space can be distinctly divided into an ageing regime $(\partial E_{IS}/\partial t)\big|_T < 0$, and a rejuvenating regime $(\partial E_{IS}/\partial t)\big|_T > 0$, respectively.

- Such ageing/rejuvenating mechanism map is universal, irrespective of the actual stimuli used to elicit the metastable GBs.

- The ageing/rejuvenating crossover stems from the energy disparity during the elementary transitions in the PEL, which can be characterized by an effective kinetic model.

- Without invoking free fitting parameters, such kinetic model is able to capture the energetic and mechanical responses of metastable GBs to external stimuli. It can naturally explain the intriguing phenomena observed in recent *fs*-laser experiments, namely the non-linear dependence of hardness variation on the laser fluence and the processing history effect.

We would like to note that many studies have demonstrated the strong correlations between GB relaxation and the mechanical performance of NC alloys. Therefore, the capabilities established in the present study might provide a new perspective on controlling kinetic pathways for achieving a plurality of interfacial states with desired mechanical performance for various applications such as AM.

Chapter 5 Universal Trend in the Dynamic Relaxations of Metastable Tilted Grain Boundaries under Ultrafast Thermal Cycles

Last chapter we focus on the energetic evolution of GBs over a broad metastability-temperature space, while in this chapter we mainly study the non-equilibrium relaxation and structural evolution with extended GB types under ultrafast thermal cycles. Specifically, here we investigate the responses of a multiplicity of bicrystal tilted GBs in Cu subjected to ultrafast thermal cycles comparable with the selective laser melting or *fs*-laser irradiation environments. Moreover, asymmetric GBs and another material Ni are also studied. Most notably, in the rapid cooling stage we discover a scaling relationship between GBs' inherent structure energies and their critical structural transition temperatures. These findings provide a foundation to assess the tunability of different metastable tilted GBs and predict their most effective processing windows. It may hold the promise for a new route to harness the properties of interface-dominant systems without changing the macroscopic textures in producing nanocrystallines during AM.

5.1. Introduction

GBs, as one of the most common solid-solid interfaces, determine many important properties of poly-/nano-crystalline materials [80, 82, 83, 87]. In terms of the macroscopic degrees of freedom, GBs are usually characterized by 5 independent angular parameters representing the misorientation between neighboring grains. In the past, extensive efforts have been made on probing the thermodynamic equilibrium atomic structures and properties of GBs at different misorientations [88, 137, 138]. Consequently, the conventional wisdom of GB-

engineering strategy has been focused on creating and controlling the relative fraction of GBs with special coincident site lattice structures (e.g. twin or other low-Σ boundaries) [139].

Recent theoretical studies [14] have demonstrated that a given GB, even with its macroscopic misorientation angle fixed, can possess essentially infinite number of metastable microstates. This marks the insufficiency of traditional focus on the equilibrium structures, and such an issue becomes more critical when extreme environments are imposed. For example, recent experiments demonstrate non-equilibrium processing can remarkably change GBs' behaviors without affecting their macroscopic features. Specifically, pulse *fs*-laser irradiation can significantly change the nano-crystals' hardness with negligible variations in grain sizes [92]. Recent additive manufacturing (AM) experiments [8] also suggest that, the very rapid heating/cooling cycle can create non-equilibrium states of GBs with remarkably high diffusivity ($10^{4\sim8}$ times faster than usual) without discernible changes in grain sizes and orientations. These studies collectively envisage a new school of thought on GB engineering – a way to manipulate the metastable microstates of GBs without changing their macroscopic textures. In the meantime, such a prospect also prompts fundamentally new challenges on understanding the behavior of metastable GBs under extreme environments.

5.2. Methodology and System Set Up

We first create a variety of "ground-state" GBs in Cu with EAM potential [93] via the bicrystal set-up protocol [94, 96, 140]. Mis-oriented upper and lower crystals are combined through rigid in-plane translations and occasional atom deletions to identify the lowest energy states and configurations. Note that our ground-state structures and energetics calculations at different misorientation angles are well consistent with earlier studies [94, 141]. Fast heating and

cooling (0K→1300K→0K at 10K/ps) are then imposed to the so-constructed static GBs, and their energetics and structural evolutions are consequently scrutinized. Note that the temperature changing rate here is not unrealistic in scope of non-equilibrium processing [97, 120, 121]. The upper bound of temperature is set deliberately below the bulk melting point (~1350K), because we would like to keep the constraints of macroscopic textures while focusing on the evolution of GBs' metastable microstates. Also note that the atoms number in the simulation box keeps fixed, because the ultrafast stimuli will drive the system out of equilibrium, and one should not assume a grand canonical ensemble. Figure 5-1 shows the evolution of inherent structure (IS) energy during the thermal cycle over different types of GBs (details of tilting axes and misorientation angles in Appendix C, Table C-1). More details about the set-up would be discussed in Appendix C and the system size effect during the non-equilibrium processing is also studied (Figure C-1 in Appendix C).

5.3. Results and Discussion

5.3.1. Universal Hysteretic Behavior in Tilted GBs

In Figure 5-1, despite of a wide range distribution of energetics across various GBs, there clearly exhibit some universal features: (1) At low temperatures the curves are almost in perfect arches with invariant radii (i.e. E_{IS}), reflecting the kinetically arrested stage; (2) At high temperatures there present significant energy fluctuations while the radii are ramping up, yielding a cluster of skewed curves. As will be discussed below, this reflects the ISs of GBs are becoming increasingly more disordered via atomic rearrangements near interfaces; (3) Most notably, the curves are not closed loops after the thermal cycle; instead, the upper and lower halves in Figure 5-1 are off from mirror symmetry. More specifically, a universal hysteretic

59

behavior exhibits, and the E_{IS} of GBs shift to higher values after cooling than they were initially located, corroborating the rejuvenating responses of nanocrystals under pulse *fs*-laser processing [92]. It is also worth noting that, in high temperature regime there exist frequent crossovers among various curves, indicating very complex and diverse relaxation behaviors of different GBs at extreme conditions. In what follows, we report the discovery of a scaling relationship that can delineate these complex relaxations.
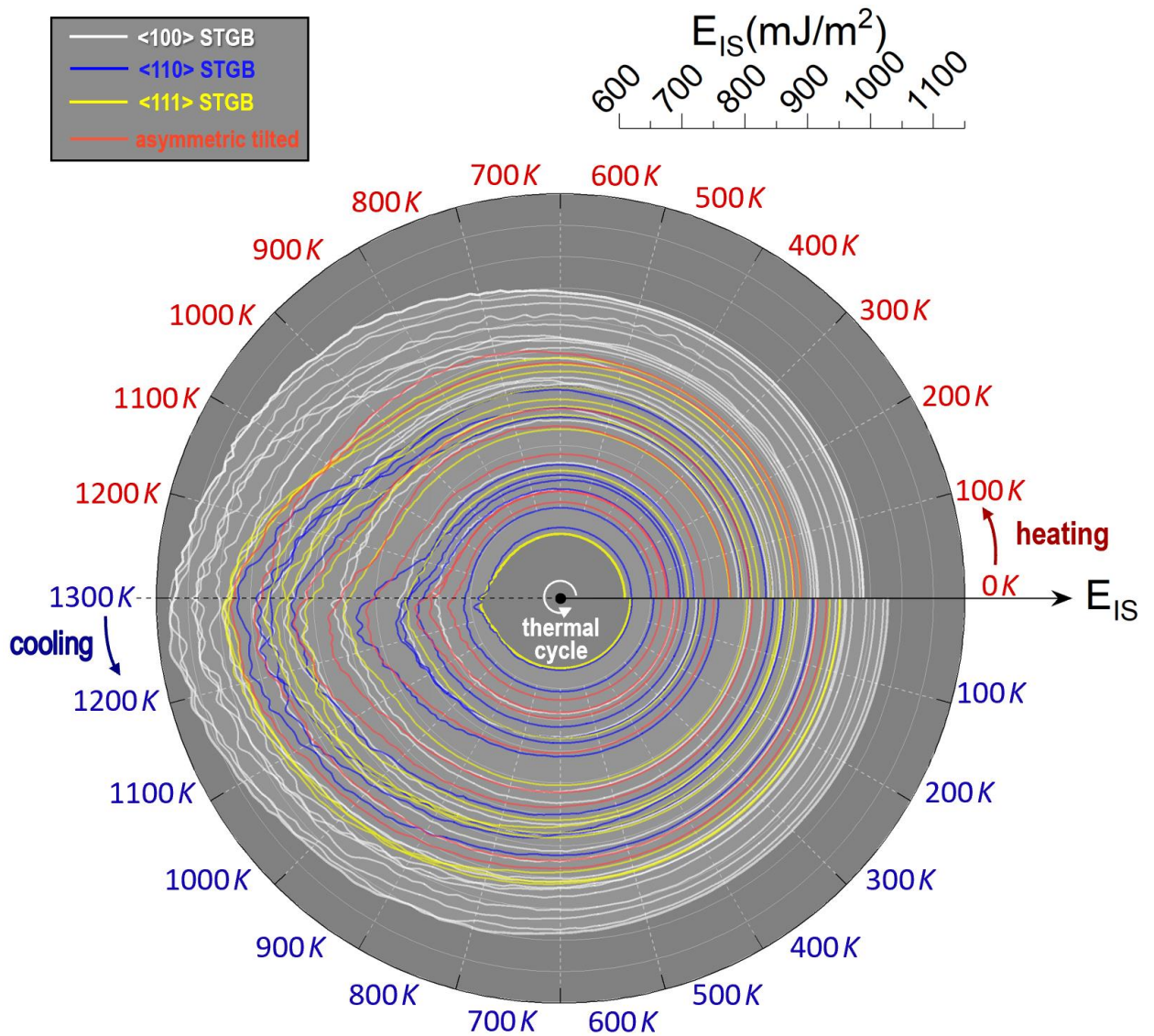
Figure 5-1. Inherent structure energy evolution under rapid thermal cycling (0K→1300K→0K at 10K/ps) for various types of GBs.

5.3.2. Transition Temperature Characterization and Activation Barrier Exhibition from PEL

Figure 5-2.a-b presents a case study on the $\sum 5$ (310) <100> STGB. Its hysteretic E_{IS} evolution is clearly seen in Figure 5-2.a1. There are only limited overlaps between the heating and cooling stages around 1100~1300K, because at such high temperatures equilibrated GB structures can be achieved even within very short timescales. Beyond that regime the cooling curve significantly deviates from its heating counterpart, and the system eventually freezes at a higher energy level after the processing. We also did a benchmark study in a single Cu crystal at the same condition and found its E_{IS} stays constant throughout entire cycle, and the heating/cooling process is completely reversible. Such a benchmark therefore verifies the hereby observed hysteresis is not an artifact in MD simulation; instead, it reflects the strong coupling between the extreme stimuli and the accessible metastable states of a GB.
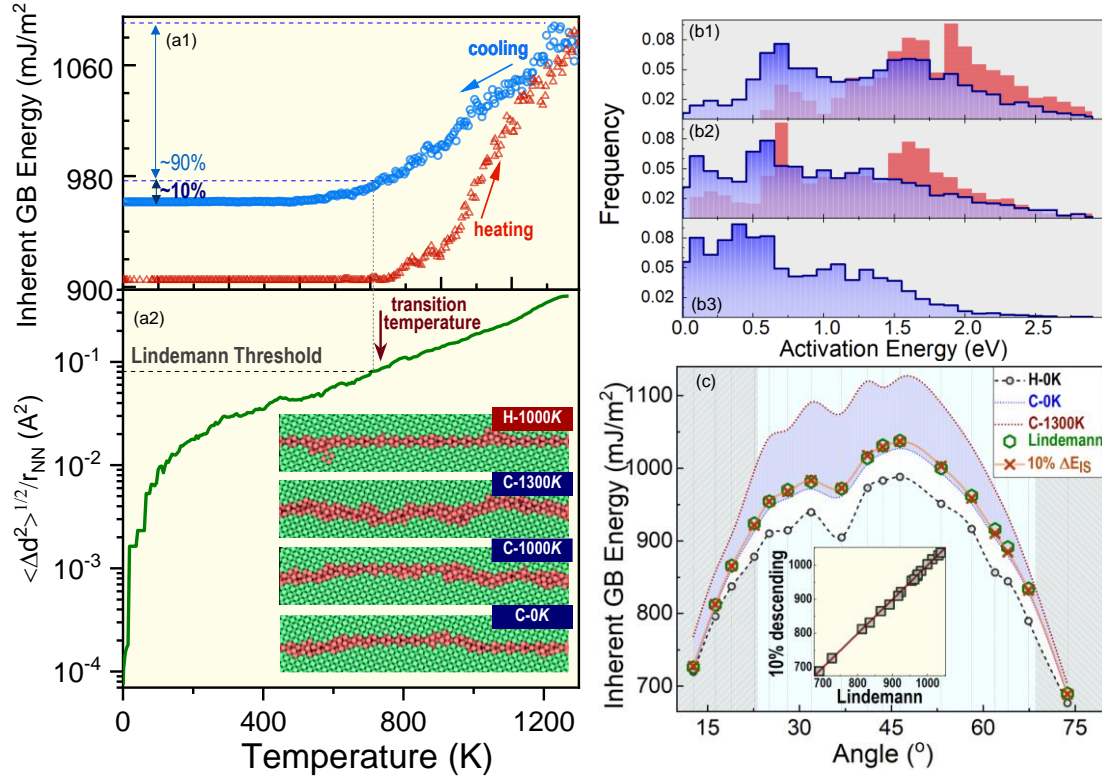
Figure 5-2. (a1) E_{IS} evolution for $\sum 5$ (310) <100> STGB. (a2) The average atomic square displacement (normalized by nearest neighbor distance) of non-FCC atoms during the cooling process. Inset: selected ISs at different temperatures during the heating-cooling process. Non-FCC atoms (red) are distinguished by the common neighbor analysis. (b) Activation energy spectra for the selected ISs. (c) Variations of E_{IS} for all <100> STGBs considered in the present study. The green circles represent the E_{IS} at Lindemann threshold, namely $\sqrt{(\Delta d^2)}/r_{NN}=0.08$. The orange crosses represent the 10% descending energy illustrated in (a1). Inset: strong overlap between the Lindemann extraction and 10% E_{IS} descending line.

Along with energetics variation the GB's atomic structure also keeps evolving, and a higher E_{IS} state is usually associated with a more disordered configuration. To quantify the microstructural evolution, Figure 5-2.a2 shows the average atomic square displacement of non-FCC atoms. Specifically, we calculate the average square atomic displacement between two successive ISs on the fly as:

$$< d^2 > \equiv \frac{1}{N_{non-FCC}} \sum_{i=1}^{N_{non-FCC}} [(x_i^n - x_i^{n-1})^2 + (y_i^n - y_i^{n-1})^2 + (z_i^n - z_i^{n-1})^2] \quad (5.1)$$

where (x_i^n, y_i^n, z_i^n) represents the atom #i's Cartesian coordinate in the current frame of IS, while

where $(x_i^{n-1}, y_i^{n-1}, z_i^{n-1})$ represents its coordinate in the previous IS frame. $N_{non-FCC}$ represents

non-FCC atom numbers, as an effective measure of particles in GB. As seen in Figure 5-2.a2, the

average atomic displacement at high T is comparable with nearest neighbor distance (r_{NN}),

suggesting a drastic structural variation; while at low T its value is rapidly decaying. Here we

borrow the spirit of Lindemann criterion as a characteristic threshold of structural change. The

Lindemann criterion can vary between 0.05~0.20 [142, 143] across different systems, and here

we adopt the value of 0.08 retrieved from a recent systematic study on both 2D and 3D systems

[144]. The corresponding temperature at $\sqrt{< d^2 >}/r_{NN}$=0.08 can thus be regarded as a critical

structural transition temperature T_{tr}, above which the GB's configurations and properties are

dynamically evolving, while below which they would present an enhanced metastability. This is

consistent with the energetics inspection in Figure 5-2.a1, where E_{IS} descends mostly (~90%)

above T_{tr}, compared with only 10% further drop below it. Such a measure can also robustly

apply to other GBs, as supported by Figure 5-2.c and the inset plot, where the Lindemann

extraction and the 10% E_{IS} descending line are almost always overlapping.

Figure 5-2.a's inset shows a few selected ISs at various heating/cooling stages. The very

initial ground-state configuration (denoted as H-0K below) is not presented here, because it is a

well-known structure made of repeating kite units [79, 94, 145]. It is worth noting that our

ground state GB energy calculations for different misorientation angles are well consistent with

earlier studies. When the system is heated to 1000K, some dispersed fluctuations emerge while

the overall GB remains thin and straight (H-1000K). At 1300K, where heating ends and cooling

starts, the IS becomes thicker and distorted (C-1300K). Apparently, disorders are accumulated

and the repeating kite units at low temperatures no longer exist, corroborating the "smooth-to-rough" transition [146-148]. When the system is cooled to 1000K (C-1000K), the GB's thickness is reduced while the curvature and disorder remain elevated. When the system is eventually cooled back to 0K (C-0K) the GB turns thin and smooth again, but it cannot recover the ground-state configuration, leaving behind a kink structure. The reason that the system does not recover the ground-state configuration is due to the mismatch between two timescales: namely the intrinsic relaxation timescale for a given GB to reach its thermodynamics equilibrium structure through atomic reconfigurations, and the extrinsic timescale imposed by the processing condition (*e.g.* the rapid cooling). More specifically, the GB tries to find its ground state (*i.e.* the repeating kite units) during the cooling stage but cannot fully achieve so because of the exceedingly longer intrinsic relaxation timescales at low temperatures and subsequently its mismatch with the permissible extrinsic timescales.

5.3.3. Analysis of Free Volume of Metastable GBs and Diffusion Boost Factor

Earlier studies demonstrate that, for ground-state GBs with different misorientation angles, their energetics positively correlate with excess free volumes [138, 149]. These previous studies focused on the GBs' energetics and free volumes at different macroscopic orientations rather than at different thermal processing stages as we probed in the present study. The key difference is that previous studies [138, 149] primarily investigated the equilibrium structures/energetics of various GBs, while the primary focus of our present study is on how those ground-state GBs are driven out of equilibrium under extreme stimuli and how the structures and degrees of their metastability quantitatively change during the processing. Therefore, the scopes between our present study and the previous studies are largely different

64

and such a trend no longer holds in the present study. Figure 5-3 shows the free volume distributions of GB atoms (defined as Voronoi volumes ratio between non-FCC and FCC particles) at different processing stages. There are only 4 distinct local environments in the initial state (H-0K), due to the above-mentioned repeating kites. Under fast thermal cycling the free volume distributions become much broadened, indicating more disordered configurations. However, the average $\Omega_{non-fcc}/\Omega_{fcc}$ values (i.e. vertical lines) only change little, in stark contrast to Figure 5-2a's significant energetics variations. Note that the previous studies focused on the equilibrium states of GBs. Therefore, the present study indicates a qualitatively different behavior at far-from-equilibrium conditions, that is, the metastability of non-equilibrium GBs are disorder-driven rather than free volume-driven. Interestingly, such a disorder-driven mechanism aligns with recent studies of ceramic nanocrystals under ion irradiations [150]. It is also worth noting that this discovered disorder-driven mechanism only refers to the extreme environments rather than at equilibrium conditions as investigated in previous studies.

Many important properties of GBs – including diffusion, migration, and strength – are controlled by activation barriers of collective atomic rearrangements inside the boundaries [138, 151-156]. Therefore, we probe the distributions of accessible activation barriers for the above-selected ISs using an energy landscape sampling algorithm [104, 112, 157-159], as shown in Figure 5-2.b. At first, the activation barriers show broad spectra rather than explicit values. This can be attributed to the break of translational symmetry in single crystals and/or the disorders at GBs, which is not surprising. Secondly, by comparing through Figure 5-2.b1-b3, it is clear that the activation energy spectra vary significantly at different stages, and that a metastable state with higher E_{IS} yields a smaller effective activation barrier. This is understandable because, as

shown by the configurations in Figure 5-2.a, higher-energy metastable GBs are more random and disordered, where the emergence of easily accessible activation pathways can be expected.

To quantify the kinetic boost factor between the post-processing and pre-processing states (C-0K vs. H-0K), one can compute the Boltzmann factor-weighted integral of the two activation barriers spectra in Figure 5-2.b1 as:

$$\alpha(T) = \frac{\int P(E_A|C-0K) \cdot e^{-\frac{E_A}{k_B T}} dE_A}{\int P(E_A|H-0K) \cdot e^{-\frac{E_A}{k_B T}} dE_A} \tag{5.2}$$

Note that very recent isotope diffusion measurements demonstrate non-equilibrium states of GBs in rapidly cooled alloys can exhibit diffusivity $10^{4\sim8}$ times faster than that in regularly annealed GBs [8]. Markedly, plugging the same measurement temperature (500 K) into Eq.(5.2) yields a boost factor of $6.5*10^5$, which is in line with experiments.
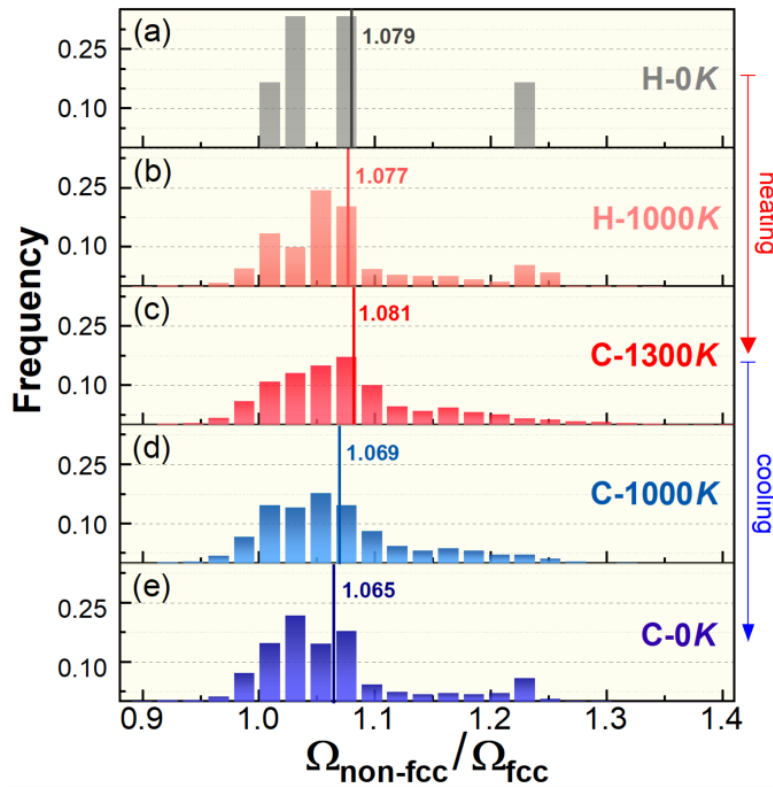
Figure 5-3. The distributions of Voronoi volume ratios between non-FCC particles (GBs) and FCC particles (bulk) at different processing stages.

5.3.4. Displacement Field of Energy-Landscape Driven

The diffusions in GBs are believed to be mediated by free volumes [160, 161]; however, the negligible free volume variations seen in Figure 5-3 indicate a different picture for non-equilibrium GBs. To unravel the underlying physics, we examine the displacement fields for the elementary atomic rearrangements retrieved from energy landscape sampling (details in Appendix C, Figure C-2). It is found that the unit processes of particle reconfigurations are in general more collective and accompanied with smaller magnitude of displacements in a higher-energy metastable state than that in a lower-energy state (Figure 5-4.a1 vs. a2). Fig.4.b shows the Euclidean norm distributions for the atomic displacements at different processing stages. It is evident that a higher-energy metastable GB exhibits a more extended tail distribution on the left side, indicating a rougher energy landscape with higher fraction of easily accessible and low-cost reconfiguration processes. Such a free volume-insensitive and energy landscape-driven picture closely resembles the excitations in metallic glasses [106, 162].
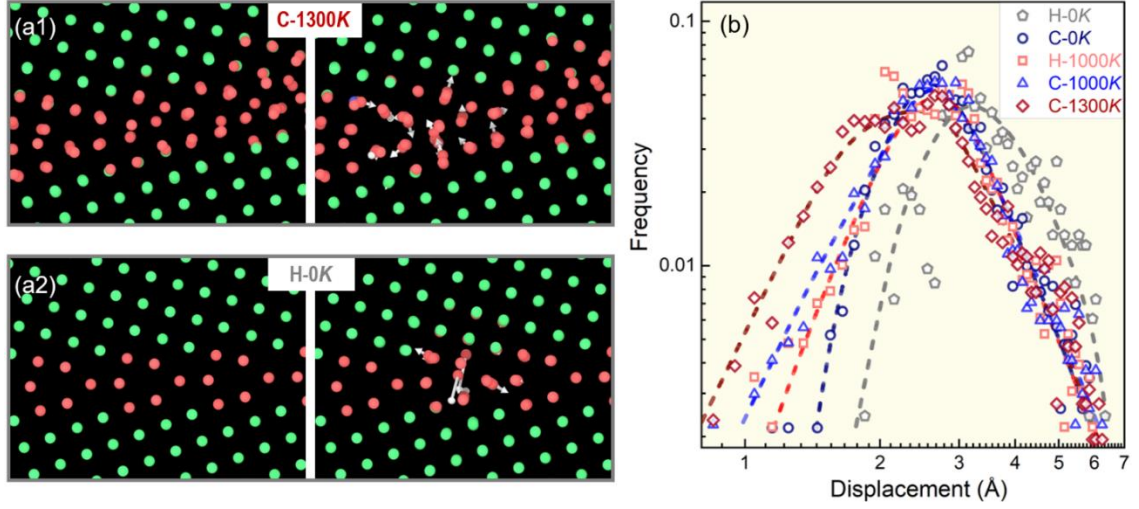
Figure 5-4. (a1-a2) Displacement fields (white arrows) of two exemplified elementary atomic rearrangements events inside GBs in a high energy state (C-1300K), and a low energy state (H-0K), respectively. (b) Euclidean norm distributions of GBs' atomic rearrangements at different processing stages.

5.3.5. Scaling Correlation between IS Energy and Transition Temperature

To probe the correlation between a given GB and its T_{tr} during the fast-cooling stage, and to better contrast the relaxations in different GBs, in Figure 5-5.a we plot the rescaled IS energy variations of the group of <100> STGBs, $\hat{E}_{IS}(C-T)$, which is defined as:

$$\hat{E}_{IS}(C-T) = \frac{E_{IS}(C-T) - E_{IS}(C-0K)}{E_{IS}(C-1300K) - E_{IS}(C-0K)} \tag{5.3}$$

where "C" refers to cooling and "T" represents the temperature. Note that a few low-angle GBs are excluded in Figure 5-5.a, and it will be discussed later.
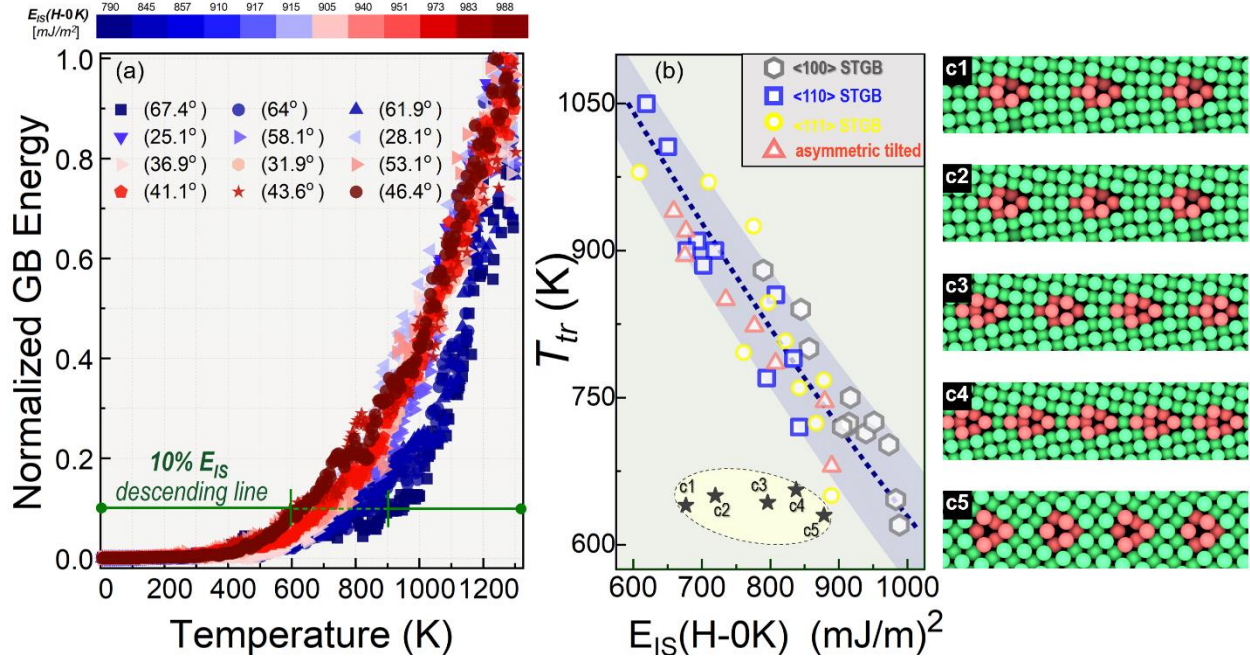
Figure 5-5. (a) $\hat{E}_{IS}(C-T)$ for different <100> STGBs. The data for each GB is colored according to its pre-processing energy at H-0K. T_{tr} is measured when $\hat{E}_{IS}(C-T)$ reaches 10%, as marked by the green line.(b) The correlation between E_{IS}(H-0K) and T_{tr} for various GBs. A few outlier points labelled by the grey filled stars correspond to low angle GBs shown in c1-c5 (H-0K configurations), whose misorientation angles are 12.7°, 16.3°, 18.9°, 22.6°, and 73.7°, respectively.

As seen in Figure 5-5.a, in general the curves are rather steep at high temperatures and become much flatter at low temperatures. However, different GBs show different energy variation rates and the entire cluster of curves span into a crescent-shaped region. If one colors the curves according to the GBs' pre-processing energy $E_{IS}(H-0K)$, then a clear trend reveals by itself: the curves associated with lower $E_{IS}(H-0K)$ values (more blue) tend to be leaning toward the right edge, suggesting narrower windows for the changes of atomic structures and properties during the fast cooling stage. To be more quantitative, the T_{tr} of a GB is measured by the intersecting point between its $\hat{E}_{IS}(C-T)$ curve and the afore-mentioned 10% energy descending line (green line in Figure 5-5.a). Figure 5-5.b shows the correlations between

$E_{IS}(H - 0K)$ and T_{tr}, where a clear monotonic correlation exhibits. This notable finding

indicates that, as long as a GB's ground-state energy is known, one can then predict the

tunability of its metastable states when subjected to ultrafast thermal cycle.

We would like to emphasize that, due to the non-equilibrium nature, in principle there

could be various ways of defining the T_{tr} (*e.g.* cooling stage extraction vs. heating stage

extraction) and correlating it with differently assessed $\hat{E}_{IS}$ (*e.g.* ground state H-0 K vs. post-

processing state C-0 K). More details are shown in Appendix C, Figure C-3. Here we focus on

the cooling stage and the $\hat{E}_{IS}$ at H-0 K state for the following considerations: (i) In many non-

equilibrium processing techniques, such as ultra-fast laser irradiation or additive manufacturing,

the final step and arguably the most properties-determining step is the rapid cooling stage.

Therefore, we believe the cooling stage should be more meaningful than the heating stage; (ii)

Compared with any other non-equilibrium states during or after the extreme thermal stimuli, H-

0 K samples represent the ground states that can be unambiguously obtained both in experiments

by slow annealing and in atomistic modeling by well-defined protocols [94], making them as

good reference states.

To further examine the universality of such correlation, in Figure 5-5.b we also add other

GBs considered in the present study, including a number of <110> and <111> STGBs, as well as

some asymmetrically tilted GBs. Evidently most data points fall into a narrow band, indicating a

strong and universal correlation between the two variables. It is known that Cu has a medium-to-

low stacking fault energy, and to further assess the applicability of the hereby obtained results we

also investigate a group of GBs in Ni [163], a system with relatively higher stacking fault energy.

A similar correlation persists there (Figure C-4 in Appendix C), which gives reason to expect the

present study may apply to other materials as well.

5.3.6. Discussion on thermos-mechanical effects on GBs

It is worth noting that the overall motion of GBs is not investigated and their net velocities are statistically zero in the present study. Many previous atomistic modelling studies have been investigated to extract the structures and velocity/mobility of GBs, where an artificial driving force is applied to the system. However, only ultrafast thermal stimuli and no global mechanical driving forces are applied in our simulations. Therefore, GB mobility is not considered in our present study and the primary focus is on the structural evolution of non-equilibrium GBs and their intrinsic activation barriers for atomic rearrangements under extreme environments.

Admittedly, there are new questions prompted. Figure 5-5.b contains a few outliers (filled stars), whose T_{tr} do not exhibit strong dependence on $E_{IS}(H-0K)$. This may indicate the low-angle GBs consisting of dislocation arrays (Figure 5-5.c) would present qualitatively distinct responses to extreme stimuli compared with those high-angle 2D planar GBs. The underlying physics for such fundamental difference, however, yet remains to be explored. In addition, to highlight the impact of microstructural metastability, this work does not present complications resulting from chemical complexity. While single-element model can well capture many important physics relevant to real alloys [24, 110, 133], we also realize that solutes may largely impact GBs' metastability [164, 165] and impose complex chemo-thermo-mechanical coupling. Last but not least, in the present study we only focused on extreme thermal stimuli but did not introduce any global mechanical driving forces introduced in the simulations. This sets a distinction both from the conventional grain coarsening behaviors, where the capillary force often serves as the main driver to the motion of curved GBs; and from many previous atomistic

modeling studies [128, 166], where an artificial bias/driving force is applied to the simulation to extract the structures and velocity/mobility of GBs when a steady state is reached. In other words, the thermo-mechanical coupling effects on the metastable GBs still remain unknown. These challenges would warrant future studies.

5.4. Summary

We have demonstrated that the energetics and kinetics evolution of metastable GBs under extremes are very different from those in equilibrium or near-equilibrium states. Free volume only plays a minor role here, and the evolution is mainly driven by disorder and rough energy landscape. Importantly, a universal scaling is observed between the GBs' inherent structure energies and their T_{tr} during the rapid cooling stage. The discovery herein is noteworthy, not only because it enables an increased control over how the metastable microstates and properties of GBs can be effectively tuned in advanced processing such as additive manufacturing and *fs*-laser irradiation, but more critically it suggests the importance of E_{IS} as a robust parameter to delineate the complex relaxation behaviors of GBs under non-equilibrium environments. There is already evidence that the energetics of GBs are more effective than their detailed morphologies in determining the system's strength [135, 167] and mobility [135]. Our present study therefore lends further credence to such a notion. Note that the significance of E_{IS} is well appreciated in amorphous materials [106, 167, 168]. It has been quantified that, regardless of the samples' processing histories and detailed configurations, as long as they exhibit similar E_{IS} then their mechanical and kinetic properties are close to each other [169]. Considering many similarities between GBs and glasses [92, 110, 111], one may believe E_{IS} would play a decisive role in the performance of metastable GBs.

Chapter 6 Summary and Future Work

6.1. Summary and Implication

In this thesis, we have employed PEL-based modeling framework to investigate the microstructural evolutions and concomitant mechanisms of structural materials at long time scales under extreme environments. Specifically, we focused on kinetic evolutions of two extremely significant defects (dislocations and grain boundaries) in structural materials from the PEL standpoint. The tackled problems are of great scientific and technological importance because the performance of structural materials in the applications of nuclear reactors and additive manufacturing is largely controlled by the kinetic evolutions of dislocations and grain boundaries.

In Chapter 3, we employ a recently-developed ABC-T algorithm based on the concept of PEL to investigate the dislocation-obstacle interaction at realistic strain rates, which are not accessible by classical MD method. Specifically, the critical resolved shear stress (CRSS) is obtained over a wide range of strain rates $10^8 s^{-1}$ down to $10^3 s^{-1}$. We observed that the CRSS of the system is determined by the interplay between thermal activation and applied strain rate. Interestingly, negative strain rate sensitivity (nSRS) behavior is observed, which might lead to mechanical degradations in nuclear reactors. We demonstrated that the nSRS is due to the different intermediate microstructures emerged during the dislocation-obstacle interaction at various strain rate conditions. This work has been published in Physical Review Letters [22].

In Chapter 4, we investigate the kinetic evolution of metastable grain boundaries (GBs) under non-equilibrium processing from the PEL standing point. The aim has been understanding and predicting the evolution of non-equilibrium metastable GBs under extreme stimuli, which is critical for the sustainability of additive manufacturing (AM). We created a multiplicity of metastable states and investigate those metastable GBs' energetic temporal evolution by isothermal annealing. The results confirmed that the evolution of metastable GBs over a broad energy-temperature space can be distinctly divided into an ageing regime, and a rejuvenating regime, respectively assisted by an effective data mining algorithm. Furthermore, it is demonstrated that such ageing/rejuvenating stems from the energy imbalance during the elementary transitions between local minima in the system's underlying PEL, similar to that in metallic glasses. Such kinetic model could explain the intriguing phenomena observed in our collaborated *fs*-laser experiments. This work has been published in Acta Materialia [24].

In Chapter 5, we investigate the non-equilibrium relaxation of tilted GBs subjected to ultrafast thermal cycles comparable with the selective laser melting or *fs*-laser irradiation environments. The key contribution is providing a foundation to process different types of metastable GBs and a new route to harness the properties of interface-dominant systems. Specifically, a universal hysteresis on energy evolution is observed in both symmetrically tilted GBs (STGBs) along different axes and asymmetrically tilted GBs. By probing the atomic configurations and energy landscape of metastable tilted GBs at various intermediate stages and resolving the activation energy spectra for collective atom rearrangements, we demonstrate a strong sensitivity of GBs' kinetic behavior to their processing histories. Most notably, in the rapid cooling stage we discover a scaling relationship between GBs' inherent structure energies

74

and their critical structural transition temperatures. This work has been published in Materials Research Letters [25].

We would like to emphasize that the PEL-based modeling techniques are capable of bridging the time scale gap from the atomic-scale to mesoscale, which is not accessible by traditional atomistic simulation methods such as molecular dynamics. Most notably, PEL-based framework is fundamentally governed by the atomic interactions without invoking empirical assumptions or fitting parameters. Therefore, such PEL-based framework could be expected to provide a more accurate and predictive modeling and bridge the time scale gap.

6.2. Future Work

Further development in complex dislocation-GB interaction via PEL-enabled multi-timescale modeling

In Chapter 3, we have investigated the dislocation-obstacle interaction under various strain rates by our developed ABC-T method from the PEL standpoint. A surprisingly negative SRS has been discovered at low strain rate regime far beyond MD's accessibility and the underlying mechanism is due to the complex interplay between applied strain rate and thermal activation. We expect that the similar spirit also holds for the dislocation interaction with metastable GBs in nanocrystalline alloys. It is well-known that dislocations and GBs are both extremely significant microstructural defects and therefore it is of great importance to investigate the dislocation-GB interaction at low strain rates by ABC-T method, which can be tested by experiments.

Microstructural evolutions of high entropy alloys (HEA) from the PEL standpoint

In previous studies, we employ PEL-based framework to investigate microstructural evolutions and underlying mechanisms of single-element metals. HEA consists of five or more principal elements and exhibits high strength and ductility. However, due to the high entropy, severe lattice-distortion, and sluggish diffusion effect, the microstructural evolution of HEA is extremely complex and therefore it is essential to extend PEL-based framework to study HEA's microstructural evolutions. We have collaborated with Oak Ridge National Lab to explore the PEL of strained HEA and obtained the spectra of activation energy barriers under different mechanical conditions via ART method. We expect to uncover the fundamental deformation mechanisms from the PEL standpoint without inserting any fitting parameters.

Appendices

Appendix A Origin of the Shear Stress Discrepancies between MD and ABC-T

It has been noted in the main text in Chapter 3 that there exists a shear stress mismatch (~80 MPa) between the ABC-T results and MD results. Such quantitative discrepancies are less likely to originate from different microstructural evolutions, because as seen in Figure A-1 below (also Figure 3-3.c in the main text), the defects configurations in both studies are the same in terms of: (a) the exact configuration of the remnant vacancy cluster; (b) the number of vacancies absorbed by the dislocation in the final configuration; and, (c) the ripped dislocation core after the interaction. Admittedly, the ripped dislocation core in MD simulation is not as sharp as in ABC-T because the random thermal oscillations of atoms in MD algorithm would smear the static configuration a little bit [51]. In addition, in spite of the value mismatch, such difference keeps consistent and almost invariable at two different strain rates (10^6 s^{-1} and 10^8 s^{-1}). Together with the same configurations identified in both ABC-T and MD, it is reasonable to believe that the mismatch might come from the thermal compression stress produced in the non-zero temperature MD simulations, because of the fixed volume condition.

Figure A-1. Detailed comparison between the obtained final configurations by ABC-T and MD, respectively, under the same conditions. We would like to stress that both studies start from the same initial configuration. It can be seen from the comparison that the microstructural evolutions in both studies are identical to each other in terms of the remnant cluster configuration, the number of vacancies being absorbed by the dislocation, and the ripped core structures in the end. Such consistency suggests that both methods are essentially capturing the same dislocation obstacle interaction mechanism. We therefore believe the thermal compression stress in MD is the main reason leading to the shear stress mismatch.

If thermal fluctuations in MD simulations are the main contributors to the stress variations, then one should expect that, by changing the temperatures in the MD simulations, even the same configuration will correspond to different shear stresses. To verify this, we conducted several parallel MD studies on the same configuration when the dislocation and obstacle just start to contact with each other. To remove any other potential factors that might affect the results, we only change the temperatures in these MD studies while keeping the shear

strain (i.e. the shape of simulation cell) fixed. Five different temperatures are studied at 0.1 K, 100 K, 200 K, 300 K, and 400 K, respectively. We would like to stress again that these MD studies are all at the same configuration. As seen in Figure A-2, the shear stresses of the same configuration give different values at various temperatures. At 0.1 K, the shear stress (-250 MPa) is almost identical to the ABC-T results shown in the manuscript because the thermal fluctuation is negligible. As we gradually increase the temperature, an enhanced deviation of the shear stress shows up, while the configurations essentially keep unchanged. At 300 K, the shear stress mismatch reaches to ~80 MPa, which is well consistent with the discrepancies we report in the manuscript.

As we mentioned, in these validating MD studies, we only change the temperatures while keeping the configuration and strain fixed. Therefore, the most reasonable explanation to the variations of shear stress is the thermal effects in MD simulations. To be more specific, since the simulation cell is fixed, at higher temperature the system would experience a larger hydrostatic compressive stress (inset in Figure A-2), and such thermal-induced pressure leads to a shift of the shear stress values, although the microstructural evolution mechanisms are not changed. It is worth noting that, according to Figure A-2, it seems the thermal effect is non-linear. This is a very interesting observation and would warrant further investigations in our future studies.
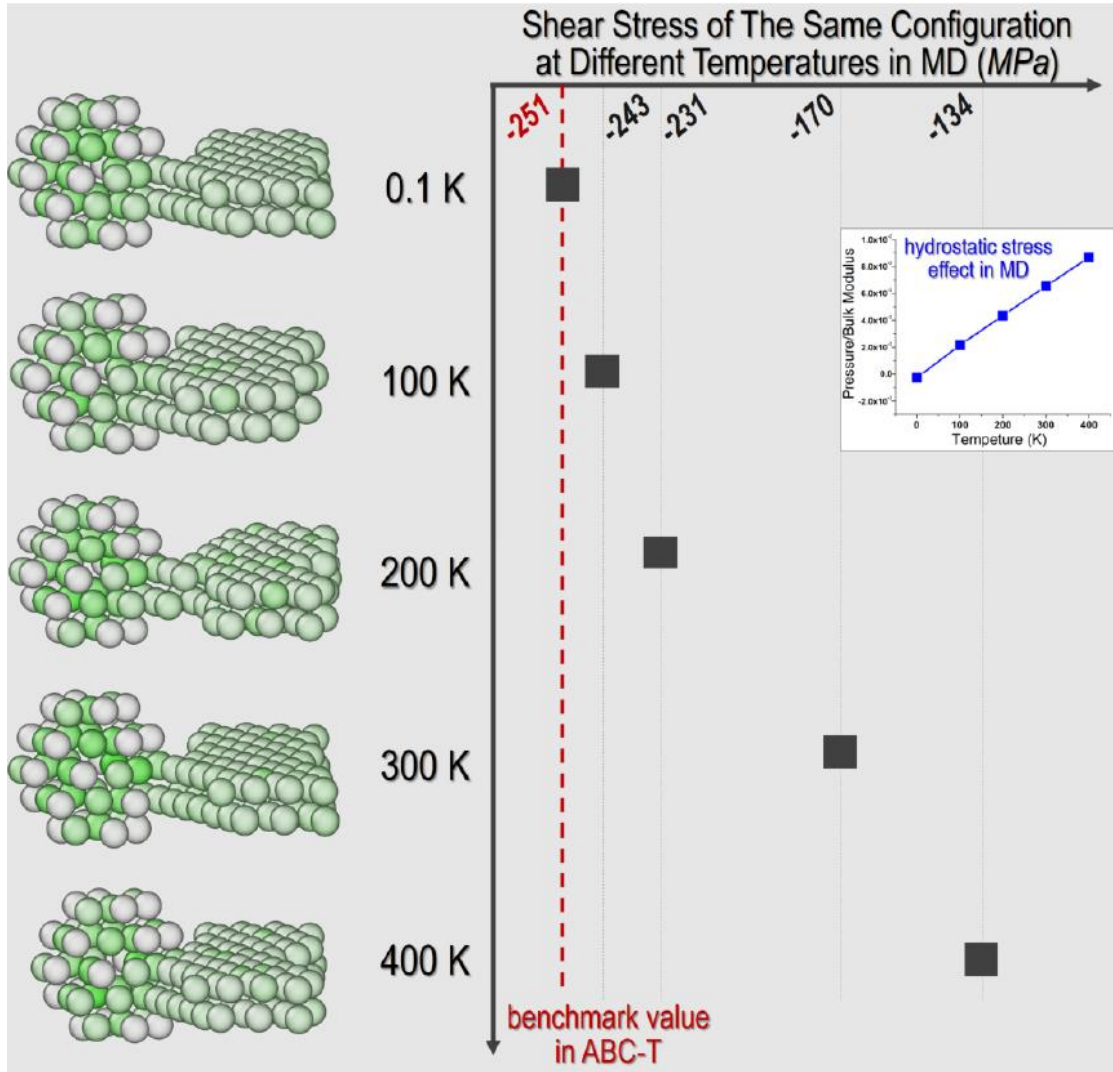
Figure A-2. Shear stresses of the same configuration in MD at different temperatures. The software Ovito [170] is used for visualization and only the atoms with distinguishing numbers of neighbors are shown (with a cutoff radius of 3.5 Å in the common neighbor analysis). The atoms are colored according to their centro-symmetry parameters [171]. It can be seen that the colors show some fluctuations at finite temperature MD simulations due to the random thermal oscillations. But the defect configurations are apparently identical with each other. Yet different shear stresses are obtained for these configurations. At 0.1 K, the shear stress value is the same as in ABC-T, since the thermal effect is negligible. And the shear stress deviations become larger at higher temperatures. Meanwhile, the hydrostatic stress keeps increasing (inset plot) since the volume of simulation cell is fixed.

In sum, we believe the thermal effects in MD simulations are the major factor leads to the quantitative differences of the shear stress values. But the qualitative mechanisms in both ABC-T and MD are well consistent.

Appendix B The Kinetic Evolution of Metastable GBs under Non-Equilibrium Processing

θ (°)	CSL	x (Å)	y (Å)	z (Å)	# of Atom	E(H-0K) [mJ/m²]	E(C-0K) [mJ/m²]
12.7	∑41(019)	327.35	262.14	14.46	104,960	719.88	722.84
16.3	∑25(017)	255.61	256.46	14.46	80,160	796.12	807.83
18.9	∑37(016)	219.89	264.25	14.46	71,040	837.58	860.52
22.6	∑13(015)	184.33	259.21	14.46	58,400	878.27	913.20
25.1	∑85(029)	333.28	267.50	14.46	108,960	910.25	944.75
28.1	∑17(014)	149.05	269.70	14.46	49,120	914.63	958.66
31.9	∑53(027)	263.17	262.75	14.46	84,480	939.56	971.56
36.9	∑5(013)	114.31	249.84	14.46	34,880	904.83	961.36
41.1	∑73(038)	308.86	246.42	14.46	92,960	972.89	1006.39
43.6	∑29(025)	194.67	273.12	14.46	64,960	983.11	1020.3
46.4	∑29(037)	275.30	275.47	14.46	92,640	988.22	1027.27
53.1	∑5(012)	80.83	241.52	14.46	23,840	951.2	993.46
58.1	∑53(059)	372.18	297.26	14.46	135,200	916.59	950.88
61.9	∑17(035)	210.78	251.60	14.46	64,800	856.53	903.65
64.0	∑89(058)	341.03	272.17	14.46	113,440	844.56	879.24
67.4	∑13(023)	130.34	262.14	14.46	41,760	789.78	828.75
73.7	∑25(034)	180.75	254.14	14.46	56,160	676.79	687.46

Table B-1. The specifics on the dimension, atom number, and the IS energy before and after the fast thermal cycling for various <100> STGBs.

The enhanced statistical algorithm of mining the energy variation rate: Figure 4-1.**b** already shows that the GB's energetic evolution is sensitive to both its IS energy level and temperature. To better quantify the system's intrinsic energy variation rate in the broad E_{IS}—T space, we have selected many different samples at different initial IS energy levels and conducted isothermal annealing simulations over a wide range of temperatures.

Figure B-1.a below shows a typical cluster of the annealing curves for one selected sample which was subject to different annealing temperatures. All the curves collapse in the beginning because, at *t=0*, the relaxation has not started yet. It is seen that the E_{IS} evolution evidently shows a non-monotonic dependence on the temperature. For example, in the regime from 300*K* to 550*K*, by increasing the temperature the GB's energy drops to a deeper level within the same amount of time, suggesting a larger ageing rate; while by further increasing the temperature to 1050*K*, the annealing curve becomes much flatter and the overall ageing rate obviously becomes smaller. By further increasing temperature, the GB's energy would become higher than its initial state, entering the rejuvenating regime. To precisely quantify the E_{IS} evolution rate, here we introduce an enhanced statistical treatment illustrated in the inset of Figure B-1. To be more specific, we calculate the slopes of neighboring data points in each individual $E(t,T)$ annealing curve. For example, the slope between the *n* th and *n+1* th points can be calculated as $(E_{n+1}-E_n)/(t_{n+1}-t_n)$, and this is essentially the ageing rate dE_{IS}/d*t* at the prescribed temperature *T* and IS energy level $(E_{n+1}+E_n)/2$. Following such an algorithm, each neighboring pair would provide an effective entry of ageing rate in the E_{IS}—*T* space, and by considering all the neighboring pairs for all the annealing curves, the statistics are significantly enhanced, as seen in Figure B-1.b. With such effective data mining process, together with the thin-plate spline (TPS) interpolation algorithm, we are then able to construct a quasi-continuum contour plot seen in Figure 4-2**.a**.

It is worth noting that, the raw data entries are not uniform in the E_{IS}—*T* space. As seen in Fig. S3.b, the data points are relatively sparse in the high energy regime. The reason is that at high energy level the ageing rate is too fast, so that the annealing curves would drop into low energy regime within very short time period, making the effective data entries in the high energy

84

regime are limited. As a result, the interpolated pixel map might have relatively large numerical

errors in the high energy regime compared to those in the low energy regime.

(a) Inherent GB Energy (mJ/m²) vs Time (ps)

Rejuvenating Regime

$$\frac{dE}{dt} \equiv \frac{E_{n+1} - E_n}{t_{n+1} - t_n}$$

1200K
1050K
950K
300K
400K
550K

Ageing Regime
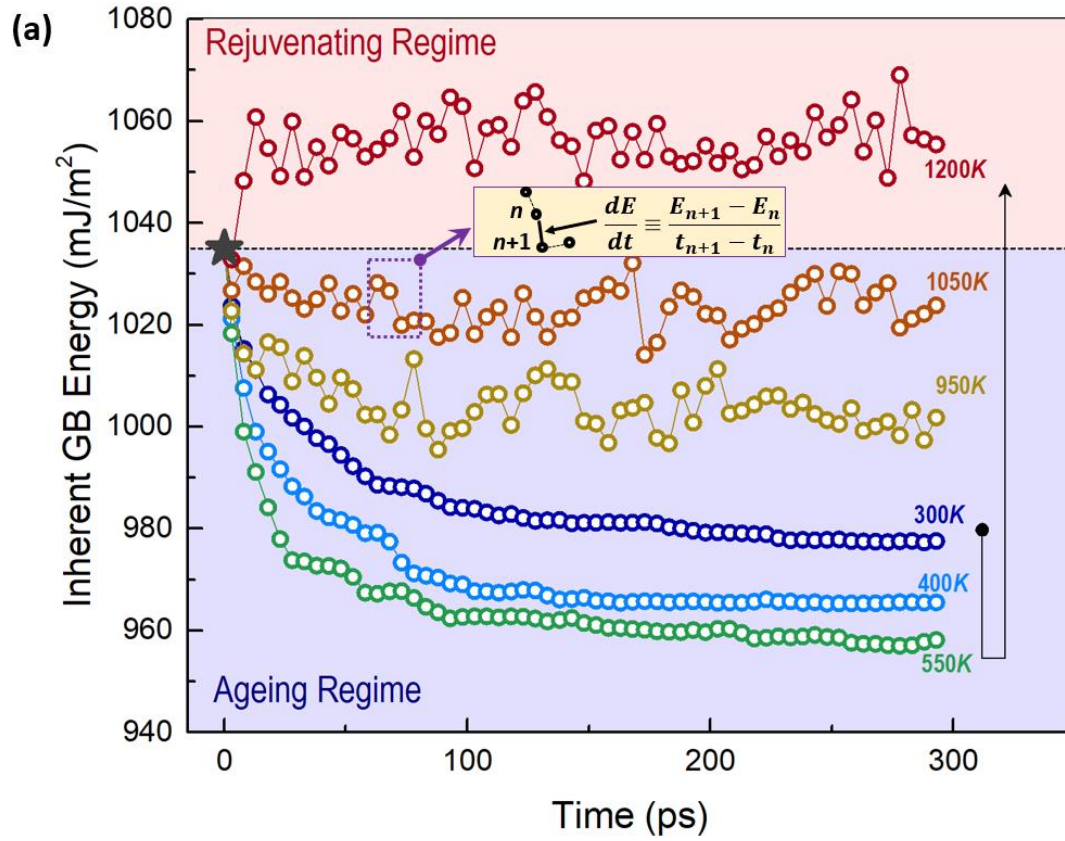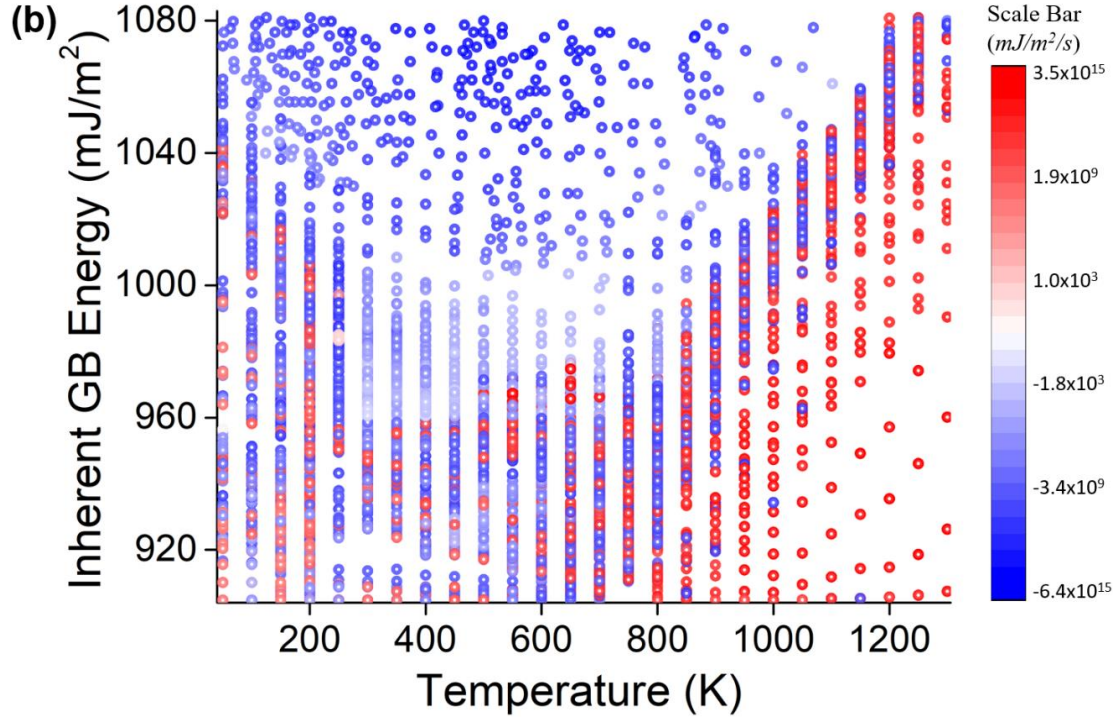
Figure B-1. (a) A typical cluster of the annealing curves $E_{IS}(t)$ for one selected GB sample which was subject to different annealing temperatures. Inset: each pair of neighboring data points would enable an effective entry of dE_{IS}/dt. (b) Scattered data of dE_{IS}/dt at prescribed temperature and IS energy states calculated from the annealing curves in (a). The 2D interpolation of these scattered data leads to the pixel map of Figure 4-2.a.

Universal hysteresis of GBs with different misorientation angles: Figure B-2 below displays the IS energy responses of 16 additional <100> STGBs during fast thermal cycling from $0K \rightarrow 1300K \rightarrow 0K$ at a rate of $10K/ps$. The heating stage is shown by red open circles and the cooling stage is shown by blue open squares. Each data point in the plot is an average of three runs with the same condition. It can be seen that, while the rejuvenated IS energy might vary quantitatively, all the GBs considered here show a clear irreversible behavior, suggesting that the hysteresis during heating/cooling is a universal behavior of metastable GBs. Details of the specific dimensions, as well as the number of atoms and the GBs' IS energy before (H-0K) and after (C-0K) the fast thermal cycling with different misorientation angles are shown below in **Table B-1.**
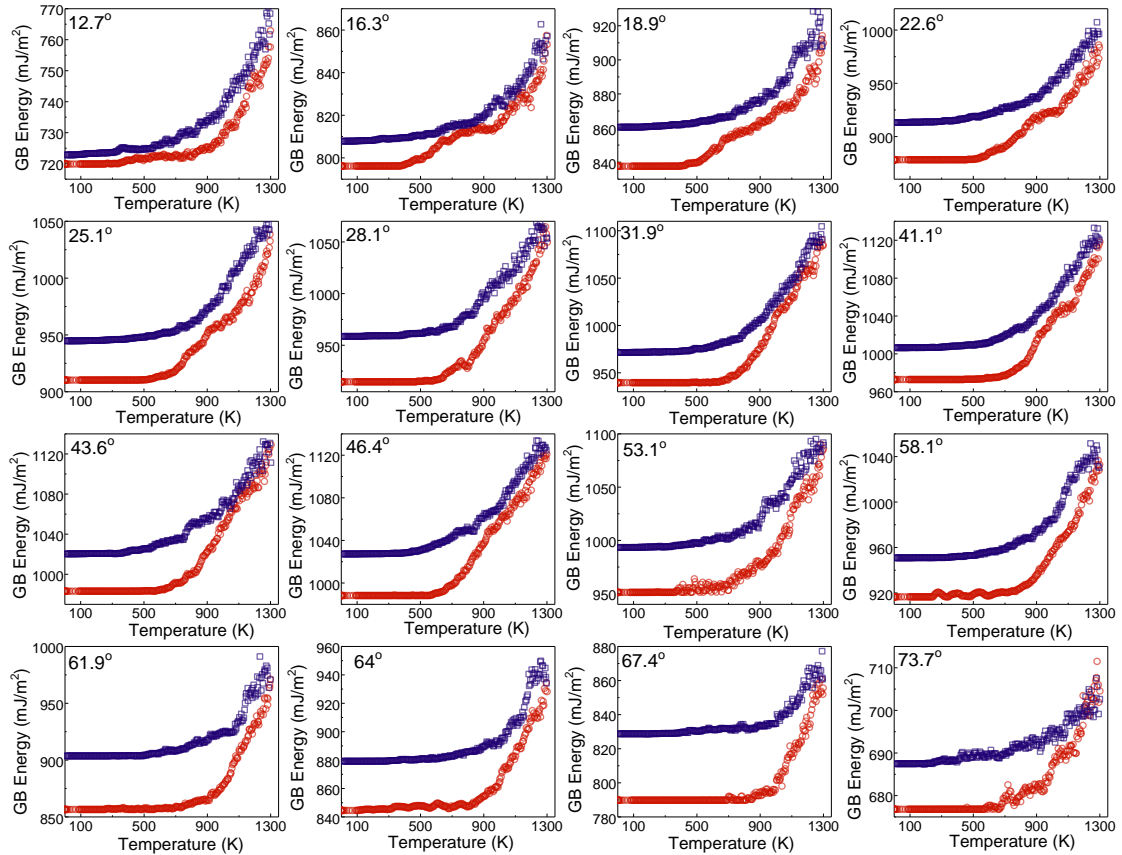
Figure B-2. Inherent energy evolution during the fast heating-cooling cycle for different STGBs with the misorientation angle ranges from 12.7° to 73.7° (the Σ5 (310) was shown in the main text and not displayed here.) The red open circles represent the heating stage and the blue open squares represent the cooling stage.

Universality of femtosecond laser behavior: We report the normalized change in hardness of two Cu-Zr based nanocrystalline samples as a function of normalized laser fluence. The data presented below finished by Gianola and his coworkers suggest that this behavior is an inherent property of grain boundaries, and thus material agnostic. Figure B-3(a-b) show the absolute change in hardness observed for the binary Cu-Zr as well as a chemically complex nanocrystalline steel prepared by high pressure torsion. Ablation thresholds are noted for each sample by the vertical dashed lines. Samples with higher energy grain boundaries exhibit

suppressed ablation thresholds and smaller reductions in hardness for both binary and chemically complex nanocrystalline materials.

Figure B-3(c) shows the normalized change in hardness as a function of normalized laser fluence for all materials investigated in this study. Figure B-3(c) is colored according to the maximum change in the normalized hardness. In the main text, we report that the Cu-Zr sample agrees well with the proposed model, where an initially relaxed grain boundary can be further rejuvenated and an initially high-energy boundary. It is clear from Figure S6, that this behavior is even more apparent in a chemically complex 316L steel. In the as-deformed state, this material undergoes a mild decrease in hardness as a result of laser rejuvenation. By relaxing the material by annealing it at 550C for 1 hr prior to laser irradiation, the material subsequently exhibits a nearly 90% decrease in the normalized hardness owing to laser rejuvenation, strongly implicating the importance of the initial GB state. Studies have shown this relaxation behavior from annealing to be related exclusively to grain boundary relaxation, rather than chemical segregation or dislocation-related phenomena [172].
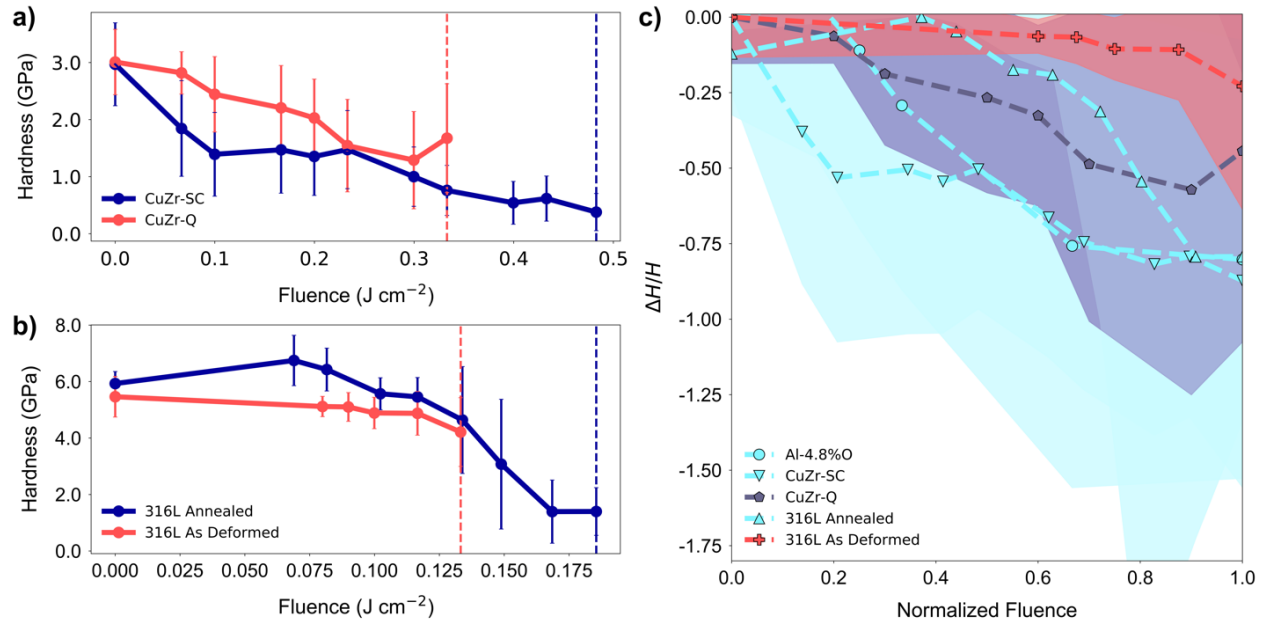
Figure B-3. (a-b) Absolute change in hardness observed for NC Cu-Zr, and 316L steel, respectively. The red curves represent higher energy samples while the blue curves represent lower energy samples. (c) Normalized change in hardness as a function of normalized laser fluence for all materials investigated in this study.

Experiment Set Up: NC Cu-Zr samples were prepared from 99.99% pure Cu and 99.5% pure Zr powders in a SPEX 8000M high-energy ball mill under Ar atmosphere. Samples were then annealed for 1hr at 950°C, and then either quenched (Q) or slowly cooled (SC) to room temperature. Additional details of sample preparation for these materials can be found elsewhere [92, 173].

Femtosecond laser irradiation experiments were performed with a Clark MXR CPA-2110 Series Ti:Sapphire Ultrashort Pulse Laser with 1 kHz repetition rate, 780 nm wavelength, and 150 fs pulse width. All experiments were performed in air at room temperature. Regions of 0.1-0.5 mm^2 were exposed to single pulse fs-laser irradiation with ~30% overlap between subsequent pulses. Ablation thresholds were characterized on non-overlapping single pulse exposures via optical profilometry.

Indentation experiments were performed using a Nanomechanics iNano nanoindenter equipped with a 50 mN load cell and Berkovich tip. Prior to all indentation experiments, the tip

area function was calibrated on a fused silica standard. Measurements were performed using a CSM indentation protocol, where a dynamic oscillation is imposed atop the loading curve, allowing depth-resolved hardness measurements [174]. All hardness measurements reported are extracted from ~ 30 nm penetration depths. Hardness values and errors reported are the mean and standard deviation, respectively, of at least 20 indentations.

Appendix C Dynamic Relaxations of Metastable GBs during Ultrafast Thermal Cycle

Details of the STGBs along <100>, <110>, and <111> axes and ATGBs: The specifics on the misorientation/inclination angle, dimension, atom number, and the IS energy before and after the fast thermal cycling for various <100>, <110>, and <111> STGBs and ATGBs in Cu.

	CSL	Misorientation Angle(°)	x (Å)	y (Å)	z (Å)	N	E(H-0K) [mJ/m²]	E(C-0K) [mJ/m²]
<100> STGBs	Σ41(019)	12.7	327.35	262.14	14.46	104960	719.88	722.84
	Σ25(017)	16.3	255.61	256.46	14.46	80160	796.12	807.83
	Σ37(016)	18.9	219.89	264.25	14.46	71040	837.58	860.52
	Σ13(015)	22.6	184.33	259.21	14.46	58400	878.27	913.20
	Σ85(029)	25.1	333.28	267.50	14.46	108960	910.25	944.75
	Σ17(014)	28.1	149.05	269.70	14.46	49120	914.63	958.66
	Σ53(027)	31.9	263.17	262.75	14.46	84480	939.56	971.56
	Σ5(013)	36.9	114.31	249.84	14.46	34880	904.83	961.36
	Σ73(038)	41.1	308.86	246.42	14.46	92960	972.89	1006.39
	Σ29(025)	43.6	194.67	273.12	14.46	64960	983.11	1020.3
	Σ29(037)	46.4	275.30	275.47	14.46	92640	988.22	1027.27
	Σ5(012)	53.1	80.83	241.52	14.46	23840	951.2	993.46
	Σ53(059)	58.1	372.18	297.26	14.46	135200	916.59	950.88
	Σ17(035)	61.9	210.78	251.60	14.46	64800	856.53	903.65
	Σ89(058)	64.0	341.03	272.17	14.46	113440	844.56	879.24
	Σ13(023)	67.4	130.34	262.14	14.46	41760	789.78	828.75
	Σ25(034)	73.7	180.75	254.14	14.46	56160	676.79	687.46
<110> STGBs	Σ33(118)	20.05	207.65	235.66	20.45	84640	650.49	654.64
	Σ19(116)	26.525	157.55	223.76	20.45	60960	719.09	736.34
	Σ27(115)	31.586	265.61	225.81	20.45	103680	693.23	726.61

	CSL	Inclination Angle(°)	x (Å)	y (Å)	z (Å)	N	E(H-0K) [mJ/m²]	E(C-0K) [mJ/m²]
	Σ9(114)	38.942	130.14	246.49	20.45	55488	619.20	620.41
	Σ11(332)	129.521	143.86	238.56	20.45	59328	702.45	757.33
	Σ9(221)	141.058	184.05	240.27	20.45	76416	833.68	875.90
	Σ27(552)	148.414	225.42	266.55	20.45	103872	842.10	908.48
	Σ19(331)	153.475	222.85	219.38	20.45	84480	808.11	863.12
	Σ33(441)	159.95	293.70	247.68	20.45	125760	794.80	845.06
	Σ73(661)	166.557	436.72	247.09	20.45	186560	678.31	709.36
<111> STGBs	Σ57(178)	13.174	668.45	231.56	25.04	327840	608.73	617.60
	Σ31(156)	17.9	492.94	226.72	25.04	236640	709.71	728.65
	Σ21(145)	21.8	405.71	235.27	25.04	202080	775.35	803.21
	Σ67(279)	24.433	724.69	251.85	25.04	386400	811.63	859.27
	Σ13(134)	27.8	319.22	222.38	25.04	150240	841.81	875.46
	Σ39(257)	32.2	552.92	253.85	25.04	297120	888.82	951.90
	Σ7(123)	38.2	234.26	243.92	25.04	120960	877.93	950.78
	Σ49(358)	43.574	619.82	286.73	25.04	376320	866.61	934.92
	Σ37(347)	50.6	538.62	249.16	25.04	284160	821.90	883.51
	Σ61(459)	52.659	691.60	238.94	25.04	349920	796.68	856.03
	CSL	Inclination Angle(°)	x (Å)	y (Å)	z (Å)	N	E(H-0K) [mJ/m²]	E(C-0K) [mJ/m²]
ATGBs	Σ9(110)	70.530	325.31	262.01	20.45	147360	807.78	833.80
	Σ9(552)	54.740	187.84	255.14	20.45	82880	879.34	929.68
	Σ9(771)	64.760	508.63	288.47	20.45	253760	776.85	811.69
	Σ9(885)	46.690	632.40	267.7	20.45	292800	734.99	750.41
	Σ11(110)	64.760	397.62	291.02	20.45	200160	675.49	686.72
	Σ11(441)	54.740	293.68	250.12	20.45	127040	659.14	667.41
	Σ11(771)	70.530	508.61	287.38	20.45	252800	676.94	696.18
	Σ13(740)	18.430	291.435	291.012	14.46	103680	889.51	915.65

Table C-1. The model parameters and the corresponding GB energies at 0 K (heating and cooling) for STGBs along <100>, <110>, and <111> axes and ATGBs in Cu.

Details of the set-up and size effect study: The energetic and structural evolutions of

metastable tilted GBs under ultrafast thermal cycles are investigated by molecular dynamics

simulations. The periodic boundary conditions on all axes and NPT ensemble are applied in our

system. The inherent structure energy of a given GB is calculated as follows:

$$\gamma = (E_{tot} - N * E_{coh}) / (2 * A) \ ,$$

where E_{tot} is the total potential energy of the entire supercell, N is the total number of atoms in

the supercell, E_{coh} is the atomic cohesive energy in a single crystal reference system, and A is the

area of GB, i.e. the cross-sectional area of the supercell in xz plane. It is worth noting that the

system size is also studied. The previous study [94] has shown that ground-state structures and

energetics won't be affected, as long as the orthogonal directions parallel to the GB plane satisfy

the minimum periodic distance (depending on the cut-off radius of interatomic potential).

 To further examine the size effect during the non-equilibrium processing, in particular the

dimension along tilt axis, we also did some new calculations under the same thermal stimuli but

with larger simulation boxes. More specifically, we expand the tilt-axis dimension (*i.e.* z axis) to

3 times larger while keeping the x-y plane unchanged. 4 sets of heating/cooling curves for the

GBs at the misorientation angles of 28.1^0, 36.9^0, 53.1^0, and, 61.9^0 are investigated, respectively.

As seen in Figure C-1 below, the results of larger simulation boxes overlap well with the results

of smaller simulation boxes in the main text. Therefore, we do not expect a strong size effect on

the present study.
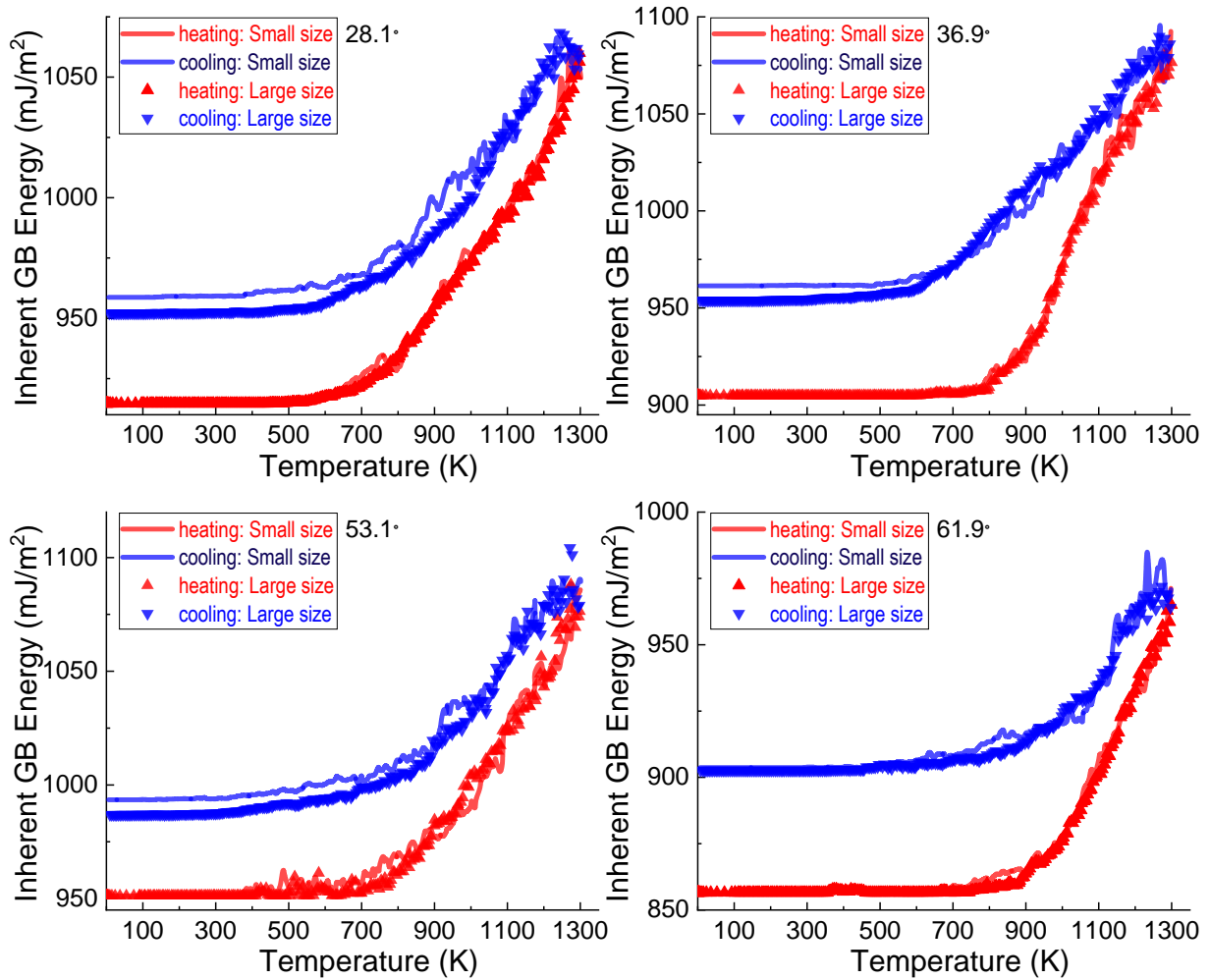
Figure C-1. Inherent energy evolution during the fast heating-cooling cycle for 4 different STGBs with the different misorientation angles (28.1^0, 36.9^0, 53.1^0, and 61.9^0). In each figure, two system sizes are studied, where the tilt axis (z) is increased 3 times and the other two axes are kept constant for the larger system. The blue and red curves represent the smaller system, while the solid red circles and blue squares represent the larger system.

Details of the distribution of displacement fields: The potential energy landscape (PEL) is known to interpret material properties in complex structures. From the PEL perspective, the elementary processes are the hopping between neighboring local minima connected by an intermediate saddle state. The activation relaxation technique (ART) is employed in probing the PEL of GBs and obtaining the displacement fields from the local minimum to the saddle state.

94

Specifically, a random atom inside the GBs is firstly chosen and perturbed randomly by ART. When the lowest eigenvalue of the PEL calculated by Lanczos algorithm is smaller than -0.01 eV Å^{-2}, the system is then relaxed to a saddle state. Once the initial local minimum and saddle state structures are obtained, the total Euclidean displacements are calculated. Here the statistic distributions of Euclidean norm distributions of GB's atomic rearrangements at different processing stages are shown in Figure C-2.
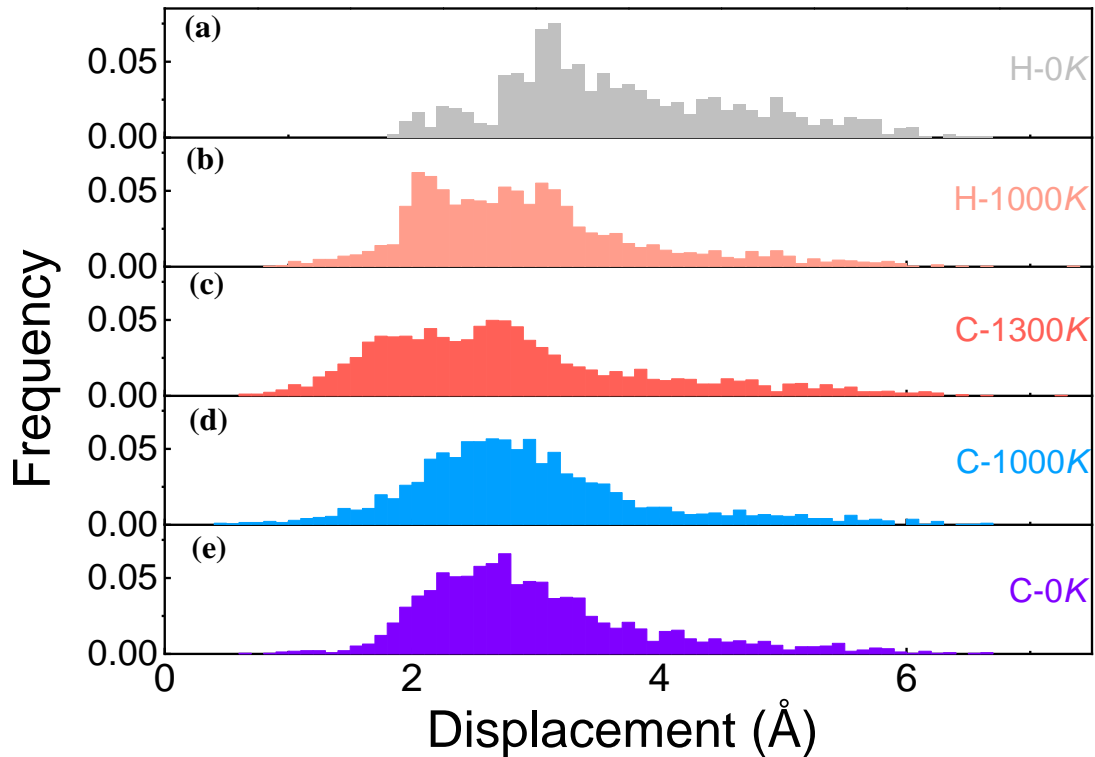
Figure C-2. The distributions of GB's atomic displacement at different processing stages.

Correlation between a given GB and its structural transition temperature extracted from heating stage: Figure C-3.a shows energy variations extracted form heating curves of all different GBs, where the entire cluster of curves also span into a crescent-shaped region similar with cooling curves. Figure C-3.b shows a clear monotonic trend between the critical structural

95

transition temperature and the GB's inherent structure energy based on the heating curves, which

demonstrates that this correlation always persists.
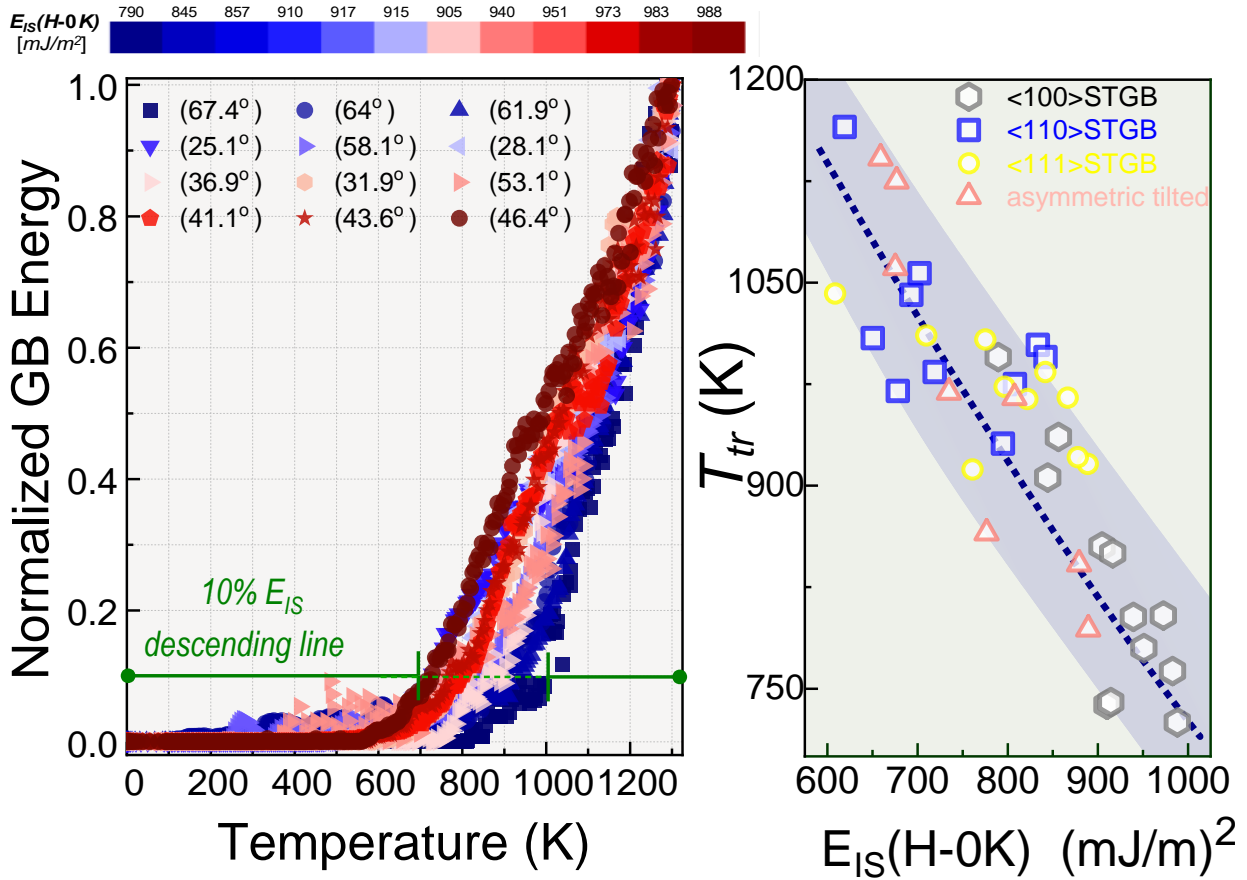
Figure C-3. The analysis on the correlation between critical structural transition temperature and inherent structure energy in the heating stage. (a) $\hat{E}_{IS}(H-T)$ for different <100> STGBs. The data for each GB is colored according to its pre-processing energy at H-0K. T_{tr} is measured when $\hat{E}_{IS}(H-T)$ reaches 10%, as marked by the green line. (b) The correlation between $E_{IS}(H\text{-}0K)$ and T_{tr} for various GBs. It is worth noting that such a correlation is almost identical to the trend shown in Figure 5-5, with only a quantitative shift.

Details of the STGBs along <100> axis in Ni: The specifics on the misorientation angle,

dimension, atom number, and the IS energy before and after the fast thermal cycling for various

<100> STGBs in Ni.

<100> STGBs	CSL	Misorientation Angle(°)	x (Å)	y (Å)	z (Å)	N	E(H-0K) [mJ/m²]	E(C-0K) [mJ/m²]
	$\sum13(015)$	22.6	179.46	250.38	10.56	43440	1295.67	1375.97

$\sum 85(029)$	25.1	**324.32**	259.27	10.56	81240	1347.41	1430.32
$\sum 17(014)$	28.1	145.12	231.05	10.56	32400	1347.23	1470.28
$\sum 53(027)$	31.9	256.13	255.61	10.56	63240	1393.21	1499.75
$\sum 5(013)$	36.9	111.30	221.01	10.56	23760	1343.56	1444.32
$\sum 73(038)$	41.1	300.62	239.38	10.56	69480	1435.25	1515.10
$\sum 97(049)$	47.92	346.56	275.82	10.56	92340	1462.14	1537.13
$\sum 17(035)$	61.9	205.19	245.18	10.56	48600	1278.86	1328.80
$\sum 13(023)$	67.4	126.90	227.04	10.56	27840	1159.30	1237.50

Table C-2. The model parameters and the corresponding GB energies at 0 K (heating and cooling) for STGBs along <100> axis in Ni.

Correlation between a given GB and its structural transition temperature in Ni:

Figure 5-5 already shows that a clear monotonic correlation between E_{IS} *(H-0K)* and T_{tr} in Cu exhibit. To examine the universality of such correlation, Ni is also studied here. Similar with results of Cu, the rescaled inherent structure energy curves in Ni exhibit a crescent shape as shown in Figure C-4.a. Meanwhile, the T_{tr} of all the GBs in Ni could be extracted in Figure C-4.a. Then, it is found that this similar correlation also exists in Ni as shown in Figure C-4.b, which demonstrates that this strong correlation could be applicable to many other materials as well.
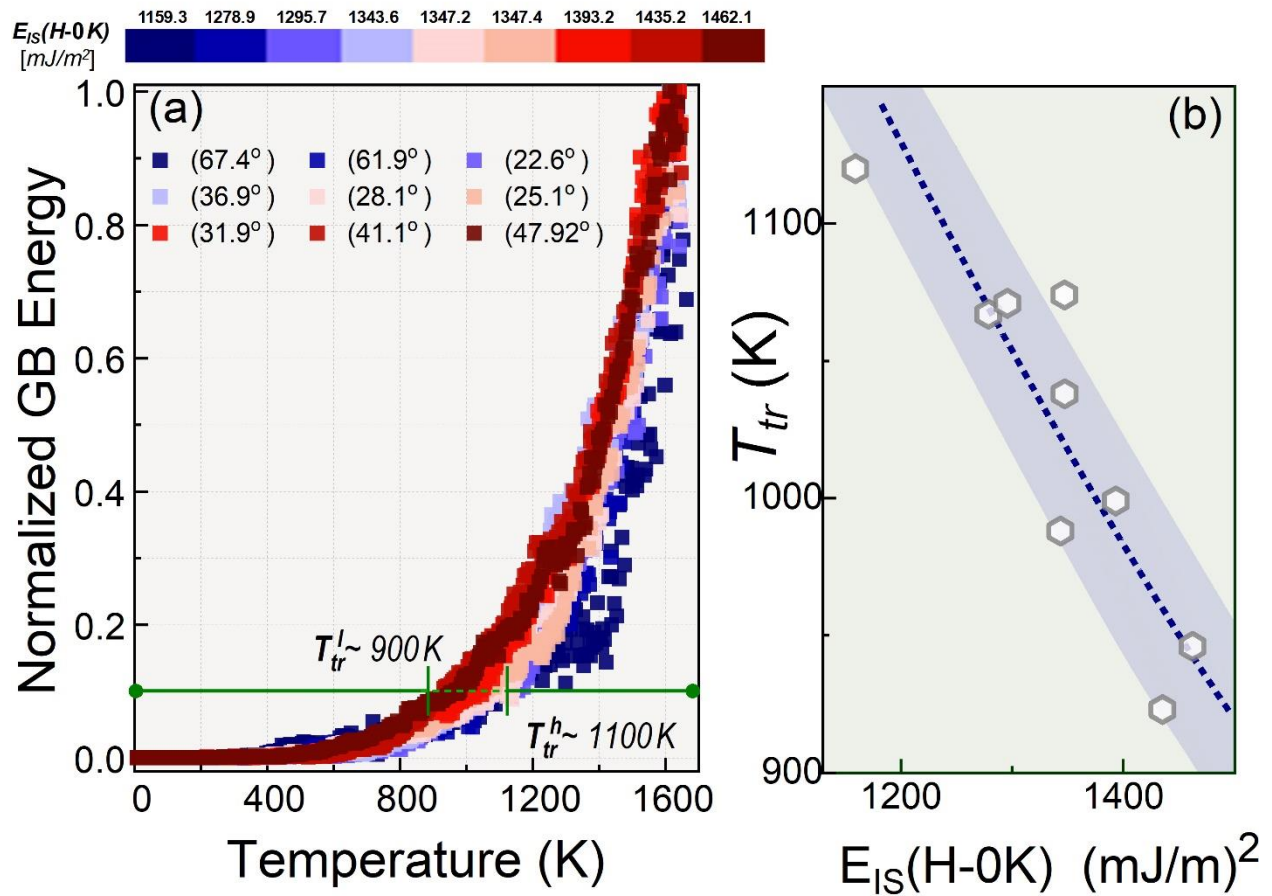
Figure C-4. (a) The rescaled inherent structure energy in Ni for different STGBs along <100> axis during the cooling stage. The data for each GB is colored according to its energy at H-0K seen in the legend. (b) The correlation between $E_{IS}(H-0K)$ and T_{tr}. Similar with Cu, data points of Ni also fall into a very narrow band, indicating a very strong correlation between the two variables.

Bibliography

[1] R.W. Grimes, R.J.M. Konings, L. Edwards, Greater tolerance for nuclear materials, Nature Materials 7(9) (2008) 683-685.

[2] Y. Guérin, G.S. Was, S.J. Zinkle, Materials Challenges for Advanced Nuclear Energy Systems, MRS Bulletin 34(1) (2017) 10-19.

[3] L.K. Mansur, Theory and experimental background on dimensional changes in irradiated alloys, Journal of Nuclear Materials 216 (1994) 97-123.

[4] G.S. Was, Materials degradation in fission reactors: Lessons learned of relevance to fusion reactor systems, Journal of Nuclear Materials 367-370 (2007) 11-20.

[5] G.R. Odette, M.J. Alinger, B.D. Wirth, Recent Developments in Irradiation-Resistant Steels, Annual Review of Materials Research 38(1) (2008) 471-503.

[6] M. Despeisse, S. Ford, The Role of Additive Manufacturing in Improving Resource Efficiency and Sustainability, in: S. Umeda, M. Nakano, H. Mizuyama, H. Hibino, D. Kiritsis, G. von Cieminski (Eds.) Advances in Production Management Systems: Innovative Production Management Towards Sustainable Growth, Springer International Publishing, Cham, 2015, pp. 129-136.

[7] M. Mani, K.W. Lyons, S.K. Gupta, Sustainability Characterization for Additive Manufacturing, J Res Natl Inst Stand Technol 119 (2014) 419-428.

[8] N. Choi, V. Kulitckii, J. Kottke, B. Tas, J. Choe, J.H. Yu, S. Yang, J.H. Park, J.S. Lee, G. Wilde, S.V. Divinski, Analyzing the 'non-equilibrium state' of grain boundaries in additively manufactured high-entropy CoCrFeMnNi alloy using tracer diffusion measurements, Journal of Alloys and Compounds 844 (2020) 155757.

[9] F. Yan, W. Xiong, E.J. Faierson, Grain Structure Control of Additively Manufactured Metallic Materials, Materials 10(11) (2017) 1260.

[10] P.C. Collins, D.A. Brice, P. Samimi, I. Ghamarian, H.L. Fraser, Microstructural Control of Additively Manufactured Metallic Materials, Annual Review of Materials Research 46(1) (2016) 63-91.

[11] M.C. Brennan, J.S. Keist, T.A. Palmer, Defects in Metal Additive Manufacturing Processes, Journal of Materials Engineering and Performance 30(7) (2021) 4808-4818.

[12] L. Lu, X. Chen, X. Huang, K. Lu, Revealing the Maximum Strength in Nanotwinned Copper, Science 323(5914) (2009) 607-610.

[13] L. Tan, T.R. Allen, J.T. Busby, Grain boundary engineering for structure materials of nuclear reactors, Journal of Nuclear Materials 441(1) (2013) 661-666.

[14] J. Han, V. Vitek, D.J. Srolovitz, Grain-boundary metastability and its statistical properties, Acta Mater. 104 (2016) 259-273.

[15] W.J. Phythian, R.E. Stoller, A.J.E. Foreman, A.F. Calder, D.J. Bacon, A comparison of displacement cascades in copper and iron by molecular dynamics and its application to microstructural evolution, Journal of Nuclear Materials 223(3) (1995) 245-261.

[16] T. Diaz de la Rubia, G.H. Gilmer, Structural Transformations and Defect Production in Ion Implanted Silicon: A Molecular Dynamics Simulation Study, Phys. Rev. Lett. 74(13) (1995) 2507-2510.

[17] D.J. Bacon, F. Gao, Y.N. Osetsky, The primary damage state in fcc, bcc and hcp metals as seen in molecular dynamics simulations, Journal of Nuclear Materials 276(1) (2000) 1-12.

[18] Y. Zhang, G.M. Stocks, K. Jin, C. Lu, H. Bei, B.C. Sales, L. Wang, L.K. Béland, R.E. Stoller, G.D. Samolyuk, M. Caro, A. Caro, W.J. Weber, Influence of chemical disorder on energy dissipation and defect evolution in concentrated solid solution alloys, Nature Communications 6(1) (2015) 8736.

[19] A. Hospital, J.R. Goñi, M. Orozco, J.L. Gelpí, Molecular dynamics simulations: advances and applications, Adv Appl Bioinform Chem 8 (2015) 37-47.

[20] C.R. Weinberger, A.T. Jennings, K. Kang, J.R. Greer, Atomistic simulations and continuum modeling of dislocation nucleation and strength in gold nanowires, Journal of the Mechanics and Physics of Solids 60(1) (2012) 84-103.

[21] F. Onimus, I. Monnet, J.L. Béchade, C. Prioul, P. Pilvin, A statistical TEM investigation of dislocation channeling mechanism in neutron irradiated zirconium alloys, Journal of Nuclear Materials 328(2) (2004) 165-179.

[22] Z. Bai, Y. Fan, Abnormal Strain Rate Sensitivity Driven by a Unit Dislocation-Obstacle Interaction in bcc Fe, Phys. Rev. Lett. 120(12) (2018) 125504.

[23] B. Wu, Z. Bai, A. Misra, Y. Fan, Atomistic mechanism and probability determination of the cutting of Guinier-Preston zones by edge dislocations in dilute Al-Cu alloys, Physical Review Materials 4(2) (2020) 020601.

[24] Z. Bai, G.H. Balbus, D.S. Gianola, Y. Fan, Mapping the kinetic evolution of metastable grain boundaries under non-equilibrium processing, Acta Mater. 200 (2020) 328-337.

[25] Z. Bai, A. Misra, Y. Fan, Universal Trend in the dynamic relaxations of tilted metastable grain boundaries during ultrafast thermal cycle, Materials Research Letters 10(6) (2022) 343-351.

[26] D. Wolf, V. Yamakov, S.R. Phillpot, A. Mukherjee, H. Gleiter, Deformation of nanocrystalline materials by molecular-dynamics simulation: relationship to experiments?, Acta Mater. 53(1) (2005) 1-40.

[27] J.D. Durrant, J.A. McCammon, Molecular dynamics simulations and drug discovery, BMC Biology 9(1) (2011) 71.

[28] L. Verlet, Computer "Experiments" on Classical Fluids. I. Thermodynamical Properties of Lennard-Jones Molecules, Physical Review 159(1) (1967) 98-103.

[29] F. Dommert, K. Wendler, R. Berger, L. Delle Site, C. Holm, Force Fields for Studying the Structure and Dynamics of Ionic Liquids: A Critical Review of Recent Developments, ChemPhysChem 13(7) (2012) 1625-1637.

[30] J.A. Harrison, J.D. Schall, S. Maskey, P.T. Mikulski, M.T. Knippenberg, B.H. Morrow, Review of force fields and intermolecular potentials used in atomistic computational materials research, Applied Physics Reviews 5(3) (2018) 031104.

[31] O. Penrose, Foundations of statistical mechanics, Reports on Progress in Physics 42(12) (1979) 1937-2006.

[32] J. Wereszczynski, J.A. McCammon, Statistical mechanics and molecular dynamics in evaluating thermodynamic properties of biomolecular recognition, Quarterly Reviews of Biophysics 45(1) (2011) 1-25.

[33] J.R. Perilla, B.C. Goh, C.K. Cassidy, B. Liu, R.C. Bernardi, T. Rudack, H. Yu, Z. Wu, K. Schulten, Molecular dynamics simulations of large macromolecular complexes, Current Opinion in Structural Biology 31 (2015) 64-74.

[34] Y. Shibuta, K. Oguchi, T. Takaki, M. Ohno, Homogeneous nucleation and microstructure evolution in million-atom molecular dynamics simulation, Scientific Reports 5(1) (2015) 13534.

[35] Q. Peng, F. Meng, Y. Yang, C. Lu, H. Deng, L. Wang, S. De, F. Gao, Shockwave generates $< 100 >$ dislocation loops in bcc iron, Nature Communications 9(1) (2018) 4880.

[36] Y.-H. Wen, Z.-Z. Zhu, R.-Z. Zhu, Molecular dynamics study of the mechanical behavior of nickel nanowire: Strain rate effects, Comput. Mater. Sci. 41(4) (2008) 553-560.

[37] T. Zhu, J. Li, A. Samanta, A. Leach, K. Gall, Temperature and Strain-Rate Dependence of Surface Dislocation Nucleation, Phys. Rev. Lett. 100(2) (2008) 025502.

[38] H. Zhao, N.R. Aluru, Temperature and strain-rate dependent fracture strength of graphene, Journal of Applied Physics 108(6) (2010) 064321.

[39] N.J. Wagner, B.L. Holian, A.F. Voter, Molecular-dynamics simulations of two-dimensional materials at high strain rates, Physical Review A 45(12) (1992) 8457-8470.

[40] P. Wang, S. Xu, Z. Li, J. Yang, C. Zhang, H. Zheng, S. Hu, Experimental investigation on the strain-rate effect and inertia effect of closed-cell aluminum foam subjected to dynamic loading, Materials Science and Engineering: A 620 (2015) 253-261.

[41] N. Mousseau, L.K. Béland, P. Brommer, J.-F. Joly, F. El-Mellouhi, E. Machado-Charry, M.-C. Marinica, P. Pochet, The Activation-Relaxation Technique: ART Nouveau and Kinetic ART, Journal of Atomic, Molecular, and Optical Physics 2012 (2012) 925278.

[42] C. Lanczos, An iteration method for the solution of the eigenvalue problem of linear differential and integral operators, (1950).

[43] M. Trochet, A. Sauvé-Lacoursière, N. Mousseau, Algorithmic developments of the kinetic activation-relaxation technique: Accessing long-time kinetics of larger and more complex systems, The Journal of Chemical Physics 147(15) (2017) 152712.

[44] A. Kushima, X. Lin, J. Li, J. Eapen, J.C. Mauro, X. Qian, P. Diep, S. Yip, Computing the viscosity of supercooled liquids, The Journal of Chemical Physics 130(22) (2009) 224504.

[45] A. Laio, M. Parrinello, Escaping free-energy minima, Proceedings of the National Academy of Sciences 99(20) (2002) 12562-12566.

[46] G. Henkelman, B.P. Uberuaga, H. Jónsson, A climbing image nudged elastic band method for finding saddle points and minimum energy paths, The Journal of Chemical Physics 113(22) (2000) 9901-9904.

[47] Y. Fan, S. Yip, B. Yildiz, Autonomous basin climbing method with sampling of multiple transition pathways: application to anisotropic diffusion of point defects in hcp Zr, Journal of Physics: Condensed Matter 26(36) (2014) 365402.

[48] X.-M. Bai, A.F. Voter, R.G. Hoagland, M. Nastasi, B.P. Uberuaga, Efficient Annealing of Radiation Damage Near Grain Boundaries via Interstitial Emission, Science 327(5973) (2010) 1631-1634.

[49] F. Montalenti, A.F. Voter, Applying Accelerated Molecular Dynamics to Crystal Growth, physica status solidi (b) 226(1) (2001) 21-27.

[50] P. Cao, M. Li, R.J. Heugle, H.S. Park, X. Lin, Self-learning metabasin escape algorithm for supercooled liquids, Physical Review E 86(1) (2012) 016710.

[51] Y. Fan, Y.N. Osetskiy, S. Yip, B. Yildiz, Mapping strain rate dependence of dislocation-defect interactions by atomistic simulations, Proceedings of the National Academy of Sciences 110(44) (2013) 17756-17761.

[52] V. Shastry, T. Diaz de la Rubia, The Interaction Between Point Defects and Edge Dislocation in BCC Iron, Journal of Engineering Materials and Technology 121(2) (1999) 126-128.

[53] A. Kipelova, R. Kaibyshev, V. Skorobogatykh, I. Schenkova, Portevin-Le Chatelier effect in an E911 creep resistant steel with 3%Co additives, Journal of Physics: Conference Series 240 (2010) 012100.

[54] M.A. Lebyodkin, Y. Brechet, Y. Estrin, L.P. Kubin, Statistics of the Catastrophic Slip Events in the Portevin--Le Ch\^atelier Effect, Phys. Rev. Lett. 74(23) (1995) 4758-4761.

[55] A. Bertram, T. Böhlke, C. Brüggemann, Y. Estrin, M. Lebyodkin, Modeling and Simulation of the Portevin-Le Chatelier Effect, PAMM 6(1) (2006) 353-354.

[56] J.M. Robinson, M.P. Shaw, Microstructural and mechanical influences on dynamic strain aging phenomena, International Materials Reviews 39(3) (1994) 113-122.

[57] U.F.A.A.S.A.M.F.C.B.C.J.W.M.T.B. Kocks, Progress in materials science. Vol. 19, Vol. 19, Pergamon, Oxford (etc.), 1975.

[58] Y. Brechet, Y. Estrin, On the influence of precipitation on the Portevin-Le Chatelier effect, Acta Metallurgica et Materialia 43(3) (1995) 955-963.

[59] S. Zhang, P.G. McCormick, Y. Estrin, The morphology of Portevin–Le Chatelier bands: finite element simulation for Al–Mg–Si, Acta Mater. 49(6) (2001) 1087-1094.

[60] W.A. Curtin, D.L. Olmsted, L.G. Hector, A predictive mechanism for dynamic strain ageing in aluminium–magnesium alloys, Nature Materials 5(11) (2006) 875-880.

[61] F.R.N.H.J.P. Nabarro, Dislocations in Solids, Volume 12. http://site.ebrary.com/id/10169700, 2004).

[62] G.J. Ackland, D.J. Bacon, A.F. Calder, T. Harry, Computer simulation of point defect properties in dilute Fe—Cu alloy using a many-body interatomic potential, Philosophical Magazine A 75(3) (1997) 713-732.

[63] A.F. Voter, INTRODUCTION TO THE KINETIC MONTE CARLO METHOD, in: K.E. Sickafus, E.A. Kotomin, B.P. Uberuaga (Eds.) Radiation Effects in Solids, Springer Netherlands, Dordrecht, 2007, pp. 1-23.

[64] Y.N. Osetsky, D.J. Bacon, An atomic-level model for studying the dynamics of edge dislocations in metals, Modelling and Simulation in Materials Science and Engineering 11(4) (2003) 427-446.

[65] X. Yan, P. Sharma, Time-Scaling in Atomistics and the Rate-Dependent Mechanical Behavior of Nanostructures, Nano Letters 16(6) (2016) 3487-3492.

[66] J. Li, AtomEye: an efficient atomistic configuration viewer, Modelling and Simulation in Materials Science and Engineering 11(2) (2003) 173-177.

[67] D. Terentyev, L. Malerba, D.J. Bacon, Y.N. Osetsky, The effect of temperature and strain rate on the interaction between an edge dislocation and an interstitial dislocation loop in α-iron, Journal of Physics: Condensed Matter 19(45) (2007) 456211.

[68] D. Terentyev, Y.N. Osetsky, D.J. Bacon, Competing processes in reactions between an edge dislocation and dislocation loops in a body-centred cubic metal, Scripta Materialia 62(9) (2010) 697-700.

[69] B.P. Uberuaga, R.G. Hoagland, A.F. Voter, S.M. Valone, Direct Transformation of Vacancy Voids to Stacking Fault Tetrahedra, Phys. Rev. Lett. 99(13) (2007) 135501.

[70] A. Dutta, M. Bhattacharya, N. Gayathri, G.C. Das, P. Barat, The mechanism of climb in dislocation–nanovoid interaction, Acta Mater. 60(9) (2012) 3789-3798.

[71] G. Monnet, Mechanical and energetical analysis of molecular dynamics simulations of dislocation–defect interactions, Acta Mater. 55(15) (2007) 5081-5088.

[72] C.A. Schuh, T.G. Nieh, A survey of instrumented indentation studies on metallic glasses, Journal of Materials Research 19(1) (2004) 4.

[73] Y. Fan, Y.N. Osetsky, S. Yip, B. Yildiz, Onset Mechanism of Strain-Rate-Induced Flow Stress Upturn, Phys. Rev. Lett. 109(13) (2012) 135503.

[74] F. Onimus, J.-L. Béchade, A polycrystalline modeling of the mechanical behavior of neutron irradiated zirconium alloys, Journal of Nuclear Materials 384(2) (2009) 163-174.

[75] J.W. Dunlop, Y.J.M. Bréchet, L. Legras, Y. Estrin, Dislocation density-based modelling of plastic deformation of Zircaloy-4, Materials Science and Engineering: A 443(1) (2007) 77-86.

[76] K. Farrell, T.S. Byun, N. Hashimoto, Deformation mode maps for tensile deformation of neutron-irradiated structural alloys, Journal of Nuclear Materials 335(3) (2004) 471-486.

[77] N. Hashimoto, T.S. Byun, K. Farrell, S.J. Zinkle, Deformation microstructure of neutron-irradiated pure polycrystalline metals, Journal of Nuclear Materials 329-333 (2004) 947-952.

[78] H. Wang, D.S. Xu, D. Rodney, P. Veyssière, R. Yang, Atomistic investigation of the annihilation of non-screw dislocation dipoles in Al, Cu, Ni and γ-TiAl, Modelling and Simulation in Materials Science and Engineering 21(2) (2013) 025002.

[79] C. Deng, C.A. Schuh, Atomistic Simulation of Slow Grain Boundary Motion, Phys. Rev. Lett. 106(4) (2011) 045503.

[80] Y. Mishin, M. Asta, J. Li, Atomistic modeling of interfaces and their impact on microstructure and properties, Acta Mater. 58(4) (2010) 1117-1151.

[81] A.P.B.R.W. Sutton, Interfaces in crystalline materials, Clarendon Press ; Oxford University Press, Oxford; New York, 1995.

[82] M.A. Meyers, A. Mishra, D.J. Benson, Mechanical properties of nanocrystalline materials, Progress in Materials Science 51(4) (2006) 427-556.

[83] J. Hu, Y.N. Shi, X. Sauvage, G. Sha, K. Lu, Grain boundary stability governs hardening and softening in extremely fine nanograined metals, Science 355(6331) (2017) 1292-1296.

[84] H. Van Swygenhoven, J.R. Weertman, Deformation in nanocrystalline metals, Materials Today 9(5) (2006) 24-31.

[85] T.J. Rupert, C.A. Schuh, Sliding wear of nanocrystalline Ni–W: Structural evolution and the apparent breakdown of Archard scaling, Acta Mater. 58(12) (2010) 4137-4148.

[86] J.D. Schuler, C.M. Barr, N.M. Heckman, G. Copeland, B.L. Boyce, K. Hattar, T.J. Rupert, In Situ High-Cycle Fatigue Reveals Importance of Grain Boundary Structure in Nanocrystalline Cu-Zr, JOM 71(4) (2019) 1221-1232.

[87] A. Khalajhedayati, Z. Pan, T.J. Rupert, Manipulating the interfacial structure of nanomaterials to achieve a unique combination of strength and ductility, Nature Communications 7(1) (2016) 10802.

[88] T. Frolov, D.L. Olmsted, M. Asta, Y. Mishin, Structural phase transformations in metallic grain boundaries, Nature Communications 4(1) (2013) 1899.

[89] Q. Zhu, A. Samanta, B. Li, R.E. Rudd, T. Frolov, Predicting phase behavior of grain boundaries with evolutionary search and machine learning, Nature Communications 9(1) (2018) 467.

[90] A. Kashinath, A. Misra, M.J. Demkowicz, Stable Storage of Helium in Nanoscale Platelets at Semicoherent Interfaces, Phys. Rev. Lett. 110(8) (2013) 086101.

[91] A. Vattré, T. Jourdan, H. Ding, M.C. Marinica, M.J. Demkowicz, Non-random walk diffusion enhances the sink strength of semicoherent interfaces, Nature Communications 7(1) (2016) 10424.

[92] G.H. Balbus, M.P. Echlin, C.M. Grigorian, T.J. Rupert, T.M. Pollock, D.S. Gianola, Femtosecond laser rejuvenation of nanocrystalline metals, Acta Mater. 156 (2018) 183-195.

[93] Y. Mishin, M.J. Mehl, D.A. Papaconstantopoulos, A.F. Voter, J.D. Kress, Structural stability and lattice defects in copper: Ab initio, tight-binding, and embedded-atom calculations, Phys. Rev. B 63(22) (2001) 224106.

[94] M.A. Tschopp, S.P. Coleman, D.L. McDowell, Symmetric and asymmetric tilt grain boundary structure and energy in Cu and Al (and transferability to other fcc metals), Integrating Materials and Manufacturing Innovation 4(1) (2015) 11.

[95] E. Cancès, F. Legoll, M.-C. Marinica, K. Minoukadeh, F. Willaime, Some improvements of the activation-relaxation technique method for finding transition pathways on potential energy surfaces, The Journal of Chemical Physics 130(11) (2009) 114711.

[96] H. Zhang, D.J. Srolovitz, Simulation and analysis of the migration mechanism of $\Sigma5$ tilt grain boundaries in an fcc metal, Acta Mater. 54(3) (2006) 623-633.

[97] L. Zhong, J. Wang, H. Sheng, Z. Zhang, S.X. Mao, Formation of monatomic metallic glasses through ultrafast liquid quenching, Nature 512(7513) (2014) 177-180.

[98] P.G. Debenedetti, F.H. Stillinger, Supercooled liquids and the glass transition, Nature 410(6825) (2001) 259-267.

[99] S. Sastry, P.G. Debenedetti, F.H. Stillinger, Signatures of distinct dynamical regimes in the energy landscape of a glass-forming liquid, Nature 393(6685) (1998) 554-557.

[100] F.H. Stillinger, A Topographic View of Supercooled Liquids and Glass Formation, Science 267(5206) (1995) 1935-1939.

[101] Y.Q. Cheng, E. Ma, Atomic-level structure and structure–property relationship in metallic glasses, Progress in Materials Science 56(4) (2011) 379-473.

[102] D.J. Wales, A Microscopic Basis for the Global Appearance of Energy Landscapes, Science 293(5537) (2001) 2067-2070.

[103] D.J. Wales, Decoding the energy landscape: extracting structure, dynamics and thermodynamics, Philosophical Transactions of the Royal Society A: Mathematical, Physical and Engineering Sciences 370(1969) (2012) 2877-2899.

[104] Y. Fan, B. Yildiz, S. Yip, Analogy between glass rheology and crystal plasticity: yielding at high strain rate, Soft Matter 9(40) (2013) 9511-9514.

[105] C. Liu, X. Yan, P. Sharma, Y. Fan, Unraveling the non-monotonic ageing of metallic glasses in the metastability-temperature space, Comput. Mater. Sci. 172 (2020) 109347.

[106] Y. Fan, T. Iwashita, T. Egami, Energy landscape-driven non-equilibrium evolution of inherent structure in disordered material, Nature Communications 8(1) (2017) 15417.

[107] A.C. Lund, C.A. Schuh, Strength asymmetry in nanocrystalline metals under multiaxial loading, Acta Mater. 53(11) (2005) 3193-3205.

[108] A. Khalajhedayati, T.J. Rupert, Emergence of localized plasticity and failure through shear banding during microcompression of a nanocrystalline alloy, Acta Mater. 65 (2014) 326-337.

[109] H. Van Swygenhoven, M. Spaczer, A. Caro, D. Farkas, Competing plastic deformation mechanisms in nanophase metals, Phys. Rev. B 60(1) (1999) 22-25.

[110] H. Zhang, D.J. Srolovitz, J.F. Douglas, J.A. Warren, Grain boundaries exhibit the dynamics of glass-forming liquids, Proceedings of the National Academy of Sciences 106(19) (2009) 7735-7740.

[111] T.A. Sharp, S.L. Thomas, E.D. Cubuk, S.S. Schoenholz, D.J. Srolovitz, A.J. Liu, Machine learning determination of atomic dynamics at grain boundaries, Proceedings of the National Academy of Sciences 115(43) (2018) 10943-10947.

[112] K.C. Alexander, C.A. Schuh, Exploring grain boundary energy landscapes with the activation-relaxation technique, Scripta Materialia 68(12) (2013) 937-940.

[113] D. Rodney, C. Schuh, Distribution of Thermally Activated Plastic Events in a Flowing Glass, Phys. Rev. Lett. 102(23) (2009) 235503.

[114] H. Kallel, N. Mousseau, F. Schiettekatte, Evolution of the Potential-Energy Surface of Amorphous Silicon, Phys. Rev. Lett. 105(4) (2010) 045503.

[115] C. Liu, X.-X. Chen, J. Zhang, H.-Z. Zhou, L. Zhang, Y.-K. Guo, Advanced treatment of bio-treated coal chemical wastewater by a novel combination of microbubble catalytic ozonation and biological process, Separation and Purification Technology 197 (2018) 295-301.

[116] B. Schönfelder, D. Wolf, S.R. Phillpot, M. Furtkamp, Molecular-Dynamics Method for the Simulation of Grain-Boundary Migration, Interface Science 5(4) (1997) 245-262.

[117] M.R. Sørensen, Y. Mishin, A.F. Voter, Diffusion mechanisms in Cu grain boundaries, Phys. Rev. B 62(6) (2000) 3658-3673.

[118] N.Q. Vo, J. Schäfer, R.S. Averback, K. Albe, Y. Ashkenazy, P. Bellon, Reaching theoretical strengths in nanocrystalline Cu by grain boundary doping, Scripta Materialia 65(8) (2011) 660-663.

[119] L. Zhang, C. Lu, Y. Shibuta, Shear response of grain boundaries with metastable structures by molecular dynamics simulations, Modelling and Simulation in Materials Science and Engineering 26(3) (2018) 035008.

[120] C. Wu, M.S. Christensen, J.-M. Savolainen, P. Balling, L.V. Zhigilei, Generation of subsurface voids and a nanocrystalline surface layer in femtosecond laser irradiation of a single-crystal Ag target, Phys. Rev. B 91(3) (2015) 035413.

[121] C. Wu, L.V. Zhigilei, Nanocrystalline and Polyicosahedral Structure of a Nanospike Generated on Metal Surface Irradiated by a Single Femtosecond Laser Pulse, The Journal of Physical Chemistry C 120(8) (2016) 4438-4447.

[122] M. Gill-Comeau, L.J. Lewis, Ultrashort-pulse laser ablation of nanocrystalline aluminum, Phys. Rev. B 84(22) (2011) 224110.

[123] O. Renk, A. Hohenwarter, K. Eder, K.S. Kormout, J.M. Cairney, R. Pippan, Increasing the strength of nanocrystalline steels by annealing: Is segregation necessary?, Scripta Materialia 95 (2015) 27-30.

[124] X. Huang, N. Hansen, N. Tsuji, Hardening by Annealing and Softening by Deformation in Nanostructured Metals, Science 312(5771) (2006) 249-251.

[125] L. Chang, P.W. Kao, C.H. Chen, Strengthening mechanisms in electrodeposited Ni–P alloys with nanocrystalline grains, Scripta Materialia 56(8) (2007) 713-716.

[126] X. Zhou, X.Y. Li, K. Lu, Enhanced thermal stability of nanograined metals below a critical grain size, Science 360(6388) (2018) 526-530.

[127] O. Renk, A. Hohenwarter, B. Schuh, J.H. Li, R. Pippan, Hardening by annealing: insights from different alloys, IOP Conference Series: Materials Science and Engineering 89 (2015) 012043.

[128] S.L. Thomas, K. Chen, J. Han, P.K. Purohit, D.J. Srolovitz, Reconciling grain growth and shear-coupled grain boundary migration, Nature Communications 8(1) (2017) 1764.

[129] H.A. Khater, A. Serra, R.C. Pond, J.P. Hirth, The disconnection mechanism of coupled migration and shear at grain boundaries, Acta Mater. 60(5) (2012) 2007-2020.

[130] G.J. Tucker, M.A. Tschopp, D.L. McDowell, Evolution of structure and free volume in symmetric tilt grain boundaries during dislocation nucleation, Acta Mater. 58(19) (2010) 6464-6473.

[131] D.L. Olmsted, D. Buta, A. Adland, S.M. Foiles, M. Asta, A. Karma, Dislocation-Pairing Transitions in Hot Grain Boundaries, Phys. Rev. Lett. 106(4) (2011) 046101.

[132] J.-P. Du, Y.-J. Wang, Y.-C. Lo, L. Wan, S. Ogata, Mechanism transition and strong temperature dependence of dislocation nucleation from grain boundaries: An accelerated molecular dynamics study, Phys. Rev. B 94(10) (2016) 104110.

[133] T.J. Rupert, C.A. Schuh, Mechanically driven grain boundary relaxation: a mechanism for cyclic hardening in nanocrystalline Ni, Philosophical Magazine Letters 92(1) (2012) 20-28.

[134] N.Q. Vo, R.S. Averback, P. Bellon, A. Caro, Yield strength in nanocrystalline Cu during high strain rate deformation, Scripta Materialia 61(1) (2009) 76-79.

[135] D. Utt, A. Stukowski, K. Albe, Grain boundary structure and mobility in high-entropy alloys: A comparative molecular dynamics study on a Σ11 symmetrical tilt grain boundary in face-centered cubic CuNiCoFe, Acta Mater. 186 (2020) 11-19.

[136] J. Schiøtz, T. Vegge, F.D. Di Tolla, K.W. Jacobsen, Atomic-scale simulations of the mechanical deformation of nanocrystalline metals, Phys. Rev. B 60(17) (1999) 11971-11983.

[137] P.R.M. van Beers, V.G. Kouznetsova, M.G.D. Geers, M.A. Tschopp, D.L. McDowell, A multiscale model of grain boundary structure and energy: From atomistics to a continuum description, Acta Mater. 82 (2015) 513-529.

[138] D.L. Olmsted, E.A. Holm, S.M. Foiles, Survey of computed grain boundary properties in face-centered cubic metals—II: Grain boundary mobility, Acta Mater. 57(13) (2009) 3704-3713.

[139] D. Raabe, M. Herbig, S. Sandlöbes, Y. Li, D. Tytko, M. Kuzmina, D. Ponge, P.P. Choi, Grain boundary segregation engineering in metallic alloys: A pathway to the design of interfaces, Current Opinion in Solid State and Materials Science 18(4) (2014) 253-261.

[140] M.A. Tschopp, D.L. McDowell, Structures and energies of Σ 3 asymmetric tilt grain boundaries in copper and aluminium, Philos. Mag. 87(22) (2007) 3147-3173.

[141] M.A. Tschopp, D.L. McDowell, Asymmetric tilt grain boundary structure and energy in copper and aluminium, Philos. Mag. 87(25) (2007) 3871-3892.

[142] C. Chakravarty, Path integral simulations of quantum Lennard-Jones solids, The Journal of Chemical Physics 116(20) (2002) 8938-8947.

[143] F.H. Stillinger, T.A. Weber, Lindemann melting criterion and the Gaussian core model, Phys. Rev. B 22(8) (1980) 3790-3794.

[144] S. Sarkar, C. Jana, B. Bagchi, Breakdown of universal Lindemann criterion in the melting of Lennard-Jones polydisperse solids, Journal of Chemical Sciences 129(7) (2017) 833-840.

[145] J.W. Cahn, Y. Mishin, A. Suzuki, Coupling grain boundary motion to shear deformation, Acta Mater. 54(19) (2006) 4953-4975.

[146] E.A. Holm, S.M. Foiles, How Grain Growth Stops: A Mechanism for Grain-Growth Stagnation in Pure Materials, Science 328(5982) (2010) 1138-1141.

[147] E.A. Holm, S.M. Foiles, Grain Growth Stagnation Caused by the Grain Boundary Roughening Transition, Materials Science Forum 715-716 (2012) 415-415.

[148] M. Liao, X. Xiao, S.T. Chui, Y. Han, Grain-Boundary Roughening in Colloidal Crystals, Physical Review X 8(2) (2018) 021045.

[149] J.J. Bean, K.P. McKenna, Origin of differences in the excess volume of copper and nickel grain boundaries, Acta Mater. 110 (2016) 246-257.

[150] D.S. Aidhy, Y. Zhang, W.J. Weber, A fast grain-growth mechanism revealed in nanocrystalline ceramic oxides, Scripta Materialia 83 (2014) 9-12.

[151] E.R. Homer, E.A. Holm, S.M. Foiles, D.L. Olmsted, Trends in Grain Boundary Mobility: Survey of Motion Mechanisms, JOM 66(1) (2014) 114-120.

[152] C.A. Deng, C.A. Schuh, Atomistic Simulation of Slow Grain Boundary Motion, Phys. Rev. Lett. 106(4) (2011) 4.

[153] Z.T. Trautt, M. Upmanyu, A. Karma, Interface Mobility from Interface Random Walk, Science 314(5799) (2006) 632-635.

[154] C. Deng, C.A. Schuh, Diffusive-to-ballistic transition in grain boundary motion studied by atomistic simulations, Phys. Rev. B 84(21) (2011) 214102.

[155] X.W. Zhou, R. Dingreville, R.A. Karnesky, Molecular dynamics studies of irradiation effects on hydrogen isotope diffusion through nickel crystals and grain boundaries, Physical Chemistry Chemical Physics 20(1) (2018) 520-534.

[156] M.I. Mendelev, D.J. Srolovitz, G.J. Ackland, S. Han, Effect of Fe Segregation on the Migration of a Non-Symmetric Σ5 Tilt Grain Boundary in Al, Journal of Materials Research 20(1) (2011) 208-218.

[157] O.A. Restrepo, N. Mousseau, M. Trochet, F. El-Mellouhi, O. Bouhali, C.S. Becquart, Carbon diffusion paths and segregation at high-angle tilt grain boundaries in \ensuremath{\alpha}-Fe studied by using a kinetic activation-relation technique, Phys. Rev. B 97(5) (2018) 054309.

[158] C.A. Kathleen, A.S. Christopher, Towards the reliable calculation of residence time for off-lattice kinetic Monte Carlo simulations, Modelling and Simulation in Materials Science and Engineering 24(6) (2016) 065014.

[159] G.T. Barkema, N. Mousseau, Event-Based Relaxation of Continuous Disordered Systems, Phys. Rev. Lett. 77(21) (1996) 4358-4361.

[160] A. Suzuki, Y. Mishin, Atomic mechanisms of grain boundary diffusion: Low versus high temperatures, Journal of Materials Science 40(12) (2005) 3155-3161.

[161] A.M. Alsayed, M.F. Islam, J. Zhang, P.J. Collings, A.G. Yodh, Premelting at Defects Within Bulk Colloidal Crystals, Science 309(5738) (2005) 1207-1210.

[162] C. Liu, P. Guan, Y. Fan, Correlating defects density in metallic glasses with the distribution of inherent structures in potential energy landscape, Acta Mater. 161 (2018) 295-301.

[163] Y. Mishin, Atomistic modeling of the γ and γ′-phases of the Ni–Al system, Acta Mater. 52(6) (2004) 1451-1467.

[164] A.E. Perrin, C.A. Schuh, Stabilized Nanocrystalline Alloys: The Intersection of Grain Boundary Segregation with Processing Science, Annual Review of Materials Research 51(1) (2021) 241-268.

[165] T.J. Rupert, The role of complexions in metallic nano-grain stability and deformation, Current Opinion in Solid State and Materials Science 20(5) (2016) 257-267.

[166] K.G.F. Janssens, D. Olmsted, E.A. Holm, S.M. Foiles, S.J. Plimpton, P.M. Derlet, Computing the mobility of grain boundaries, Nature Materials 5(2) (2006) 124-127.

[167] J. Helfferich, I. Lyubimov, D. Reid, J.J. de Pablo, Inherent structure energy is a good indicator of molecular mobility in glasses, Soft Matter 12(27) (2016) 5898-5904.

[168] D.R. Reid, I. Lyubimov, M.D. Ediger, J.J. de Pablo, Age and structure of a model vapour-deposited glass, Nature Communications 7(1) (2016) 13062.

[169] S. Zhang, C. Liu, Y. Fan, Y. Yang, P. Guan, Soft-Mode Parameter as an Indicator for the Activation Energy Spectra in Metallic Glass, The Journal of Physical Chemistry Letters 11(7) (2020) 2781-2787.

[170] A. Stukowski, Visualization and analysis of atomistic simulation data with OVITO–the Open Visualization Tool, Modelling and Simulation in Materials Science and Engineering 18(1) (2009) 015012.

[171] C.L. Kelchner, S.J. Plimpton, J.C. Hamilton, Dislocation nucleation and defect structure during surface indentation, Phys. Rev. B 58(17) (1998) 11085-11088.

[172] S. Scheriau, Z. Zhang, S. Kleber, R. Pippan, Deformation mechanisms of a modified 316L austenitic steel subjected to high pressure torsion, Materials Science and Engineering A-structural Materials Properties Microstructure and Processing 528 (2011) 2776-2786.

[173] A. Khalajhedayati, Z. Pan, T.J. Rupert, Manipulating the interfacial structure of nanomaterials to achieve a unique combination of strength and ductility, Nature Communications 7 (2016) 10802.

[174] W.C. Oliver, G.M. Pharr, An improved technique for determining hardness and elastic modulus using load and displacement sensing indentation experiments, Journal of Materials Research 7(6) (1992) 1564-1583.